Dissertation

submitted to the
Combined Faculties for the Natural Sciences and for Mathematics
of the Ruperto-Carola University of Heidelberg, Germany
for the degree of
Doctor of Natural Sciences

Put forward by
Christine Böhm
born in Weilburg, Germany

Date of oral examination: January 14, 2015

High-precision mass measurements of neutron-deficient Tl isotopes at ISOLTRAP and the development of an ultra-stable voltage source for the PENTATRAP experiment

Referees: Prof. Dr. Klaus Blaum
PD Dr. Klaus Reygers

Abstract

Atomic masses and hence binding energies of nuclides are of great importance for studies of nuclear structure since they reflect all effective interactions in a nucleus. Within this thesis the masses of seven nuclides, namely ^{194}Au, ^{194}Hg, ^{190,193,198}Tl and ^{202,208}Pb, were determined at the Penning-trap mass spectrometer ISOLTRAP at ISOLDE/CERN.
The thallium region in the chart of isotopes is of special interest due to the occurrence of nuclear structure effects like low-lying isomers, level inversion, shape coexistence and deformations. These effects are investigated by applying finite-difference mass formulas, such as the two-neutron separation energies or the so-called empirical pairing gaps. The second topic addressed within the present thesis is an ultra-stable voltage source, called StaReP (**Sta**ble **Re**ference for **P**enning Trap Experiments), which was developed at the Max-Planck-Institut für Kernphysik. It is one of the key components of the high-precision mass spectrometer PENTATRAP, containing a tower of five Penning traps. A 25-channel voltage source with a relative stability of few 10^{-8} over a period of 10 minutes in the range of 0 to $-100\,\mathrm{V}$ is mandatory for PENTATRAP aiming for mass measurements with relative mass uncertainties of $\leq 10^{-11}$. Mass values with such a high precision allow for stringent tests of quantum electrodynamics in strong electric fields, testing Einstein's mass-energy relation $E = mc^2$ as well as measurements of decay energies (Q-values) with applications in neutrino physics.

Zusammenfassung

Atomare Massen und somit die Bindungsenergien von Nukliden sind für Kernstrukturuntersuchungen von großer Bedeutung, da darin alle Kernwechselwirkungen widergespiegelt werden. Im Rahmen der vorliegenden Arbeit wurden die Massen von sieben Nukliden, und zwar ^{194}Au, ^{194}Hg, ^{190,193,198}Tl und ^{202,208}Pb, am Penningfallen-Massenspektrometer ISOLTRAP an ISOLDE/CERN bestimmt.
Die Region der Thalliumisotope auf der Nuklidkarte ist von besonderem Interesse, da sie zahlreiche Kernstruktureffekte, wie Isomere mit kleiner Anregungsenergie, Zustandsinversion, Formkoexistenz und Kerndeformationen aufweist. Diese Effekte können mit Hilfe von Massendifferenzen, wie z.B. der Zweineutronenseparationsenergie oder den sogenannten empirischen Paarungslücken, untersucht werden.
Darüber hinaus befasst sich die vorliegende Arbeit mit einer ultra-stabilen Spannungsquelle mit dem Namen StaReP (**Sta**ble **Re**ference for **P**enning Trap Experiments), die am Max-Planck-Institut für Kernphysik entwickelt wurde. StaReP ist eine der Schlüsselkomponenten des Hochpräzisionsmassenspektrometers PENTATRAP, das einen Turm bestehend aus fünf Penningfallen enthält. Eine 25-Kanal-Spannungsquelle mit einer relativen Stabilität von wenigen 10^{-8} in einem Zeitraum von 10 Minuten in einem Bereich von 0 bis $-100\,\mathrm{V}$ ist für PENTATRAP-Experimente zwingend erforderlich, da Massenmessungen mit relativen Unsicherheiten von $\leq 10^{-11}$ angestrebt werden. Massenmessungen mit einer solch hohen Präzision ermöglichen u. a. Tests der Quantenelektrodynamik in starken elektrischen Feldern, die Überprüfung der Einsteinschen Masse-Energie-Relation $E = mc^2$ sowie Messungen von Zerfallsenergien (Q-Werte), die Anwendung in der Neutrinophysik finden.

Contents

1 Introduction **13**

I Theory **17**

2 Basics of Penning-Trap Mass Spectrometry **19**
2.1 The Ideal Penning Trap 19
2.2 The Real Penning Trap 23
2.2.1 Ion Excitation 25
2.2.2 Cooling Techniques 26
2.2.3 Detection Techniques 29

3 Nuclear Mass Models **33**
3.1 Nuclear Models 33
3.2 Finite-Difference Mass Formulas for Nuclear Structure Studies 38
3.3 The Nuclear Charge Radius 42

II Experimental Setup and Results **45**

4 ISOLDE and the Penning-Trap Experiment ISOLTRAP **47**
4.1 The ISOLDE Facility 47
4.2 The Experimental Setup of ISOLTRAP 49
4.2.1 Ion Production and Beam Preparation 49
4.2.2 The Tandem Penning-Trap System 51
4.2.3 Ion Detection for Mass Measurements 53
4.2.4 The Decay-Spectroscopy Setup 54

5 ISOLTRAP Mass Data **55**
5.1 Principle of the Mass Determination 55
5.1.1 Contributions to the Uncertainty 56
5.1.2 The Atomic Mass Evaluation 57
5.2 Results 58
5.3 Discussion 61

6 The PENTATRAP Mass Spectrometer **71**
6.1 The Experimental Setup of PENTATRAP 71
6.1.1 Ions Sources 71
6.1.2 Beamline and Beam Diagnostics 74
6.1.3 The Cryogenic Assembly and the Trap Tower 75
6.1.4 The PENTATRAP Control and Data Aquisition System 76
6.1.5 Ion Detection 76
6.1.6 The Measurement Principle 77
6.2 Stabilization Systems at PENTATRAP 79
6.2.1 The Setup of the Helium Pressure and Level Stabilization System . 81
6.2.2 Commissioning of the Helium Pressure and Level Stabilization System 85
6.2.3 Outlook 86

7 StaReP – an Ultra-Stable Voltage Source **87**
7.1 Requirements 87
7.2 System Architecture 89
7.3 Characterization of StaReP 96
7.3.1 Test Measurements in the PENTATRAP Laboratory 97
7.3.2 Test Measurements with Ions at $-7.5\,\mathrm{V}$ and $-89\,\mathrm{V}$ 97
7.3.3 Thermal Characteristic 97
7.3.4 Noise Characteristic 102
7.3.5 Summary 103

8 Summary and Outlook **105**

A Technical Drawings and Photographs **109**

List of Figures

2.1 Schematic of a hyperbolical and a cylindrical Penning trap 20
2.2 Ion trajectory in a Penning trap 21
2.3 Dipole and quadrupole excitation 25
2.4 Radial conversion 27
2.5 Buffer-gas cooling 28
2.6 Time-of-flight detection technique 30
2.7 Fourier transform-ion cyclotron resonance technique 30

3.1 Binding energy per nucleon 34
3.2 Deviation from the Weizsäcker mass formula 35
3.3 Nuclear shell structure 37
3.4 Neutron separation energy 39
3.5 Two-neutron separation energy 40
3.6 Empirical pairing gap $\Delta^3_{\mathrm{n}}(Z,N)$ 41
3.7 Empirical pairing gap $\Delta^5_{\mathrm{n}}(Z,N)$ 42

4.1 ISOLDE experimental hall 48
4.2 Elements at ISOLDE 49
4.3 Experimental setup of ISOLTRAP 50
4.4 Preparation Penning trap 52
4.5 Cooling resonance 52
4.6 Precision Penning trap 53
4.7 Time-of-flight ion-cyclotron resonance of ^{133}Cs 54

5.1 Mass-excess values 59
5.2 Time-of-flight ion-cyclotron resonance of $^{193}\mathrm{Tl}^m$ 61
5.3 Empirical pairing gap $\Delta^3_{\mathrm{n}}(Z,N)$ in the thallium region 63
5.4 Empirical pairing gap $\Delta^3_{\mathrm{n}}(Z,N)$ compared to theory 63
5.5 Differences of mean-square nuclear charge radii compared to theory 64
5.6 Differences of mean-square nuclear charge radii in the thallium region . . . 66
5.7 Empirical pairing gap $\Delta^5_{\mathrm{n}}(Z,N)$ in the thallium region 66
5.8 Two-neutron separation energies in the thallium region 67
5.9 Slope of the empirical pairing gap compared to the γ-parameter 68
5.10 Excitation energies of thallium and gold 70

6.1 Experimental setup of PENTATRAP . . . 72
6.2 Osmium spectrum . . . 73
6.3 Beam diagnostic system . . . 74
6.4 Cryogenic assembly and the trap tower . . . 75
6.5 Measurement principle at PENTATRAP . . . 78
6.6 Photograph of the PENTATRAP magnet . . . 80
6.7 Principle of the helium pressure and stabilization system . . . 82
6.8 Overview of the helium pressure and stabilization system . . . 83
6.9 Photograph of the valve system . . . 84
6.10 Level stability . . . 86

7.1 Photograph of StaReP . . . 90
7.2 Schematic of StaReP . . . 91
7.3 Shielding concept . . . 92
7.4 Photograph of a StaReP channel . . . 93
7.5 Precision and ramping DAC . . . 95
7.6 StaReP control . . . 95
7.7 User interface . . . 96
7.8 Voltage stability at −48 V . . . 98
7.9 Voltage stability at −30 V . . . 99
7.10 Stability of the axial frequency . . . 100
7.11 Voltage stability at −89 V . . . 100
7.12 Thermal characteristic . . . 101
7.13 Noise spectrum . . . 102

A.1 Level resonator . . . 110
A.2 Absolute pressure reference . . . 111
A.3 Magnet safety valve . . . 112
A.4 StaReP transformer . . . 113

List of Tables

2.1 Ion frequencies 22

5.1 Parameters of experimental campaigns 58
5.2 Overview of the data evaluation 59

7.1 Trapping voltages for different ion species 88
7.2 Parameters of the voltage source 88
7.3 Parts and functionality of StaReP 89
7.4 Components 94

Chapter 1

Introduction[1]

Atomic masses are important input parameters of many physics applications [2–4]. According to Einstein's famous mass-energy relation $E = mc^2$ [5] the atomic mass is inherently connected with the energy of the complete system, and from there to the binding energy. The binding energy, here the nuclear binding energy reflects all interactions acting in the nucleus. Atomic mass spectrometry allows to study different fields of physics, with varying levels of precision requirements depending on the field of interest. In order to identify ionic or molecular species a relative uncertainty of $\delta m/m \approx 10^{-5} - 10^{-6}$ is sufficient, whereas nuclear structure studies require a relative uncertainty of $\delta m/m \approx 10^{-6} - 10^{-8}$ depending on the application. This uncertainty was achieved within the present thesis, allowing one to study shell effects, empirical pairing gaps and deformation of nuclides. Relative uncertainties of $\leq 10^{-8}$ enable weak interaction studies, e. g. tests of the conserved-vector-current (CVC) hypothesis or the unitarity of the Cabbibo-Kobayashi-Maskawa (CKM) quark-mixing-matrix [6, 7]. Mass measurements relevant for neutrino physics [8, 9], tests of quantum electrodynamics (QED) [10, 11] or aspects of special relativity [12] are possible by means of mass-ratio measurements with an accuracy of a few parts in 10^{11} or better.

Introduction and History of Mass Spectrometry

At the beginning of the last century, J. J. Thomson discovered the existence of isotopes by passing ion beams through crossed electric and magnetic fields [13]. His student, F. W. Aston, studied the occurrence and abundances of isotopes and received in 1922 the Nobel Prize in Chemistry for *"his discovery by means of his mass spectrograph, of isotopes, in a large number of non-radioactive elements, and for his enunciation of the whole-number rule"*. This mass spectrograph was employed for systematic studies of more than 200 nuclides [14]. The relative uncertainty of 10^{-4} was sufficient to state the constancy of the binding energy of about 8 MeV per nucleon with a slight maximum at ^{56}Fe. This led to the development of the liquid drop model, which was proposed by G. Gamow [15], C. F. von Weizsäcker [16], H. A. Bethe and R. F. Bacher [17]. In the years following the invention of mass spectrometry, relative uncertainty could be decreased due to major technical

[1] Parts of the introduction are taken from the author's paper [1].

advances by about an order of magnitude every decade [2]. In the nineteen-fifties further improvements in mass spectrometry led to measurements with relative uncertainties of 10^{-7}. The results of these measurements gave hints to the shell structure of nuclides, which was proposed independently by J. H. D. Jensen and M. Goeppert-Mayer using the so-called independent-particle model [18–25]. Besides the improvements of classical mass spectrographs, further methods were developed to determine masses. Multipole electric and magnetic fields were employed for mass separation of ions. These developments led finally to the Penning trap. Pierce trapped charged particles in three dimensions by superimposing a homogeneous magnetic field with an electrical quadrupole field [26]. In the following years many ion detection and manipulation techniques were established and in 1989 H. G. Dehmelt and W. Paul shared the Nobel Prize in Physics for the *"development of the ion trap technique"* [27, 28]. Today, Penning-trap mass spectrometry is a very successful method [3], which finds applications in a broad range of physics. Penning-trap mass determination relies on the measurement of a frequency, which can be measured with very high accuracy. In the field of nuclear physics, there are worldwide about 20 Penning-trap mass spectrometry installations under construction or in operation. So far, a relative mass uncertainty for radioactive and stable nuclides of $\leq 10^{-8}$ [29–31] and $\leq 10^{-11}$ [32], respectively, could be demonstrated. In the following physics applications of the two mass spectrometers involved in the present work, namely ISOLTRAP and PENTATRAP, will be briefly introduced.

Nuclear Structure Studies

Nuclear structure describes the behavior of protons an neutrons in a nucleus and their arrangement in the nuclear shells. Today more than 3000 isotopes are known, whereas only about 300 of them are stable. In order to investigate the nuclear structure masses are determined employing Penning-trap experiments. The pioneering Penning-trap mass spectrometer at an online facility is the ISOLTRAP experiment [33,34] installed at ISOLDE/CERN [35]. The access to exotic nuclides allows one to contribute to a large variety of physics applications. Within the present thesis precise mass values in the neutron-deficient thallium region were obtained via the time-of-flight mass spectrometry technique [36] with a relative uncertainty reaching $\delta m/m \approx 2 \cdot 10^{-8}$. Nuclear binding energies of lead, thallium, mercury and gold were determined. Finite-difference mass formulas of the binding energy can be used to explore nuclear-structure effects. Illustrative is the commonly used two-neutron separation energy, which allows one to identify the shell structure of nuclides by sharp drops after the filling of neutron shells. Combining the results of mass measurements with mean-square nuclear charge-radii information from laser-spectroscopy studies can provide additional insights. In the case of neutron-deficient lead isotopes the mean-square nuclear charge radii exhibit a regular odd-even staggering. With just a few protons less, however, the isotopic chains of mercury and gold exhibit strong deformations towards the mid-shell around $N = 104$ [37]. Located between the spherical lead isotopes, and the mercury isotopes exhibiting shape staggering in the ground state, the thallium isotopes are particularly interesting.

A Novel Penning-Trap Mass Spectrometer: PENTATRAP

The PENTATRAP mass spectrometer [38] is currently under commissioning at the Max-Planck-Institut für Kernphysik (MPIK), Heidelberg. PENTATRAP aims at mass measurements with relative uncertainties of a few 10^{-12}, which will allow one to study physics questions at the highest level of precision, three of those will be described in the following. One motivation for the PENTATRAP experiment is carry out measurements which contribute to the determination of the mass of the electron antineutrino, being relevant for physics beyond the standard model of particle physics. The β^--decay of rhenium

$$^{187}\mathrm{Re} \;\rightarrow\; ^{187}\mathrm{Os} + e^- + \bar{\nu}_e \tag{1.1}$$

will be investigated by measuring the mass difference of ^{187}Re and its daughter nucleus ^{187}Os. Combining the mass difference with the results of microcalorimetric measurements of the endpoint spectrum [8] allows one to set an upper limit on the mass of the electron antineutrino. The decay of rhenium to osmium is a suitable case for these studies, as its total decay energy, the so-called Q-value, is very low (Q≈2.5 keV) [39]. Hence, the β^--decay results in radiation of a low-energy neutrino. Therefore, the relative contribution of the neutrino mass to the total neutrino energy is high, which results in a high sensitivity to the neutrino mass. This gives just one example of neutrino-oriented mass measurements based on studies of β-transitions.
Moreover, stringent tests of quantum electrodynamics in extreme electromagnetic fields can be carried out by determining the mass difference of an atom in different charge states. Thus, one can determine the electron binding energies. An interesting region, where such studies are carried out is Pb^{14+} to Pb^{36+}. No data are currently available and theoretical models show significant discrepancies [40].
Furthermore, a test of the relation $E = mc^2$ can be conducted by comparing the speed of light c_γ with the velocity of a massive particle c_m. A possible environment where this can be studied is the transition [12] of the neutron capture

$$^{A}X + n \;\rightarrow\; ^{A+1}X + \gamma. \tag{1.2}$$

Combining mass measurements of $m(^{A+1}X)$ and $m(^{A}X)$ with the detection of the released γ-energy employing crystal-diffraction spectrometry enables to test

$$\Delta m c_m^2 = h\frac{c_\gamma}{\lambda} \tag{1.3}$$

with h and λ being the Planck constant and the photon wavelength, respectively. S. Rainville [12] investigated sulfur and silicon, which lead to $1 - c_m/c_\gamma = 1.4(4.4) \cdot 10^{-7}$, whereas PENTATRAP is aiming at measurements of chlorine isotopes ^{35}Cl and ^{36}Cl. On the one hand it was demonstrated in [41], that the determination of E_γ is possible with a relative uncertainty of $5 \cdot 10^{-8}$ if sufficient statistics is accumulated. On the other hand, the neutron capture in the chlorine isotope ^{35}Cl is a promising reaction for these studies as the neutron cross section is higher compared to the transitions in sulfur or silicon.
These physics studies require a high accuracy, which can be achieved with an advanced

experimental setup in combination with highly-sensitive detection techniques. PENTATRAP is the first experimental setup consisting of a stack of five cylindrical Penning traps at cryogenic temperatures coupled to a source of highly charged medium-heavy and heavy ions such as hydrogen-like $^{208}Pb^{81+}$. As the achievable precision of the mass measurement scales with the charge-to-mass ratio access to highly charged ions from for example different electron beam ion traps (EBITs) is advantageous. The multiple Penning-trap setup in combination with a non-destructive detection system allows simultaneous measurements of frequencies of highly charged ions in adjacent traps. Thus, this provides a better control of systematic uncertainties and the one stemming from the ion-ion-interaction is negligible.
However, magnetic field fluctuations have to be minimized and therefore a tremendous effort has been invested in different configurations and conditions. One of the conditions is the stability of the trap environment, which is controlled with the stabilization system for the helium pressure and liquid helium level in the superconducting magnet. This system has been designed and partly setup within this thesis. For the ion storage a stable magnetic field but also an ultra-stable electric potential is indispensable. Ultra-stable in this context means, that the stability of the voltage source exceeds the stability of commercial sources in the required voltage range. Such an ultra-stable voltage source has been developed in this work in collaboration with the electronics workshop at MPIK and the Physikalisch Technische Bundesanstalt (PTB), Braunschweig. Besides the trapping potentials with a relative voltage stability of $\leq 4 \cdot 10^{-8}$ over a period of 10 minutes, the voltage source provides an option of dynamically changing voltages to facilitate adiabatic ion transport to adjacent traps being part of the measurement principle.

This thesis is structured as follows: In the first part the basics of Penning traps including ion storage, manipulation and detection will be discussed (Chap. 2). Then, mass formulas and applications thereof being relevant for nuclear structure studies will be presented (Chap. 3). The second part describes mass measurements performed at ISOLTRAP and new developments at PENTATRAP. The setup of ISOLTRAP will be described in Chapter 4. Chapter 5 contains the results of mass measurements for nuclear structure studies within the thallium isotopic chain. Finite-difference mass formulas will be introduced and their application in the mass region of interest is discussed. The setup of the novel Penning-trap mass spectrometer PENTATRAP will be subject of Chapter 6. Subsequently, an ultra-stable voltage source, which is one of the key components of the PENTATRAP experiment, will be introduced in Chapter 7. The thesis is concluded with a summary and an outlook in Chapter 8.

Part I

Theory

Chapter 2

Basics of Penning-Trap Mass Spectrometry

In the nineteen-thirties, F. M. Penning used a homogeneous magnetic field in order to increase the sensitivity of ionization vacuum gauges [42]. As the magnetic field was perpendicular to the momentum of the charged particle a two-dimensional confinement was achieved. In the late nineteen-fourties, J. R. Pierce described the first Penning trap by the combination of the homogeneous magnetic field with an electrostatic trapping potential [26]. Further developments of the ion trapping technique were achieved by H. G. Dehmelt and W. Paul [27, 28].
Penning-trap mass spectrometry relates frequency measurements with mass determinations, which is advantageous as a frequency is currently the quantity which can be measured most precisely [43]. The introduction of Penning traps led to tremendous improvements of precision in mass spectrometry as the ions can be manipulated in a well-controlled environment. The present chapter introduces ideal and real Penning traps as well as ion manipulation, ion cooling and different detection techniques being relevant for the Penning-trap experiments involved in this thesis.

2.1 The Ideal Penning Trap

Penning traps are ideal tools to store charged particles by means of static electromagnetic fields. The ions are confined in two dimensions by a strong homogeneous magnetic field $\vec{B} = B\hat{e}_z$. Without loss of generality the magnetic field is aligned along the $\hat{z}$-axis. For storage in the third dimension an electric quadrupole field is created by employing an electrode configuration as shown in Fig. 2.1 and applying a voltage between the ring electrode and the endcaps. In the ideal case, these electrodes would be infinitly expanded electrodes of hyperboloidal shape. Thus, a harmonic trapping potential is provided in axial direction. Ions with charge q in an ideal Penning trap experience the total force

$$\begin{aligned} \vec{F}_{\text{total}} &= \vec{F}_{\text{Lorentz}} + \vec{F}_{\text{el}} \\ &= q(\dot{\vec{r}} \times \vec{B}) + q\vec{E}(\vec{r}), \end{aligned} \tag{2.1}$$

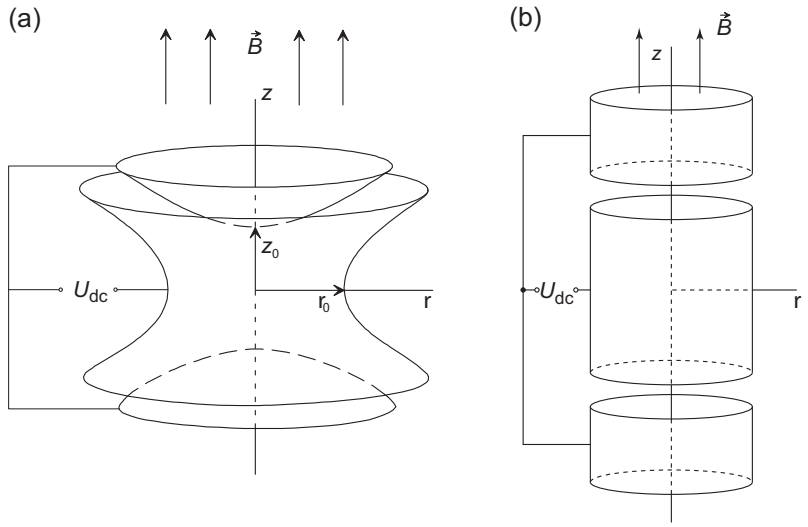

Figure 2.1: Schematic of (a) a hyperbolical and (b) a cylindrical Penning trap. The trapping potential is created by applying a voltage U_{dc} between the ring electrode and the endcaps. Radial confinement of the ion is achieved due to the superimposed homogeneous magnetic field in z-direction. The minimum distances from the trap center are indicated by z_0 in axial direction and r_0 in radial direction. Taken from [2].

with

$$\vec{F}_{\mathrm{el}} = -q\vec{\nabla}U(\vec{r}). \tag{2.2}$$

The potential $U(\vec{r})$ is given by

$$U(\vec{r}) = U(r,z) = \frac{U_0}{2d^2}\left(z^2 - \frac{r^2}{2}\right), \tag{2.3}$$

with the trap geometry parameter

$$d^2 = \frac{1}{2}\left(z_0^2 + \frac{1}{2}r_0^2\right). \tag{2.4}$$

The minimum distance from the center of the trap to the ring and the endcap electrodes is given by r_0 and z_0, respectively. Within the magnetic field B charged particles with mass m perform a circular motion according to

$$\omega_{\mathrm{c}} = \frac{q}{m}B, \tag{2.5}$$

which is called the free cyclotron frequency. Due to $\vec{B} = B\hat{e}_z$ we can replace $\hat{B}$ in Eq. (2.1) by Eq. (2.5) and plug in Eq. (2.2), which results in the equations of motion in radial and

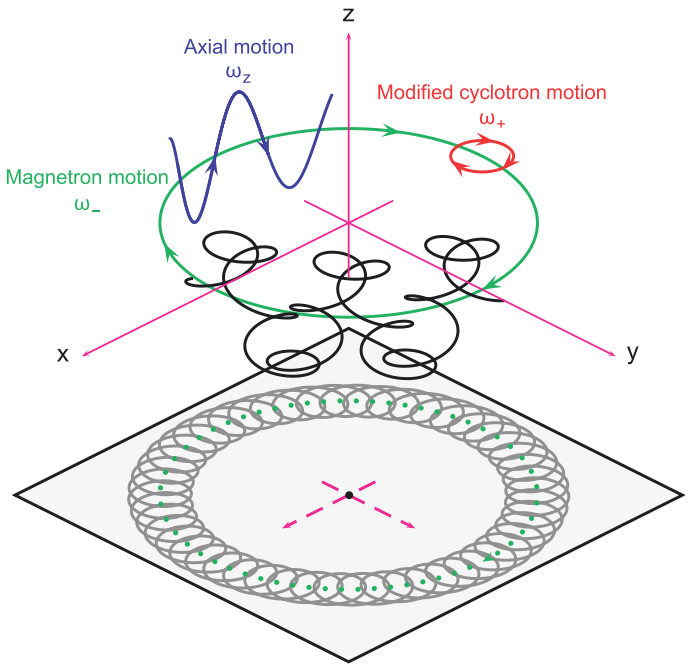

Figure 2.2: The ion trajectory in a Penning trap consists of a superposition of three eigenmotions: the magnetron motion (green), the axial motion (blue) and the modified cyclotron motion (red). The black line illustrates the superposition of all three eigenmotions. The lower part shows a 2D projection of the eigenmotion on the radial plane. Adapted from [2].

axial direction:

$$\ddot{x} = \dot{y}\omega_c + \frac{1}{2}\left(\frac{qU_0}{md^2}\right)x, \tag{2.6}$$

$$\ddot{y} = -\dot{x}\omega_c + \frac{1}{2}\left(\frac{qU_0}{md^2}\right)y, \tag{2.7}$$

$$\ddot{z} = -\left(\frac{qU_0}{md^2}\right)z. \tag{2.8}$$

In the case of ideal Penning traps, the ion motion in axial direction is decoupled from the radial components of the ion motion (see Fig. 2.2) and can be described as a harmonic oscillator. The coefficient in Eq. (2.8) is identified with the squared oscillation frequency:

$$\omega_z = \sqrt{\frac{qU_0}{md^2}}. \tag{2.9}$$

For the radial components the ansatz $u = x + iy$ with $u = e^{-iwt}$ yields:

$$\omega^2 - \omega_c \cdot \omega + \frac{1}{2}\omega_c^2 = 0, \tag{2.10}$$

Table 2.1: Typical frequencies at PENTATRAP ($B = 7\,\mathrm{T}$) for a highly charged osmium ion $^{187}\mathrm{Os}^{45+}$ and at ISOLTRAP ($B = 5.9\,\mathrm{T}$) for a singly charged cesium ion $^{133}\mathrm{Cs}^{+}$ are listed.

	$^{187}\mathrm{Os}^{45+}$	$^{133}\mathrm{Cs}^{+}$
$\omega_\mathrm{c}/2\pi$	25.87 MHz	683 kHz
$\omega_+/2\pi$	25.86 MHz	682 kHz
$\omega_\mathrm{z}/2\pi$	600 kHz	38 kHz
$\omega_-/2\pi$	6.96 kHz	1.08 kHz

which is solved by the radial eigenfrequencies:

$$\omega_\pm = \frac{1}{2}\left(\omega_\mathrm{c} \pm \sqrt{\omega_\mathrm{c}^2 - 2\omega_\mathrm{z}^2}\right). \tag{2.11}$$

The free cyclotron frequency and the eigenfrequencies for ions stored in the precision trap of ISOLTRAP or in the PENTATRAP experiment using a magnetic field strength of 5.9 T and 7 T, respectively, are listed in Tab. 2.1. In order to store the ions the trapping conditions $\omega_c^2 > 2\omega_z^2$ and $qU_0 > 0$ must be fulfilled. In first order, the Taylor expansions for Eq. (2.11) lead to:

$$\omega_+ \approx \omega_\mathrm{c} - \frac{U_0}{2d^2B}, \tag{2.12}$$

$$\omega_- \approx \frac{U_0}{2d^2B}, \tag{2.13}$$

which shows that the magnetron frequency ω_- is in first order mass independent. The magnitudes of the eigenfrequencies are ordered such that $\omega_- < \omega_z < \omega_+$. For Penning-trap mass spectrometry the following relations are of importance:

$$\omega_\mathrm{c} = \omega_+ + \omega_-, \tag{2.14}$$

$$\omega_\mathrm{c}^2 = \omega_+^2 + \omega_\mathrm{z}^2 + \omega_-^2, \tag{2.15}$$

$$\omega_\mathrm{z}^2 = 2\omega_+\omega_-. \tag{2.16}$$

Note, that Eq. (2.14) is only true for ideal Penning traps, while Eq. (2.15) is more robust and also holds for Penning traps with imperfections. This relation is called the invariance theorem, which is discussed in detail in [44].

In a quantum mechanical picture, the three eigenmotions of an ion can be treated as three harmonic oscillators. The total energy of an ion stored in a Penning trap can be expressed by

$$E_\mathrm{total} = E_+ + E_\mathrm{z} + E_-, \tag{2.17}$$

with E_+, E_z, E_- being the energies in the corresponding eigenmodes. Describing the total energy of a spin-less particle [45] yields:

$$E_\mathrm{total} = \hbar\omega_+\Big(n_+ + \frac{1}{2}\Big) + \hbar\omega_\mathrm{z}\Big(n_\mathrm{z} + \frac{1}{2}\Big) - \hbar\omega_-\Big(n_- + \frac{1}{2}\Big) \tag{2.18}$$

with principle quantum numbers n_+, n_z, n_-. Note the negative sign of the magnetron energy, which means that an increase in the quantum number n_- decreases the total energy. This is of importance for the buffer-gas cooling technique, which will be explained in Chap. 2.2.2.

2.2 The Real Penning Trap

So far, only the behavior of a single stored particle in the ideal Penning trap has been described. In a real experiment the trap electrodes themself as well as the environmental conditions affects the electric and the magnetic field. Thus the eigenmotions are coupled and frequencies are shifted. Details are discussed in [44, 46]. In the following electric and magnetic field imperfections as well as the influence of particle-particle interactions will be described.

Electric Field Imperfections

Several aspects result in an imperfect electrical field in the Penning trap, i. e. deviations from the harmonic potential. Apart from the fact that the ring electrodes are segmented in order to allow for the manipulation of the ion motion (see Chap. 2.2.1), the endcaps of hyperbolical Penning traps exhibit openings for particle in- and ejection. An alternative electrode configuration is the cylindrical Penning trap (see Fig. 2.1 (b)), which enables fast ion transfer between adjacent traps. On the one hand, cylindrical trap electrodes are more practical to produce. On the other hand, the ideal potential in a cylindrical trap can only be approximated in a limited trap volume, which is small compared to the region of the harmonic potential in a hyperbolical Penning trap.
In addition field imperfections due to finite, not perfectly fabricated electrodes as well as impurities of the trap material disturb the ideal trapping potential. Furthermore, slight misalignments of the electrodes yield an anharmonic potential. To achieve a potential, which is as harmonic as possible, real Penning traps are equipped with so-called correction electrodes inserted between the endcaps and the ring electrode. Moreover, ions are stored close to the trap center, where the potential [47] is approximately given by

$$\begin{aligned}\Phi(\rho,z) =& \frac{1}{2}U_0\left[\frac{C_2}{d^2}\left(z^2+\frac{\rho^2}{2}\right)+\frac{C_4}{d^4}\left(z^4-3z^2\rho^2+\frac{3}{8}\rho^4\right)\right.\\ &\left.+\frac{C_6}{d^6}\left(z^6-\frac{15}{2}z^4\rho^2+\frac{45}{8}z^2\rho^4-\frac{5}{16}\rho^6\right)+...\right].\end{aligned} \tag{2.19}$$

Due to the mirror symmetry in z-direction odd terms can be neglected. In the case of an ideal trap $C_2 = 1$ and $C_i = 0, i \neq 2$. However, for a real trap higher order coefficients, in particular C_4 and C_6, have to be considered. They lead to a shift in the sum frequency

(Eq. (2.14)) [47] of

$$\Delta\omega_c^{el} = \frac{\omega_z^2}{\omega_+ - \omega_-}\left[\frac{3}{4}\frac{C_4}{z_0^2}\left(\rho_+^2 - \rho_-^2\right) + \frac{15}{8}\frac{C_6}{z_0^4}\left(3\rho_z^2\left(\rho_-^2 - \rho_+^2\right) + \left(\rho_+^4 - \rho_-^4\right)\right)\right]. \tag{2.20}$$

This shift is in first order mass independent. By choosing a suitable geometry and tuning the voltage applied to the correction electrodes, the C_4 and the C_6 term and thus the corresponding shift can be minimized.
In addition, a shift of eigenfrequencies occurs for reasons such as trap misalignment, such that the magnetic field axis is not parallel to the electrical field axis. In case, the cyclotron frequency is determined via $\omega_c \approx \omega_+ + \omega_-$, it leads to a frequency shift, whereas this effect cancels out when ω_c is determined via the invariance theorem (Eq. (2.15)). For small tilting angles $\theta \ll 1$, where θ represents the angle between the magnetic field axis and the electrical field, and small ellipticities $\epsilon \ll 1$, which appear as imperfections of the rotational symmetry, the frequency shift is described by

$$\Delta\omega_c^{tilt} \approx \omega_-\left(\frac{9}{4}\theta^2 - \frac{1}{2}\epsilon^2\right). \tag{2.21}$$

A detailed discussion can be found in [48].

Magnetic Field Imperfections

Magnetic field imperfections are one of the main issues, which limit the precision in Penning-trap mass measurements. Employing a superconducting magnet, there are four different contributions, which affect the stability and homogeneity of the magnetic field. Firstly, one has to take into account that the size of the coils of the magnet is finite and thus the homogeneity is limited. A second reason occurs due to impurities in the material of the coils. These are responsible for the so-called flux creep effect [49, 50], which causes a decrease of the magnetic field over time. Moreover, the susceptibility of the Penning-trap electrodes is non-zero and ferromagnetic or paramagnetic materials or impurities in the materials in the vicinity of the trap result in magnetic field distortions. Additionally, one has to consider pressure and thus temperature fluctuations in the liquid helium and liquid nitrogen reservoir of the magnet because these fluctuations influence the temperature-dependent susceptibilities of the materials close to the Penning trap and thus the magnetic field is disturbed.
The magnetic field in a Penning trap is usually very stable in a small region at the trap center. At the ISOLTRAP experiment the temporal stability is $\delta B/\delta t \cdot 1/B < 2 \cdot 10^{-9}$/h, while at PENTATRAP a stabilization system aiming for $\delta B/\delta t \cdot 1/B$ of few ten 10^{-12}/h will be implemented.

Ion-Ion Interaction

In an ideal case only one ion is stored in a Penning trap. The presence of additional ions leads to shifts in the eigenfrequencies due to space charge effects. The harmonic trapping potential is superimposed with the potential due to Coulomb interactions of the stored

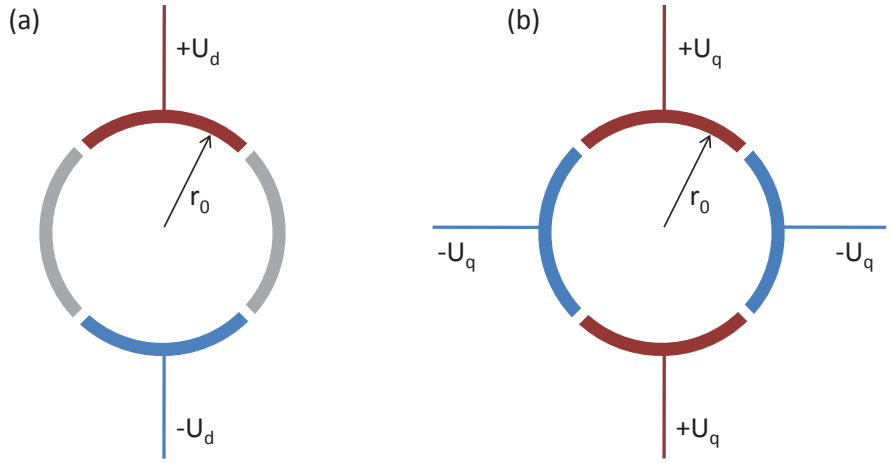

Figure 2.3: The segmentation of the ring electrode allows one to apply dipolar or quadrupolar excitations. A dipolar field (a) is obtained by applying the rf field to two diametrical ring segments, whereas a quadrupolar excitation (b) is the result of an rf field applied to two pairs of 90° rotated ring segments. Adapted from [2].

particles. The storage of ions with different charge-to-mass ratios leads to effects, which depend on the mass difference between the ion species. For small differences, which are too close to be resolved the time-of-flight spectrum (see Chap. 2.2.3) shows a single resonance with a width, which is smaller than the expected width of the superposition of two resonances. In the case of a high mass difference, two resonances are resolved, but both centers are shifted to lower frequencies in comparison to the unperturbed frequencies. This shift depends on the number of stored ions. Details of these effects are described in [51].

2.2.1 Ion Excitation

Ions stored in a Penning trap can be manipulated by applying radiofrequency (rf) excitations to the trap electrodes. Different excitation schemes are used for the detection of the ions or the elimination of unwanted ion species. Furthermore it is possible to couple two eigenmodes and thus transfer energy from one to another mode similar to the behavior in a coupled harmonic oscillator.

Dipolar Excitation

As the magnetron frequency is mass independent to first order, an excitation with $\omega_{\mathrm{rf}} = \omega_-$ will affect ions of various masses. To increase the radius of only a certain ion species, dipolar excitations with $\omega_{\mathrm{rf}} = \omega_+$ or $\omega_{\mathrm{rf}} = \omega_z$ are applied. This can be achieved by applying voltages with a 180° phase-shift to two diametrical electrodes as shown in Fig. 2.3 (a). A

dipolar excitation at $\omega_{\mathrm{rf}} = \omega_{\pm}$ results in a field

$$\vec{E}_{\mathrm{x}} = \frac{U_{\mathrm{d}}}{d} \cdot \cos(\omega_{\mathrm{rf}} t - \phi_{\mathrm{rf}}) \hat{x}, \tag{2.22}$$

which affects the radial eigenmodes, whereas an rf excitation at the endcaps with $\omega_{\mathrm{rf}} = \omega_z$ yields

$$\vec{E}_{\mathrm{z}} = \frac{U_{\mathrm{d}}}{d} \cdot \cos(\omega_{\mathrm{rf}} t - \phi_{\mathrm{rf}}) \hat{z}, \tag{2.23}$$

which increases the amplitude of the ion motion in axial direction. U_{d} denotes the amplitude of the dipolar rf voltage and d indicates the characteristic trap dimension (see Eq. (2.4)).

Quadrupolar Excitation

The coupling of two eigenmodes allows one to transfer energy from one mode to another, which is required for many detection and cooling techniques. A quadrupolar excitation at the sum or difference of the corresponding frequencies leads to the coupling of the eigenmotions. As illustrated in Fig. 2.3 (b) the rf field with 180° phase shift is applied to two pairs of e. g. ring electrode segments being rotated by 90° to each other. To couple the radial modes an rf field of

$$\vec{E}_{\mathrm{x}} = \frac{2U_{\mathrm{q}}}{d^2} \cdot \cos(\omega_{\mathrm{rf}} t - \phi_{\mathrm{rf}}) \cdot y \cdot \hat{x}, \tag{2.24}$$

and

$$\vec{E}_{\mathrm{y}} = \frac{2U_{\mathrm{q}}}{d^2} \cdot \cos(\omega_{\mathrm{rf}} t - \phi_{\mathrm{rf}}) \cdot x \cdot \hat{y} \tag{2.25}$$

results in the case of $\omega_{\mathrm{rf}} = \omega_+ + \omega_-$ in a full conversion between the magnetron and the cyclotron radii (see Fig. 2.4) [52]. If the excitation frequency is not fulfilling the condition $\omega_{\mathrm{rf}} = \omega_+ + \omega_-$ the conversion is incomplete.

2.2.2 Cooling Techniques

In general cooling techniques are used to reduce the motional amplitudes or, in a quantum-mechanical picture, lowering the quantum numbers of the particles stored in a Penning trap. Low motional amplitudes are desired to keep the ions close to the harmonic region in the trap center. Moreover, the ion beam transport of a cooled ion sample is easier and more efficient due to its low energy spread. An overview of different cooling techniques is given in [2, 53]. Two of the common cooling techniques applied in Penning-trap mass spectrometry will be described in the following.

Buffer-Gas Cooling Technique

For high-precision mass measurements it is important to prepare the ions. A cooling method for ions, which is applied at the ISOLTRAP experiment, is the mass-selective

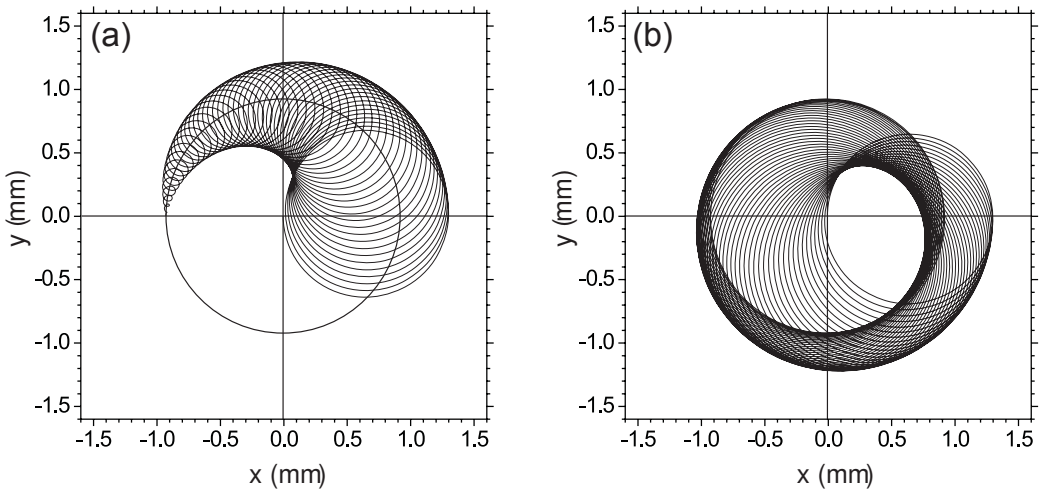

Figure 2.4: The application of a quadrupolar excitation with $\omega_{\mathrm{rf}} = \omega_+ + \omega_-$ yields a conversion from a pure magnetron motion in a pure cyclotron motion. (a) shows the first part of the conversion, starting at a high magnetron amplitude. The second part (b) illustrates the further decreasing magnetron and increasing cyclotron amplitude. Taken from [2].

buffer-gas cooling technique [54]. Ions stored in a buffer-gas filled Penning trap reduce their kinetic energy by collisions with the buffer-gas atoms. Usually, helium serves as buffer gas due to its high ionization potential to prevent charge exchange. The pressure in the buffer-gas filled ISOLTRAP preparation trap is about 10^{-4} mbar. Ions cool until a thermal equilibrium with the buffer gas is achieved. The damping force $\vec{F}$ can be approximated in a viscous drag approach with

$$\vec{F} = -\delta m\vec{v} \tag{2.26}$$

with $m\vec{v}$ being the ion momentum and δ the damping parameter. This parameter depends on the ion's charge-to-mass ratio q/m and can be expressed as

$$\delta = \frac{q}{m \cdot K_{\mathrm{ion}}} \frac{p/p_{\mathrm{N}}}{T/T_{\mathrm{N}}} \tag{2.27}$$

with K_{ion} being the ion mobility at room temperature, whereas p/p_{N} and T/T_{N} denote the pressure and temperature in units of normal pressure and normal temperature, respectively.
Figure 2.5 shows the resulting ion trajectories in a plane perpendicular to the magnetic field axis. The evolution of the magnetron and cyclotron motion can be described by

$$\rho(t) = \rho_0 \cdot e^{-\alpha t}. \tag{2.28}$$

Here, ρ_0 denotes the initial amplitude of the corresponding motion whereas the damping constant α for the magnetron and cyclotron is given as

$$\alpha = \pm\delta \frac{\omega_\pm}{\omega_+ - \omega_-}. \tag{2.29}$$

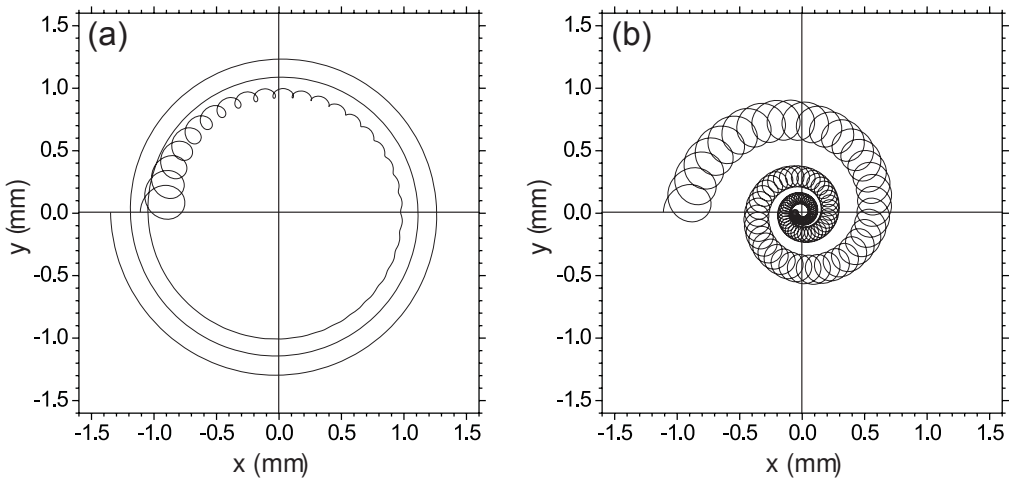

Figure 2.5: Theoretical trajectories of ions in the x-y-plane in a Penning trap filled with buffer gas. The center of the trap is indicated by the cross. In (a) a fast damping of the cyclotron motion combined with a slow increase of the magnetron motion is visible. In (b) the mass-selective centering, which is achieved by applying an azimuthal excitation at $\omega_{\mathrm{rf}} = \omega_+ + \omega_-$, is plotted. The radius of both radial motions (magnetron and cyclotron) is reduced. Taken from [2].

The negative sign leads to an increase of the magnetron radius. A frequency-dependent and hence mass-selective conversion of the magnetron into cyclotron motion, by applying an azimuthal excitation with $\omega_{\mathrm{rf}} = \omega_+ + \omega_-$, is applied to recenter the ions of interest. The extraction of the ions out of the trap through a small hole in the endcap results in a loss of the ions on larger magnetron radii than the extraction opening as they hit the trap electrode.

Resistive Cooling Technique

A cooling method, which is suitable for single-ion experiments at cryogenic temperatures like PENTATRAP, is the resistive cooling technique. The motional energy of an ion in a Penning trap can be reduced by energy dissipation over the resistance of an external tank circuit, which is connected to the trap electrodes and with a resonance frequency tuned to the ion's eigenfrequency. Thus, the energy of the ion is damped until it reaches thermal equilibrium with the tank circuit. If the circuit is hold at 4 K by cooling it with liquid helium, corresponding energies can be achieved.
Assuming that the ion is oscillating between two infinite plates, the image charge current

$$i = \frac{qv}{d} \tag{2.30}$$

induced by the ion with charge q depends on the distance d of the two plates and the velocity v of the ion. The current flows through the tank circuit with resistance R and

the energy dissipation of i^2R per unit time can be written as:

$$\frac{dE}{dt} = -i^2R = -R\frac{q^2}{d^2}v^2 = -R\frac{q^2}{d^2}\frac{E}{m} = -\frac{1}{\tau}E. \tag{2.31}$$

Accordingly, the energy evolution of the ion can be described as $E(t) = E_0 \cdot exp(-1/\tau \cdot t)$ with the cooling time constant

$$\tau = \frac{md^2}{Rq^2}. \tag{2.32}$$

Resistive cooling is a very efficient technique for ions with a high charge-to-mass ratio leading to low time constants. However, in case of short-lived ions this technique is not feasible due to the limited half-life. For those ions the buffer-gas cooling technique is applied.
The resistive cooling technique allows one to address the axial and the modified cyclotron motion. Cooling the magnetron motion would lead to higher amplitudes and thus to a loss of the ions. Instead, the magnetron motion can be cooled by coupling it with an rf field as described in Chap. 2.2.1 either to the axial or the cyclotron motion.

2.2.3 Detection Techniques

Different ion detection techniques are available in the field of Penning-trap mass spectrometry. Two commonly used methods, which are suitable for both the ISOLTRAP or the PENTATRAP experiment, will be introduced in the following.

Time-of-Flight Detection Technique

The time-of-flight ion-cyclotron resonance (TOF-ICR) detection technique [36] is a destructive detection method based on the interaction of the magnetic moment $\vec{\mu}$ of the ions of interest with the magnetic field gradient $\frac{\partial \vec{B}}{\partial z}$. Since the ions are lost after each experimental cycle, a new loading process of the Penning trap is required for every excitation frequency of the frequency scan. The trapped ions are first excited by applying an rf field with $\omega_{\mathrm{rf}} = \omega_-$ in order to prepare them on a well defined magnetron radius. Then, a quadrupolar excitation at or close to the resonance frequency is applied with $\omega_{\mathrm{rf}} = \omega_+ + \omega_-$ to obtain a conversion from the magnetron to the modified cyclotron motion. In resonance, the radial radius remains constant, but the radial kinetic energy connected with the magnetic moment $E = \vec{\mu}\vec{B}$ is increased, since $\omega_+ > \omega_-$. Then the ions are ejected out of the trap by lowering the potential of the endcap electrode. The ions are drifting along the magnetic field lines, and their initially lower axial energy increases due to the interaction with the magnetic field gradient (see Fig. 2.6). This leads to an increase in axial velocity of the ions passing the magnetic field gradient towards the detector. For each experimental cycle the quadrupolar excitation frequency is changed and for resonantly excited ions the time of flight reduces maximal due to the full conversion from the magnetron to the modified cyclotron motion. The time the ions need to fly from the trap to the detector is recorded and the minimal time of flight corresponds to the excitation at the cyclotron frequency ω_c of the ion of interest. The expected line shape is described by the $sinc(x)$

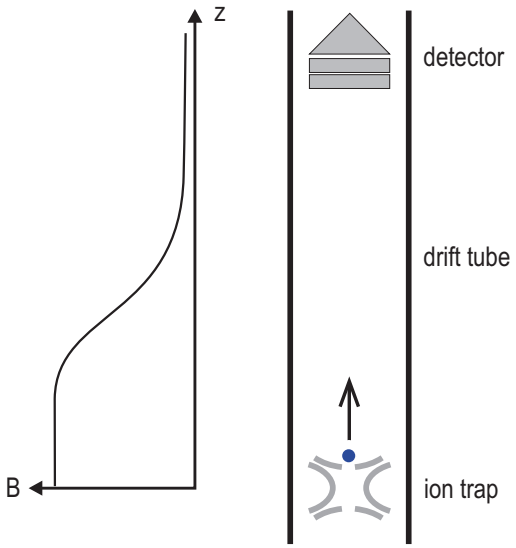

Figure 2.6: Schematic of the principle of the time-of-flight measurement technique. Ions are ejected out of the trap and drift through a magnetic field gradient, which is shown qualitatively on the left [36].

function and the fit of the experimental data as plotted in Fig. 4.3 shows that the data and the theoretical line shape are in agreement. The width of the line shape is Fourier limited by the quadrupolar excitation time and is an indicator for the resolving power.

Fourier-Transform Ion-Cyclotron Resonance Detection Technique

The Fourier-transform ion-cyclotron resonance (FT-ICR) technique [55] is based on the interaction of the ion with the trap electrodes and the detection of the induced signals. It is a non-destructive ion detection method, which allows to repeat a measurement several times without the need of loading the trap with a new ion in between. This is advantageous,

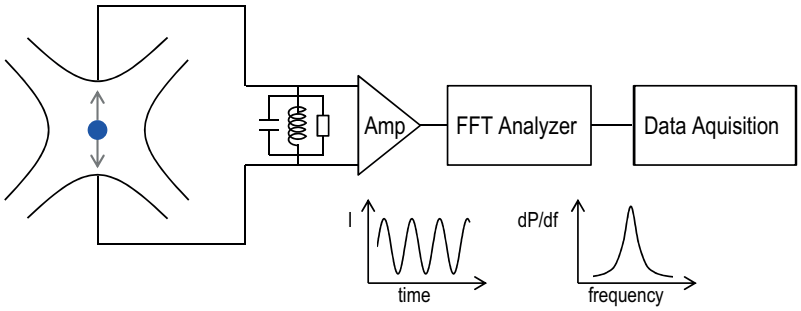

Figure 2.7: Schematic of the FT-ICR detection method. The ion oscillates between the trap electrodes and induces a tiny image charge current. This signal is amplified and then converted to a frequency signal by an FFT analyzer.

since it saves time and thus it is less sensitive to environmental fluctuations. Moreover, the FT-ICR technique enables the measurement of all three eigenfrequencies. Hence, the free cyclotron frequency can be deduced by employing the invariance theorem [44]. In a cryogenic environment, the FT-ICR technique provides single-ion sensitivity. The storage of a single ion is advantageous as frequency shifts caused by space charge effects are eliminated. A charged particle that oscillates between two infinitely extended plates of a capacitor induces image charges on the plates. When placing a high impedance between these plates, a current flows and causes a voltage drop across the impedance. This model can be applied to an ion oscillating at a certain eigenfrequency in the Penning trap, which induces image charges in the trap electrodes. This image charge within the concept of a closed circuit, leads to a current in the fA range (see Eq. (2.30)), which flows between the electrodes. The current is flowing trough the effective resistance of the tank circuit and the ion's energy is dissipated until thermal equilibrium is reached. The cooling time constant is given in Eq. (2.32). In order to detect the image current, it is amplified by means of a high impedance. Then, the voltage drop along this impedance is amplified by a low-noise amplifier to a value which can be detected with a fast fourier transform (FFT) analyzer. From the FFT of this time signal, which is picked up from a segment of a splitted Penning-trap electrode, the eigenfrequency of the ion is deduced. A schematic of the detection technique is shown in Fig. 2.7. The signal-to-noise ratio is given as

$$\frac{S}{N} = \frac{\sqrt{\pi}}{2}\frac{r_{\mathrm{ion}}}{D}q\sqrt{\frac{\nu}{\Delta\nu}}\sqrt{\frac{Q}{kTC}}, \tag{2.33}$$

where r_{ion} is the radius of the ion motion, D the effective electrode distance, q the charge of the ion, k the Boltzmann constant, ν the frequency and $\Delta\nu$ the spectral width. The temperature and capacity of the detection system is given by C and T, respectively. The signal-to-noise ratio increases with the quality factor of the tuned circuit Q.
The disadvantage of this detection method is the limitation to ions with relatively long half-lives. A frequency measurement lasts several seconds or even minutes and thus it is not possible to measure exotic nuclides with half-lives of only tens of ms.

Chapter 3

Nuclear Mass Models

High-precision mass measurements with relative uncertainties of $\delta m/m \leq 10^{-7}$ provide input for, e.g., nuclear structure or nuclear astrophysics studies. Mass data can be used to test the predictive power of mass models or to deduce input parameters for empirical mass formulas and to predict masses of unmeasured nuclides [56]. The mass measurements of exotic nuclides, i. e. nuclides far away from the stable and long-lived isotopes on the nuclear chart, are challenging as the half-lives and the production rates, which can be as low as one particle per second or below, are limiting the performance.
In recent years tremendous progress has happened in the field of modern mass formulas in order to extrapolate from the known mass region even up to the neutron drip line [57]. A brief summary of those models, focusing on those which are of importance for the mass region investigated within this thesis, will be given.

3.1 Nuclear Models

The mass of a nucleus with A nucleons is lower than the sum of the masses of its N neutrons and Z protons. This mass defect is directly linked to the binding energy by Einstein's mass-energy relation and can be expressed as

$$B(Z,N) = \Big(Z \cdot m_{\mathrm{p}} + N \cdot m_{\mathrm{n}} - m(Z,N)\Big)c^2, \tag{3.1}$$

with m_{p}, m_{n}, $m(Z,N)$ and c denoting the proton mass, the neutron mass, the mass of the nucleus and the speed of light, respectively. In 2012 more than 2400 nuclear masses were published in the Atomic Mass Evaluation AME2012 [58]. The binding energy per nucleon was extracted and is shown in Fig. 3.1 in red and black for stable and unstable nuclides, respectively.
The binding energy reflects the sum of all nucleonic interactions causing, amongst other effects, correlations in many-body systems. The detailed nuclear structure and thus the binding energy depends on the arrangement of protons and neutrons in the nucleus.
The discovery of the existence of isotopes by J. J. Thomson [13] triggered extensive studies on the abundances of isotopes performed by his student F. W. Aston. He employed a mass

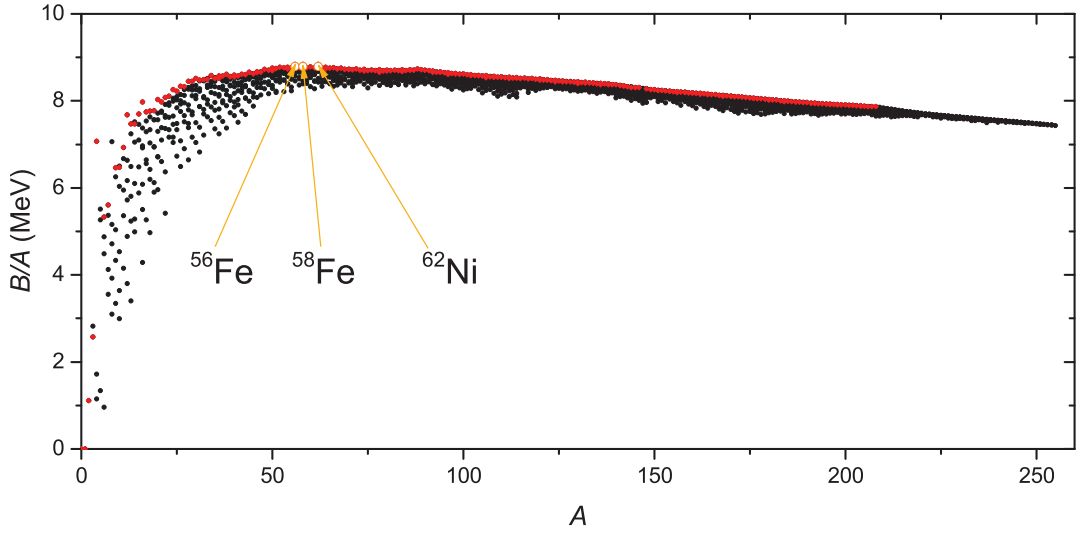

Figure 3.1: Binding energy per nucleon as a function of mass number A. The ^{56,58}Fe isotopes and the proton-magic ^{62}Ni isotope are the most strongly bound nuclides with $B/A \approx 8.8\,\mathrm{MeV}$ (orange). Other stable nuclides are indicated in red. Data were taken from AME2012 [58].

spectrograph to determine the masses of about 200 nuclides [14]. These studies revealed the trend of binding energies leading to the liquid drop model, which was initially proposed by G. Gamow in 1930 [15]. The nucleus was described by a drop of an incompressible nuclear liquid with a constant mass density. The liquid consists of protons and neutrons hold together by the strong nuclear charge-independent force. Further developments of this model gave rise to the first semi-empirical mass formula, the so-called Weizsäcker mass formula [16, 17]:

$$B(Z,N) = a_\mathrm{V} A - a_\mathrm{S} A^{2/3} - a_\mathrm{C} \frac{Z^2}{A^{1/3}} - a_\mathrm{A} \frac{(N-Z)^2}{A} - \delta(A,Z). \tag{3.2}$$

The constants a_V, a_S, a_C and a_A are empirically determined by a fit of Eq. (3.2) to experimental data. Weizsäcker's mass formula considers the following aspects:

- The volume term $a_\mathrm{V} A$ represents the energy, which is released when nucleons form the nucleus. It represents the major part of the binding energy and is proportional to the number of nucleons.

- The surface term $a_\mathrm{S} A^{2/3}$ is proportional to the surface of the nucleus. It reduces the binding energy due to the fact that nucleons at the surface on a nucleus interact with less neighboring nucleons and thus they are less bound.

- Another term, which lowers the binding energy, is the Coulomb term $a_\mathrm{C} \frac{Z^2}{A^{1/3}}$. It takes into account the repulsing interactions between protons and thus it scales with the proton number Z.

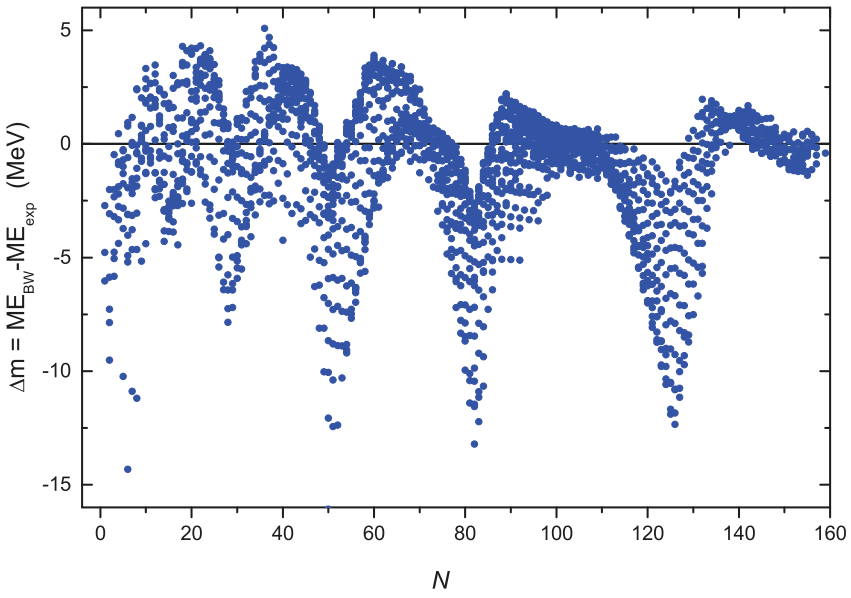

Figure 3.2: Mass differences Δm between predicted masses by H. A. Bethe and C. F. von Weizsäcker and experimental data. Adapted from [59].

- The asymmetry term $a_{\mathrm{A}}\frac{(N-Z)^2}{A}$ reduces the binding energy with increasing difference between proton and neutron number. This contribution vanishes for $N = Z$ nuclides.

- Even-even and odd-odd nuclides are more bound compared to odd-even and even-odd nuclides, the later two of which result in a negative sign of the pairing term $\delta(A, Z)$. For even-A nuclides the pairing term contributes positively to the binding energy.

This macroscopic model suggests a binding energy of about 8 MeV per nucleon. It works remarkably well for a large range of nuclides from $A > 30$ onwards. However, comparing theoretical predictions to mass data reveal a discrepancy at certain neutron and proton numbers as shown in Fig. 3.2. Later on these numbers were named magic numbers.
In order to account for the discrepancies between the model and the data microscopic descriptions are required. The deviations at magic numbers could be explained by the shell structure concept of the nucleus within the independent-particle model independently developed by J. H. D. Jensen and M. Goeppert-Mayer [18–25]. Apart from the shell structure also the pairing effect was described by the independent-particle model. J. H. D. Jensen and M. Goeppert-Mayer assumed the nucleons to move inside a potential well independently from other nucleons. As they neglected the nucleon-nucleon interaction, residual interactions had to be added to account for discrepancies. The potential was described by a mixture of a square well and a harmonic oscillator, which is also called the Woods-Saxon potential [60]. As it was not possible to reproduce the experimentally observed shell structure at certain neutron and proton numbers a spin-orbit term was added, which in turn led to the splitting of the energy levels. These are labeled as nl_j, which indicate

the principle quantum number n, the orbital quantum number l and the sum of the spin and the orbital quantum number $j = l \pm s$ (see Fig. 3.3). The energy levels resulting from this modified potential at the magic numbers reproduce the experimental data. The potential forms a set of single-particle levels, called subshells, which are filled according to the Pauli principle. The subshells cluster in groups, called shells, are separated by large energy gaps. If a shell is filled completely the nucleus is unexpected stable, i. e. the binding energy increases for these nuclides. The total number of protons or neutrons in the case of filled shells correspond to the magic numbers. If all shells or subshells are filled and there is one more nucleon, e. g. the valence nucleon, this single nucleon defines the spin and parity of the nucleus. M. Goeppert-Mayer and J. H. D. Jensen were awarded the Nobel Prize in physics in 1963 for the discovery of the nuclear shell structure [61].
The independent-particle model was later enhanced mainly by two microscopic models: The nuclear shell model [62] and the Hartree-Fock-Bogoliubov (HFB) approach [63]. Both models are based on the concept that the interaction between a certain nucleon and all other constituents of the nucleus can be approximated by a mean-field, i. e. a single-particle potential. The selection of models is not considered to be complete, it rather focuses on the models relevant for this thesis. For a detailed discussion on mass models the reader is referred to [56].

The nuclear shell model takes nucleon-nucleon interactions into account by considering the interaction between valence nucleons and an inert core formed by all other nucleons. A disadvantage of this model is, that it is applicable only at or close to closed shells. Another possibility to extend the independent-particle model is the Hartree-Fock (HF) approach, which is an ab initio method. The HF method aims to find an exact solution for the Schrödinger equation $H\Psi = E\Psi$ by variationally optimizing the nuclear mean-field, which leads to the single-particle states. The Hamiltonian contains apart from the kinetic energy term a contribution due to the nucleon-nucleon interaction. The variational principle is the starting point of the HF method. In order to take pairing effects into account the HF model was extended to the HFB model. In the pure HF picture a nucleus with one nucleon outside a doubly-closed shell would be deformed. The results of the HFB method underestimate binding energies of $N = Z$-nuclides by about 2 MeV. In order to compensate for this effect, the so-called Wigner term was introduced, which scales with the difference between both nucleon numbers [56]. The HFB method is commonly used to predict masses over the whole nuclear chart, whereas the shell model can be used to determine the different single particle states and predicts spins. Collective effects can be either described by the shell model or the HF method.
Besides complete nuclear models, there are approaches that focus on specific properties, for example the atomic mass. Global mass formulas such as Myers-Swiatecki [64] or Duflo-Zuker [65] are very successful but will not be described here. For further information the reader is referred to [56]. In some cases masses of nuclides are required, which are unmeasured but lie close to a considerable number of nuclides with known masses. In these cases local mass formulas can be employed which extrapolate masses from nearby known masses [56]. One local mass formula was introduced by G. T. Garvey and I. Kelson [66]. It predicts the mass on a nucleus by taking the masses of neighboring nuclides into account. The Garvey-Kelson relations are based on the independent-particle model and receive a

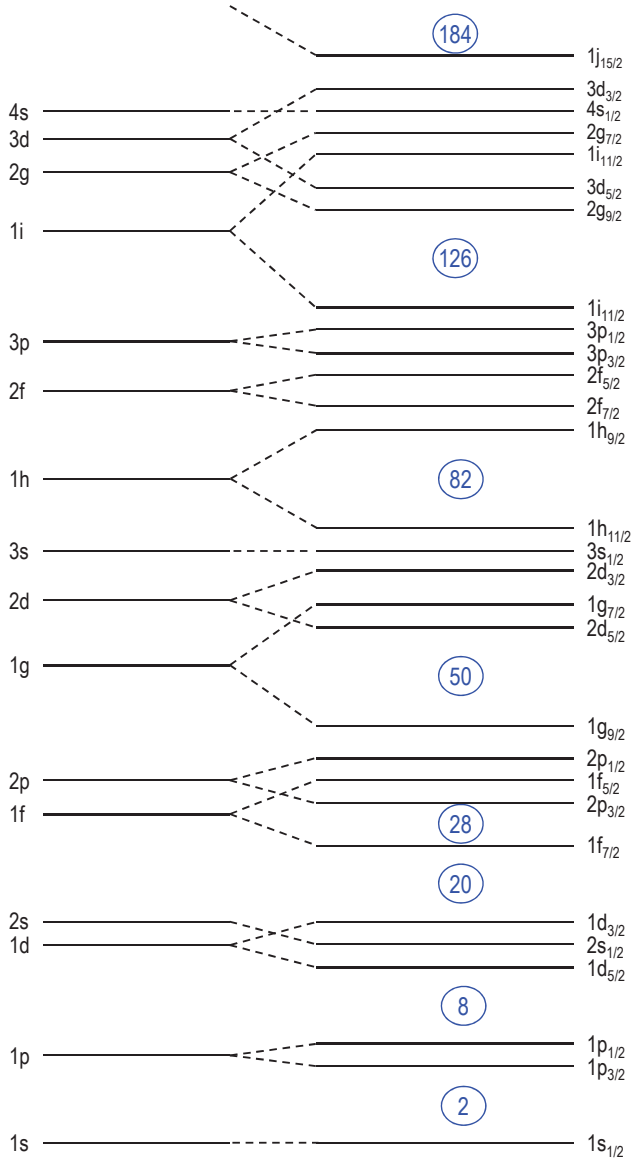

Figure 3.3: Energy levels of the nuclear shell model. Single particle potential levels (left) and the splitting due to the spin-orbit coupling (right). Magic numbers are indicated in circles. Adapted from [61].

high accuracy by using them iteratively. Another approach to predict masses by a local mass formula is the isobaric-multiplet mass equation (IMME) [67]. This equation relates masses of different members of an isospin multiplet by a quadratic relation. It is employed in mass regions up to $A \approx 100$.
Mass models can be used to study the different contributions to the interaction in a nucleus. In order to visualize these contributions, finite-difference mass formulas can be employed (see, e. g., Fig. 5.4), which will be subject of the following section.

3.2 Finite-Difference Mass Formulas for Nuclear Structure Studies

The binding energy of a nucleus can be used to study its structure. Since the total binding energy itself is a large quantity compared to the relative change, which occurs upon adding protons or neutrons to the nucleus, is not possible to reveal fine details of nuclear-structure information from it. Thus, it is difficult to study the evolution of the underlying nuclear structure. In order to gain a more detailed insight finite-difference mass formulas involving two or more nuclides are calculated, i. e. quantities, which are sensitive to specific effects are obtained. A few examples of finite-difference mass formulas, e. g. the two-neutron separation energy or the empirical pairing gap, are described in the following. As in the framework of this thesis mass measurements in the lead region have been performed, all examples shown in this section are based on the isotopic chain of lead.

Separation Energies

Differences of binding energies of two adjacent isotopes yield the separation energy of one neutron. The neutron separation energy decreases with increasing neutron number, which is a characteristic of the liquid drop model. In addition, this quantity exhibits the odd-even staggering, which is due to the enhanced binding energy of two paired neutrons. This is described by the pairing term $\delta(A, Z)$ in the Weizsäcker mass formula. The neutron separation energy

$$S_{\mathrm{n}}(Z, N) = B(Z, N) - B(Z, N-1) \tag{3.3}$$

exhibits a sharp drop at magic neutron numbers as shown in Fig. 3.4.
The neutron drip line is defined at $S_{\mathrm{n}}(Z, N_{\mathrm{drip}}) = 0$ meaning that nuclides with $N = N_{\mathrm{drip}}$ are not bound. Even though the shell concept is very successfully over a large range of the nuclear chart, shell quenching might occur far away from the valley of stability, i. e. when the neutron drip line is approached [56].
Considering the separation energy of two neutrons cancels out the odd-even effects. Thus, the two-neutron separation energy

$$S_{2\mathrm{n}}(Z, N) = B(Z, N) - B(Z, N-2) \tag{3.4}$$

shows a smooth decreasing trend for increasing neutron numbers. A sharp drop of several MeV indicates a shell closure, thus occurs at magic numbers, as shown in Fig. 3.5. Deviations from the general decreasing trend of $S_{2\mathrm{n}}$ give hints to local microscopic nuclear

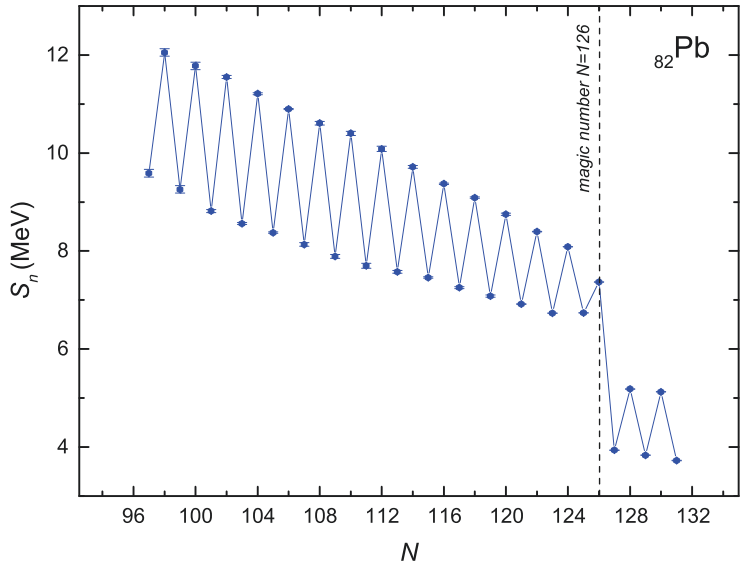

Figure 3.4: Experimental neutron separation energies for the Pb isotopic chain. A decrease in S_n is visible for increasing neutron numbers. In addition, an odd-even-staggering and a sudden drop at the magic neutron number 126 is characteristic for the neutron separation energy. Data and uncertainties were taken from AME2012 [58].

structure effects. A second typical deviation is a downward bump in $S_{2\mathrm{n}}$, which indicates a local deformation. This will be discussed in Chap. 5. For some isotopes, e. g. the thallium isotopic chain, a slight unexpected staggering is visible in $S_{2\mathrm{n}}$. The strength of this staggering will be discussed by means of the γ-parameter, which is introduced in Chap. 5.

Although the one- or two-neutron separation energies show structural effects it is required to consider even higher order finite-difference mass formulas, such as the empirical pairing gaps, to reveal effects in the range of hundreds of keV rather than effects on the MeV scale.

Empirical Pairing Gap

In 1932, W. Heisenberg described the stronger binding of even-number-particle nuclides compared to their odd-number-particle neighbors, which is visible in the odd-even staggering of binding energies [68, 69]. The attractive, short-range interaction in combination with the Pauli principle lead to pairs of nucleons of the same kind with spin $J = 0$. Adding a nucleon to, e. g. an even-even nucleus, the so-called empirical pairing gap to the next energy level has to be overcome. As a general trend, the empirical pairing gap decreases going from mid-shell towards the closed shell at $N = 126$, which is visible in Fig. 3.6. Due to the Coulomb force, the effective pairing force between two neutrons is larger than the pairing force between two protons. The pairing force drives nuclides to become spherical, which is in competition with the interaction between protons and neutrons leading to deformations.

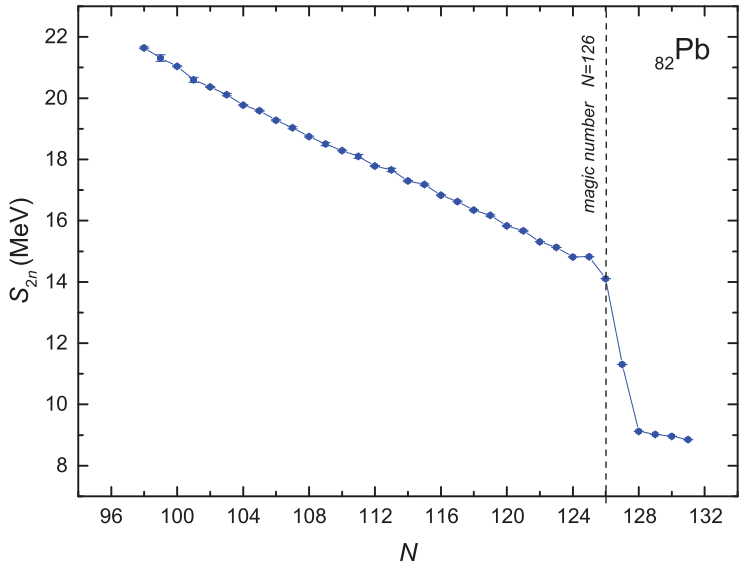

Figure 3.5: Experimental two-neutron separation energies for the Pb isotopic chain. A decreasing trend in $S_{2\mathrm{n}}$ for increasing neutron numbers is visible. At the magic number $N = 126$ a sudden drop occurs. Data and uncertainties were taken from AME2012 [58].

From a theoretical point of view the pairing gap contains more effects than pure pairing correlations [70]. It reflects all contributions leading to the odd-even staggering on the mass surface. Although there are further contributions, the name pairing gap remained, because the effect of breaking a pair of nucleons is the main contribution.
Apart from the downward trend for increasing neutron numbers, the empirical pairing gap of near-spherical nuclides show a parabolic shape between magic numbers (see for example Fig. 3 of Ref. [71]). Depending on the order, i. e. on the number of nuclides, which are taken into account, the empirical pairing gap is more or less sensitive to specific single contributions, such as deformation. The first order pairing gap mixes mean-field and pairing effects strongly [70], whereas the third and higher orders mainly represent the pairing effect and additionally e. g. deformation. Therefore, one employs higher order finite-difference mass formulas such as the so-called three-point indicator $\Delta^3_{\mathrm{n}}(Z,N)$ given as:

$$\Delta^3_{\mathrm{n}}(Z,N) = \frac{(-1)^N}{2}\Big(B(Z,N-1) + B(Z,N+1) - 2B(Z,N)\Big). \tag{3.5}$$

This is the empirical pairing gap, which is, in contrast to the pairing gap, experimentally accessible by calculating differences of binding energies. $\Delta^3_{\mathrm{n}}(Z,N)$ exhibits an odd-even staggering representing the stronger binding of even-N nuclides. Furthermore, a peak appears around magic numbers, see Fig. 3.6. According to [71] $\Delta^3_{\mathrm{n}}(Z,N)$ is the best parameter to describe pairing. Considering higher order finite-difference mass formulas the staggering smears out. The four-point indicator is not symmetric and will not be discussed here. A higher-order filter, which is commonly used, is the five-point indicator

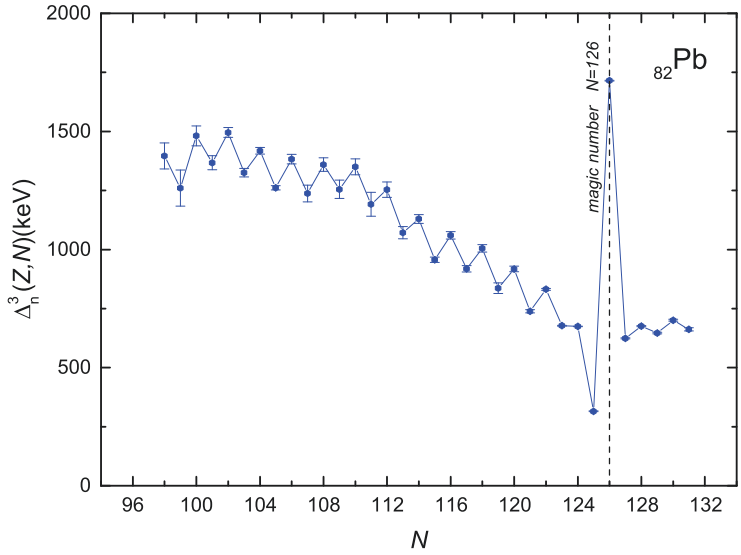

Figure 3.6: The empirical pairing gap $\Delta_n^3(Z,N)$ for the Pb isotopic chain shows a decreasing trend with an odd-even staggering on top of it. The effect of a closed shell at the magic number $N = 126$ is represented by a peak. Data and uncertainties were taken from AME2012 [58].

and can be expressed as:

$$\begin{aligned}\Delta_n^5(Z,N) = &\frac{(-1)^N}{8}\Big(B(Z,N+2) - 4B(Z,N+1) \\ &+ 6B(Z,N) - 4B(Z,N-1) + B(Z,N-2)\Big).\end{aligned} \tag{3.6}$$

In the $\Delta_n^5(Z,N)$ no staggering is visible anymore (see Fig. 3.7). The peak at $N = 126$ is still present but for higher order filters this peak gets broader as more than one adjacent binding energy is taken into account. According to [70] $\Delta_n^5(Z,N)$ yields the best decoupling from mean-field. M. Bender states that $\Delta_n^5(Z,N)$ gives a robust description of the odd-even staggering on the mass surface. However, as we will see in Chap. 5 the empirical pairing gaps are not a pure measure of pairing correlations. Polarization effects of valence nucleons interacting with the nucleons in closed shells lead to deformation, which is also affecting the trend of empirical pairing gaps.
Finite-difference mass formulas are ideal tools to study specific contributions of interactions, which influence the nuclear structure. However, the comparison of mass differences with complementary charge-radii information helps to understand the contribution of different effects to e. g. the empirical pairing gaps. Therefore, a brief introduction in nuclear charge radii is presented in the following. The combination of mass differences and mean-square nuclear charge radii information will be discussed in Chap. 5.

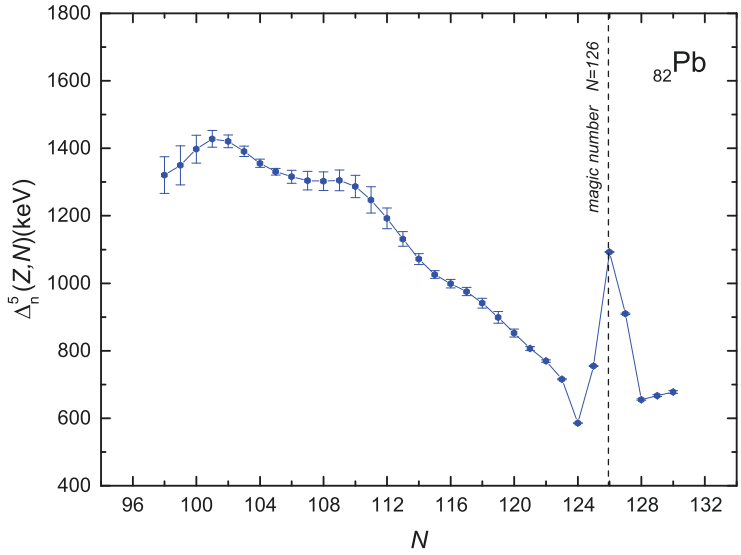

Figure 3.7: The empirical pairing gap $\Delta_n^5(Z,N)$ for Pb isotopes shows a smooth trend going down with a peak around the magic number $N = 126$. Data and uncertainties were taken from AME2012 [58].

3.3 The Nuclear Charge Radius

Differences in the mean-square nuclear charge radii can be determined by studies of the differences in an electronic transitions between two isotopes, i. e. the isotopic shift. In laser spectroscopy mean-square nuclear charge radii are determined along isotopic chains, which allows to see how the model-dependent size of a nucleus evolves upon adding neutrons [72]. The isotopic shift between two isotopes of mass A and A' is given by [73]

$$\delta\nu_{\mathrm{IS}}^{AA'} = \nu^{A'} - \nu^{A} \tag{3.7}$$

and contains two contributions

$$\delta\nu_{\mathrm{IS}}^{AA'} = \delta\nu_{\mathrm{MS}}^{AA'} + \delta\nu_{\mathrm{FS}}^{AA'}, \tag{3.8}$$

whereas $\delta\nu_{\mathrm{MS}}$ and $\delta\nu_{\mathrm{FS}}$ represent the mass shift and the field shift, respectively. The field shift $\delta\nu_{\mathrm{FS}}$ scales with the differential charge radius $\delta\langle r^2\rangle^{AA'}$ between the two nuclides under investigation. It can be expressed as

$$\delta\nu_{\mathrm{FS}} = \frac{2\pi Z e^2}{3}\Delta|\Psi(0)|^2 \cdot \delta\langle r^2\rangle^{AA'}, \tag{3.9}$$

whereas e is the charge of the electron, Z the proton number and $\Delta|\Psi(0)|^2$ describes the electron density at the nucleus. As the mass shift $\delta\nu_{\mathrm{MS}}^{AA'}$ can be calculated, the differential charge radius can be extracted from the measurement of the isotopic shift. In order to obtain the absolute radius, the radius of at least one isotope has to be known. This radius can be extracted, e. g., from elastic electron scattering. For the comparison to

mass differences (see Chap. 5), the differential mean-square nuclear charge radius can be used as the trend shows the same behavior as the absolute radius.

Part II

Experimental Setup and Results

Chapter 4

ISOLDE and the Penning-Trap Experiment ISOLTRAP

High-precision mass measurements carried out in the context of the present thesis were performed at the double Penning-trap experiment ISOLTRAP (Isotope Separator On-Line TRAP) [33, 34]. This mass spectrometer is dedicated to mass measurements of exotic, short-lived nuclides and located at the ISOLDE (Isotope Separator On-Line DEvice) facility at the European Organization for Nuclear Research CERN (Geneva, Switzerland). In total, more than 400 masses with half-lives as short as 48 ms [74] have been investigated at ISOLTRAP with a relative mass uncertainty reaching $\delta m/m = 8 \cdot 10^{-9}$ [29]. In the following, details of the ISOLTRAP experiment and the ISOLDE facility are presented.

4.1 The ISOLDE Facility

The ISOLDE facility [35] is an isotope on-line mass separator at CERN, which is devoted to the production of short-lived nuclides to investigate different fields of physics such as nuclear and atomic physics, astrophysics, solid state physics, or applications in life science. A schematic of the experimental hall is shown in Fig. 4.1. The radionuclides are created in processes like spallation, fragmentation or fission. The nuclear reactions are induced by 1 or 1.4-GeV protons impinging on a thick target, e. g. UC_x or ThC_x. The Proton Synchrotron Booster accelerates the protons in bunches of up to 2.1 µA intensity, i. e. up to $3.2 \cdot 10^{13}$ protons per pulse every 1.2 s. One half of the pulses is directed to the ISOLDE targets. The reaction products defuse out of the target and are ionized either by surface ionization, resonant laser ionization (RILIS) or plasma ionization [75]. Using different techniques allows one to deliver a large variety of nuclides from $Z = 2$ to 88 with half-lives down to ms range. Figure 4.2 shows the chemical elements, which are available as radioactive beams at ISOLDE. The isotopes are accelerated to 30–60 keV and are separated by one of the two magnetic mass filters, the General Purpose Separator (GPS, resolution $m/\Delta m \approx 1000$) or the High Resolution Separator (HRS, resolution $m/\Delta m \approx 5000$). The radioactive ion beam is then transported via a beamline using electrostatic ion optical elements to different experiments situated at ISOLDE. The central beamline guides the

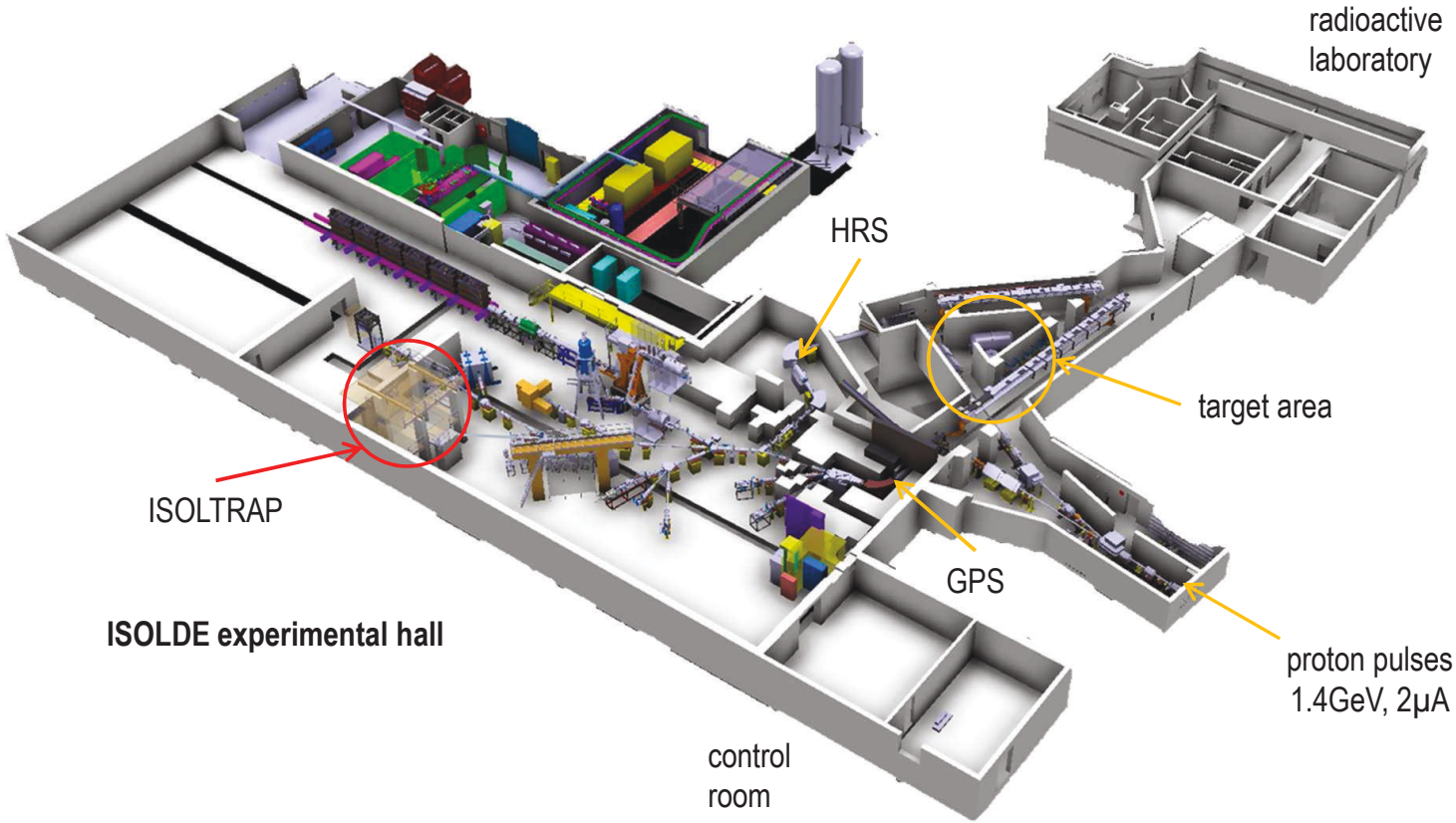

Figure 4.1: Experimental hall of the ISOLDE facility [35]. On the right the protons coming from the PSB enter the hall and impinge on a thick target, typically UC_x or ThC_x, to create radioactive nuclides in one of the target stations, HRS or GPS. After extraction and ionization the radionuclides are mass separated by one of the mass filters and pass ion optics before they enter the ISOLTRAP setup being placed at the end of the central beamline.

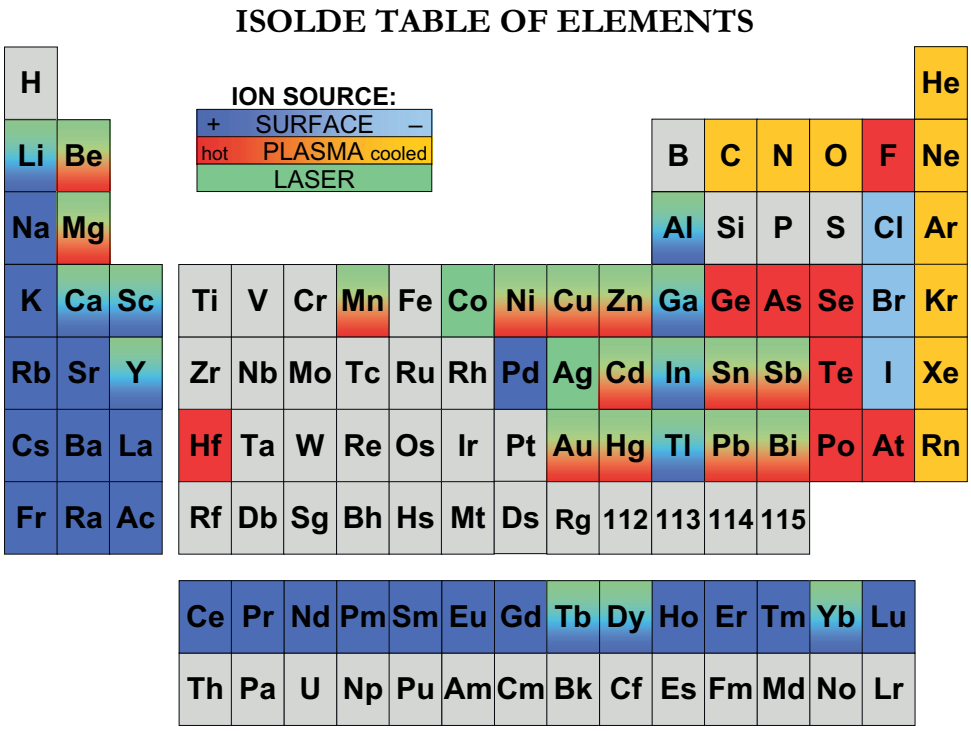

Figure 4.2: Periodic table of elements which are available as radioactive beams at ISOLDE. The colors indicate the corresponding ion source. (Courtesy of Luis Fraile)

ions to the ISOLTRAP experiment.

4.2 The Experimental Setup of ISOLTRAP

The main components of the ISOLTRAP mass spectrometer are shown in Fig. 4.3. The 30–60-keV ion beam coming from ISOLDE is first stopped, cooled and bunched in a gas-filled linear radiofrequency quadrupole ion trap (RFQ cooler and buncher) (2) [54] operated at high voltage. Afterwards ions are delivered to the MR-ToF (Multi-Reflection Time-of-Flight) (3) [76] mass separator and then transferred to the tandem Penning-trap system consisting of the preparation (5) and the precision Penning trap (6). In the preparation trap a mass selective buffer-gas cooling and centering technique is applied [77] so that an isobarically pure ion bunch can be injected into the precision trap, which is dedicated to high-precision mass measurements using the time-of-flight ion-cyclotron resonance detection technique. Apart from high-precision mass measurements, decay-spectroscopy studies can be performed employing the tape station setup (7).

4.2.1 Ion Production and Beam Preparation

ISOLTRAP is equipped with two ion sources for systematic studies and reference measurements, which are carried out for magnetic field calibration measurements during online

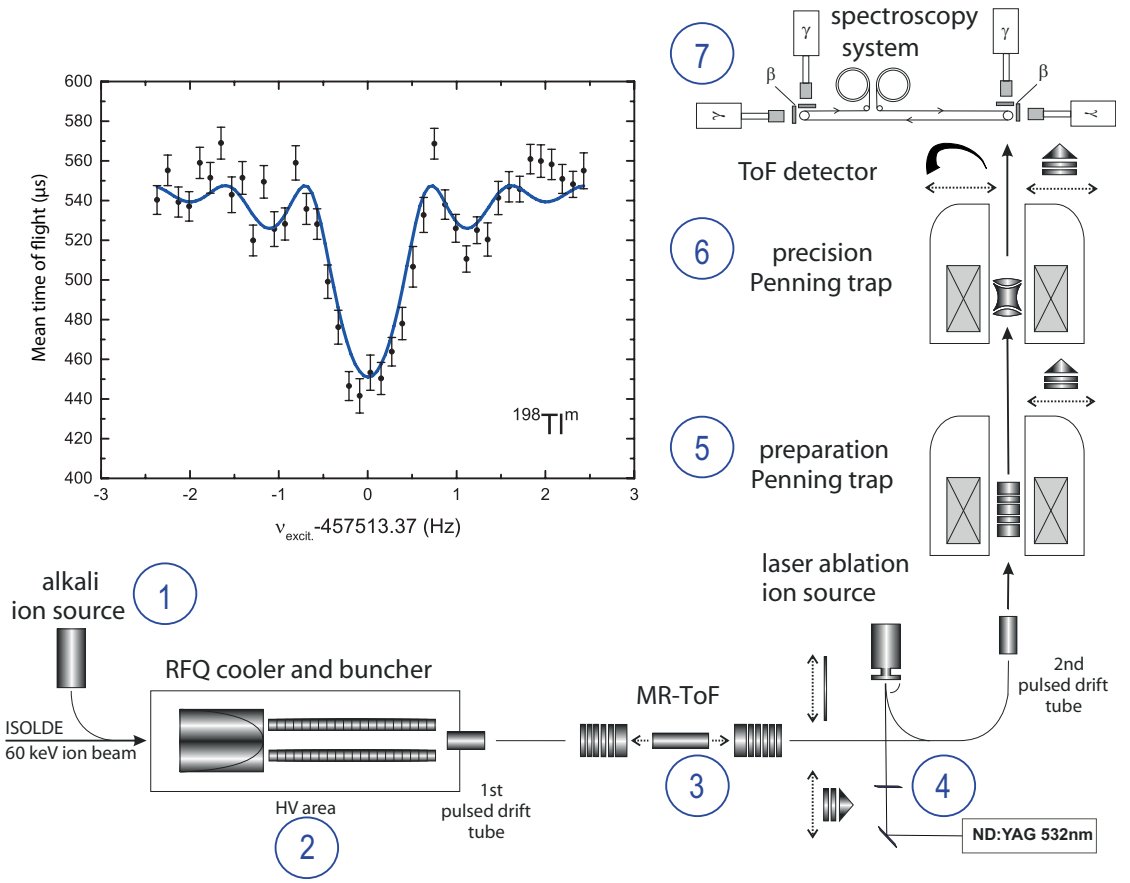

Figure 4.3: Sketch of the experimental setup: The ions coming from ISOLDE or the offline alkali ion source (1) are accumulated in the RFQ cooler and buncher (2). Then the ion bunches pass the first pulsed drift tube and the MR-ToF mass separator (3). Alternatively ions are produced by the offline laser ablation ion source (4) and enter the beamline behind the MR-ToF. Then the ions are guided to the vertical part of the beamline and injected into the preparation Penning trap (5). After isobaric purification they are injected into the precision Penning trap (6). Finally the ions are transferred either to a channeltron, an MCP detector or a spectroscopy system (7). The inset shows a $^{198}Tl^{m}$ ion-cyclotron resonance with an excitation time of 1.2 s.

experiments: A surface-ionization ion source for a production of singly charged ions of alkali and alkaline-earth elements and a laser ablation ion source capable of the production of singly charged ions of any solid element, e.g., carbon.
The surface-ionization ion source is placed in front of the RFQ cooler and buncher section as shown in Fig. 4.3 (1); the laser ablation ion source is mounted behind the MR-ToF section, see Fig. 4.3 (4). The RFQ cooler and buncher and MR-ToF section (see Fig. 4.3 (2) and (3), respectively), are used for accumulating, cooling, bunching ,and cleaning the ion beam. The RFQ cooler and buncher is filled with helium gas. Here, the ions are thermalized, focused onto the axis and accumulated in an electrostatic potential well at the end of the RFQ cooler and buncher. After a certain time the potentials of the end electrodes of the buncher are lowered to release the ions as an ion bunch. Behind the buncher a pulsed drift tube adjusts the ion bunch energy to about 3 keV. The ion bunch is injected in the MR-ToF [76], which was installed in 2010. It can be used either for purification of contaminated ion beams from ISOLDE or operated as a mass spectrometer. Behind the MR-ToF the ions are guided towards the vertical beamline where the energy of the ions is lowered to few hundreds of eV by means of a pulsed drift tube before they enter the Penning-trap system.

4.2.2 The Tandem Penning-Trap System

The ISOLTRAP Penning-trap mass spectrometer consists of two traps: the preparation trap and the precision trap. This is a standard trap configuration used in most online Penning-trap facilities. The preparation trap serves as a high-resolution mass separator via employment the of buffer-gas cooling technique. High-precision mass measurements are carried out in the precision trap employing the ToF-ICR method.

The Preparation Penning Trap

The preparation trap is a cylindrical Penning trap [78], which consists of an eight-fold segmented ring electrode, four-fold segmented endcaps and four-fold segmented correction electrodes, see Fig. 4.4. The large inner radius of r_i=17.5 mm facilitates to accept wide incoming ion bunches and the storage of more than 10^4 ions. The preparation Penning trap is situated in the homogenous magnetic field of a superconducting magnet with $B = 4.7\,\mathrm{T}$. In order to cool the axial and radial ion motions by buffer-gas collisions the trap is filled with helium gas at a pressure of about 10^{-4} mbar. The mass resolving power achievable with mass-selective buffer-gas cooling amounts to 10^5, thus providing isobaric purification. In addition the emittance of the ions can be improved dramatically to ensure optimal and reproducible starting conditions for the injection in the precision trap. For optimization purposes cooling resonances (see Fig. 4.5) are recorded employing an MCP detector located behind the preparation trap. Cooling resonances are obtained by measuring the ion count rate for different quadrupolar excitation frequencies, which are varied around the cyclotron frequency of the ion of interest.

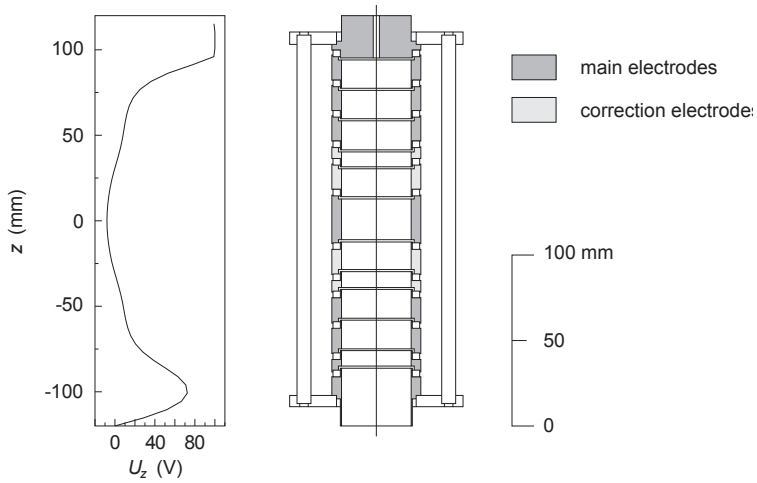

Figure 4.4: Sketch of the cylindrical preparation Penning trap [79] for isobaric separation consisting of main electrodes (gray) and correction electrodes (light gray). Applying appropriate voltages to the trap electrodes yields the shape of the trapping potential shown on the left. Taken from [2].

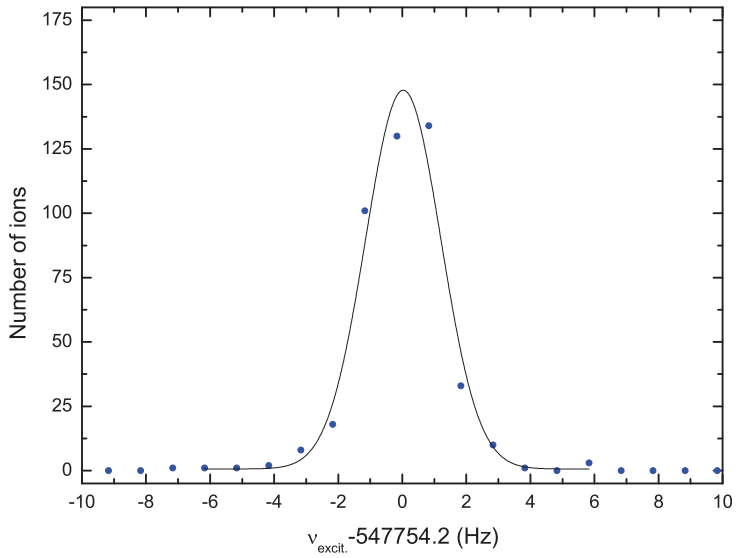

Figure 4.5: Cooling resonance of $^{133}Cs^{+}$ recorded using the MCP between the preparation trap and the precision trap. A resolving power of $2 \cdot 10^5$ has been achieved.

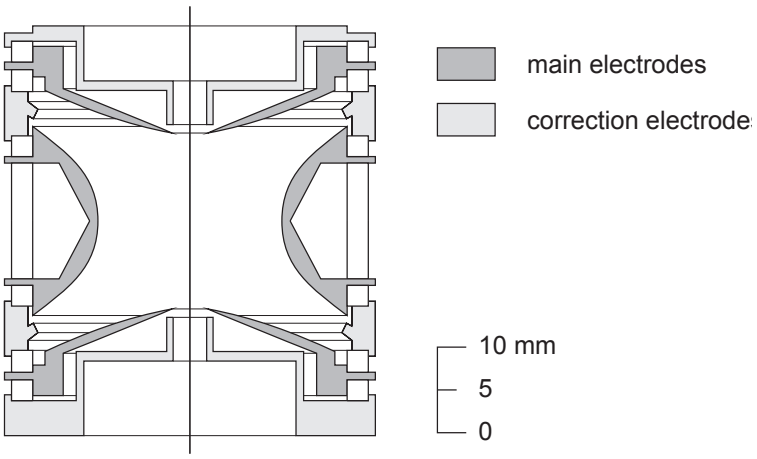

Figure 4.6: Sketch of the hyperboloidal precision Penning trap for isomeric separation containing main electrodes (gray) and correction electrodes (light gray). Taken from [2].

The Precision Penning Trap

The hyperbolic precision trap consists of a four-fold segmented ring electrode, endcaps and additional correction electrodes (Fig. 4.6) and is installed in the center of a superconducting magnet with $B = 5.9\,\mathrm{T}$. It is placed in high vacuum of about 10^{-9} mbar to allow for long excitation times up to several seconds. The ion bunches, which are ejected from the preparation trap with a low energy spread, are captured in flight in the precision trap, where their mass is determined employing the ToF-ICR technique. A time-of-flight ion-cyclotron resonance of ^{133}Cs is shown in Fig. 4.7. Alternatively the ion bunches are guided to the decay-spectroscopy setup.

4.2.3 Ion Detection for Mass Measurements

The ion detection at ISOLTRAP is realized by the time-of-flight detection technique, which has been described in Chap. 2.2.3. It is a suitable technique for ISOLTRAP as the half-life of exotic nuclides produced by ISOLDE often limits the measurement time. After the ions are captured and trapped in the precision trap, a dipolar excitation at the magnetron frequency of several hundred ms leads to a defined magnetron radius of about 0.7 mm. The recentering of the ions of interest is achieved by applying a quadrupolar frequency at $\omega_{\mathrm{rf}} = \omega_+ + \omega_-$. The choice of the quadrupolar excitation time depends on the one hand on the vacuum conditions, and on the other hand on the half-life of the trapped ion. Long excitation times of several seconds yield a high precision in determining the frequency, but in cases where damping effects play a role, the sidebands of the resonance vanish and a compromise has to be found. Depending on the excitation time and the excitation amplitude, a full conversion from the magnetron into the cyclotron motion is achieved. The recentered ions are then ejected out of the precision trap and about 1.2 m downstream an microchannel plate (MCP) detector is located for the ion detection. The value of the magnetic field strength at the detector position is reduced by three orders

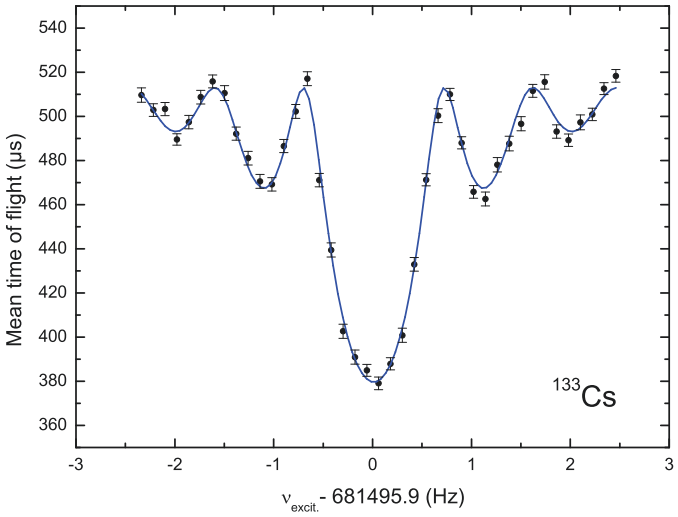

Figure 4.7: Time-of-flight ion-cyclotron resonance of ^{133}Cs with an excitation time of 1200 ms. The theoretical line shape (blue solid line) was fitted to the data [52].

of magnitudes compared to the trap center, i. e. ions are passing a region with a high longitudinal magnetic-field gradient yielding an enhanced time-of-flight effect.

4.2.4 The Decay-Spectroscopy Setup

Radioactive ion beams produced at ISOLDE very often suffer from strong isobaric or isomeric contamination. The high-resolving power offered by Penning traps for removing isobaric and isomeric contaminations from the ions of interest can be exploited for decay-spectroscopy studies [80]. A purified sample can be provided for decay studies using the compact spectroscopy setup coupled to the ISOLTRAP experiment (see Fig. 4.3 (7)). In order to reach the decay-spectroscopy setup with sufficient energy, ions are ejected from the precision Penning trap and reaccelerated to several keV before implantation in a movable tape. Thus, the decay daughters can be moved using a tape-transport system. The decay-spectroscopy setup holds a compact beta- and gamma detection system. The use of several detectors allows one to generate coincidence spectra, which means that the background is significantly decreased. At present, the system can be used in two different configurations. It can be used to perform decay-spectroscopy studies to assist mass measurements enabling for example spin-state assignments or it is also possible to perform trap-assisted decay spectroscopy.
For the measurements discussed within this thesis, the decay-spectroscopy setup was used for spin-state assignment reducing the mass uncertainty tremendously. This feature is especially important for nuclides, which exhibit low-lying long-lived isomers, where the determined mass cannot be assigned with confidence to the ground state or the isomeric state.

Chapter 5

ISOLTRAP Mass Data

This chapter describes the results of high-precision mass measurements performed in the context of the present thesis at the ISOLTRAP experiment. A total of seven nuclides in the thallium region have been addressed: ^{194}Au, ^{194}Hg, ^{190,193,198}Tl and ^{202,208}Pb. This chapter starts with a brief introduction of principles of mass determination followed by the description of the analysis of the aquired data. Each nuclide is considered individually. The chapter is culminated by the discussion of the impact of the obtained results on the nuclear structure of the thallium isotopic chain.

5.1 Principle of the Mass Determination

The determination of mass values is based on cyclotron frequency measurements. Due to the fact that the cyclotron frequency introduced in Eq. (2.5) depends not only on the mass of the ion m_{ion} and the charge state q, but also on the magnetic field B, frequency ratios $r = \frac{\nu_{\mathrm{ref}}}{\nu}$ are measured in order to cancel the magnetic field. Thus, the primary result of the measurements are frequency ratios, from which the ionic mass can be derived according to

$$m_{\mathrm{ion}} = \frac{\nu_{\mathrm{ref}}}{\nu} \cdot m_{\mathrm{ion,ref}} \cdot \frac{q}{q_{\mathrm{ref}}}. \tag{5.1}$$

Since only singly charged ions were measured, the charge states q and q_{ref} cancel out. Thus, atomic masses can be expressed via ionic masses and the electron mass m_{e} according to

$$m = r \cdot (m_{\mathrm{ref}} - m_e) + m_e. \tag{5.2}$$

The binding energy of the electron is neglected since it is small compared to the uncertainty of the mass determination. The frequencies of the reference ions and the ions of interest were measured alternately. In order to determine the ratio of two frequencies at a given time, the frequencies of the reference ion measured before and after the frequency of the ion of interest were interpolated to the measurement time of the ion of interest. For the presented measurements, $^{133}Cs^{+}$ was used as reference ion. Since the frequency ratio is equal to the mass ratio, the ion mass can be recalculated, whenever the mass of the reference ion is measured with higher precision.

5.1.1 Contributions to the Uncertainty

In the following, different contributions to the uncertainty of the frequency ratio will be discussed. Apart from the statistical uncertainty, the influence of magnetic field fluctuations and effects due to isobaric or isomeric contaminations, one has to account for systematic effects at ISOLTRAP.
The total uncertainty of the frequency ratio is given as

$$\sigma_{\mathrm{tot}} = \sqrt{\sigma_{\mathrm{stat}}^2 + \sigma_{\mathrm{mass}}^2 + \sigma_{\mathrm{res}}^2} \tag{5.3}$$

with σ_{mass} and σ_{res} being the mass-dependent and residual systematic uncertainty, respectively, whereas σ_{stat} represents the total statistical uncertainty of the frequency ratio. A detailed description can be found in [29].

Statistical Uncertainty

As a first step of the analysis of the ToF-ICR spectra the theoretical line shape [52] is fitted to the data using the analysis program *EVA* [81]. The fit yields a frequency value with its statistical uncertainty. The presence of more than one ion in the precision trap during the measurement may result in an ion number dependent frequency shift, e.g., in Ref. [51,52]. These shifts are taken into account by applying a so-called count-rate analysis [29]. Each ToF-ICR spectrum contains events with different numbers of detected ions in the Penning trap. These events are grouped in count-rate classes with respect to the number of ions in the group. Then frequencies can be obtained for each count-rate class ordered by the number of ions. Fitting a straight line through these frequencies allows an extrapolation to events where only one ion is in the trap. Taking this effect into account leads to an increased uncertainty of the cyclotron frequency ratio.
Considering not only the statistical uncertainty of a frequency, but the statistical uncertainty of a frequency ratio one more effect has to be considered: the magnetic flux creep and magnetic field fluctuations [49, 50]. The ratios of the frequency of the ion of interest and the reference ion frequency, which is the result of the interpolation of the reference measurement to the time when the actual measurement of the ion of interest was performed, are affected by the magnetic field fluctuations. Interpolating the reference frequency the magnetic field fluctuations are taken into account by adding

$$u_B = 6.35 \cdot 10^{-11}/min \cdot \Delta T \tag{5.4}$$

quadratically to the statistical uncertainty [29], where ΔT denotes the time that has elapsed between two reference measurements. Thus we obtain σ_{stat}, containing the statistical uncertainty of the frequency as well as the statistical uncertainty of the frequency ratios. To keep σ_{stat} small one has to find a compromise between short measurement times and thus a small influence of magnetic field fluctuations and long measurement times yielding better statistics. For each mass determination several frequency ratios are measured. A weighted mean value of all frequency ratios is determined and the final statistical uncertainty of the mean frequency ratio contains also the scattering of these single ratios.

Mass-dependent Uncertainty

In addition, one takes into account the fact that the reference mass might be several mass units away from the mass of the ion of interest. This leads to an additional uncertainty proportional to the mass difference:

$$u_m = 1.6 \cdot 10^{-10}/\mathrm{u} \cdot (m - m_{\mathrm{ref}}), \tag{5.5}$$

which is the result of a systematic study using carbon cluster ions of different sizes. This mass-dependent uncertainty occurs due to electric and magnetic field imperfections in the Penning trap. Details are discussed in [29].

Residual Uncertainty

Furthermore one has to consider a residual systematic effect of

$$u_{\mathrm{res}} = 8 \cdot 10^{-9}. \tag{5.6}$$

This value was determined in a study described in Ref. [29], where this was determined as the limit in the systematic accuracy. Measureing a local network of many frequency ratios [33] may yield a reduction of this limit.

5.1.2 The Atomic Mass Evaluation

Many atomic masses have been measured at various experiments employing different measurement methods. In order to find one mass value for each isotope, the Atomic Mass Evaluation (AME) was developed, which generates the atomic mass as the combination of all these experimental results, [58, 82]. The so generated mass table serves as a general mass reference. Since the uncertainty of different methods sometimes differ by orders of magnitudes, an averaged uncertainty weighted value is published there. Due to the fact that ISOLTRAP data are published as frequency ratios of the ion of interest and a reference ion, it is easy to renew a mass value in the case that the reference ion is measured later on with a higher precision. Typically, the AME masses are listed in terms of mass-excess values

$$ME = m - A \cdot \mathrm{u}, \tag{5.7}$$

with A being the atomic mass number, m the atomic mass and u the atomic mass unit. For cases where a mixture of ground state and isomeric states is measured, a correction procedure according to App. B in Ref. [58] has to be applied. Subtracting half of the excitation energy from the measured value yields the ground-state mass excess $ME_{g.s.}$:

$$ME_{\mathrm{g.s.}} = ME_{\mathrm{exp}} - \frac{1}{2}E_{\mathrm{excit.}} \tag{5.8}$$

with ME_{exp} being experimental mass excess and $E_{excit.}$ the excitation energy of the isomer. The uncertainty of the ground-state mass excess can be obtained by

$$\sigma_{\mathrm{g.s.}} = \sqrt{\sigma_{\mathrm{exp}} + \left(\frac{1}{2}\sigma_{\mathrm{excit.}}\right)^2 + \frac{1}{12}E^2_{\mathrm{excit.}}}, \tag{5.9}$$

Table 5.1: Overview of settings for different experimental campaigns at ISOLTRAP. For each run the ion energy of the ISOLDE beam, ion source and separator are indicated. For all runs, an UC_x target was used.

Isotope	Z	Run	Date	Ion energy	Ion source	Separator
^{194}Au	79	A	July 2008	30 keV	RILIS	GPS
^{194}Hg	80	B	Aug. 2008	30 keV	Hot plasma	GPS
^{190,193}Tl	81	C	Apr. 2009	30 keV	Hot plasma	HRS
^{198}Tl	81	D	Oct. 2012	50 keV	Surface (Ta cavity)	HRS
^{202}Pb	82	E	May 2008	50 keV	Hot plasma	GPS
^{202,208}Pb	82	F	Oct. 2008	30 keV	Plasma with quartz	HRS

whereas $\sigma_{\text{excit.}}$ represents the uncertainty of the excitation energy. The term $\frac{1}{12}E^2_{\text{excit.}}$ is added to account for the fact that the ratio between the ions being in the ground and isomeric state is not known. If a pure sample of the isomeric state was measured, the total excitation energy is subtracted and thus the ground state can be deduced from such a measurement.

5.2 Results

In total, the masses of seven nuclides, namely ^{194}Au, ^{194}Hg, ^{190,193,198}Tl and ^{202,208}Pb, were determined in six experimental campaigns. Details like mass separators, ion energies and ion sources used in the individual experimental campaigns are listed in Tab. 5.1. Table 5.2 shows the results including frequency ratios and mass-excess values. Most of the results are implemented in the recent AME2012 [58] and therefore the data are compared to the previously known literature value taken from AME2003 [82]. A comparison between literature and the new results is depicted in Fig. 5.1.
Apart from the measurement of ^{194}Au, where ^{197}Au served as a reference mass, $^{133}Cs^+$ ions from the surface-ionization ion source at ISOLTRAP were used for the reference measurements. For most of the resonances, a count-rate analysis was applied. For cases in which the number of recorded ions was too low to perform the count-rate analysis, the error bar was increased by an equivalent factor. In the following each nuclide is discussed separately and details about the measurements are described.

Gold $Z = 79$

In the experimental campaign A (see Tab. 5.1) the mass of ^{194}Au was determined by taking six ToF-ICR spectra. The stable isotope ^{197}Au, also produced by ISOLDE, served as a reference ion. This is advantageous since the mass-dependent uncertainty (see Eq. (5.5)) is thus very small. The mass-excess value of $-32213(2)$ keV [84] has been obtained and was implemented in AME2012 with a significance of 100 %. The reduction of the error bar by a factor of 5 was possible by applying long excitation times of 10 s leading to high precision. The statistics were high enough to allow for count-rate analysis. The new value does not confirm the previous one, which was the result of beta decay studies,

Table 5.2: Measured isotopes, half-lives, frequency ratios, ISOLTRAP mass-excess data, literature values [82] and the influence of new results on AME2012 are listed. Ground states marked with * were obtained by subtracting the excitation energy from the excited state value, measured within the present work. Note that the data of ^{190,193}Tl present the combination of values obtained within this thesis and values analyzed within the framework of [83]. Data from AME2003 marked with # indicate estimated values.

Isotope	Half-life $T_{1/2}$	$r = \frac{\nu_{c,ref}}{\nu_c}$	ISOLTRAP ME (keV)	AME2003 ME (keV)	Weight %
$^{194}Au_{115}$	38.02(0.10) h	0.9847631028(110)	−32213(2)	−32262(10)	100
$^{194}Hg_{114}$	440(80) y	1.495426184(230)	−32184(3)	−32193(13)	100
$^{190}Tl^{g.s.}_{109}$*	2.6(3) m		−24379.3(50)	−24330#(50#)	
$^{190}Tl^{m}_{109}$	3.7(3) m	1.4293932800(520)	−24289.3(6.4)	−24200#(70#)	100
$^{193}Tl^{g.s.}_{112}$*	21.6(0.8) m		−27477(7)	−27320(110)	100
$^{193}Tl^{m}_{112}$	2.11(15) m	1.4519430724(423)	−27104.3(5.2)	−26950(110)	100
$^{198}Tl^{g.s.}_{117}$*			−27528.7(7.5)	−27490(80)	-
$^{198}Tl^{m}_{117}$	1.87(0.03) h	1.4895649197(606)	−26985.1(7.5)	−26950(80)	-
$^{202}Pb_{120}$	52.5(2.8) ky	1.5196700577(328)	−25941.4(4.1)	−25934(8)	84
$^{208}Pb_{126}$	stable	1.5648489806(415)	−21749.4(5.1)	−21748.5(1.2)	0

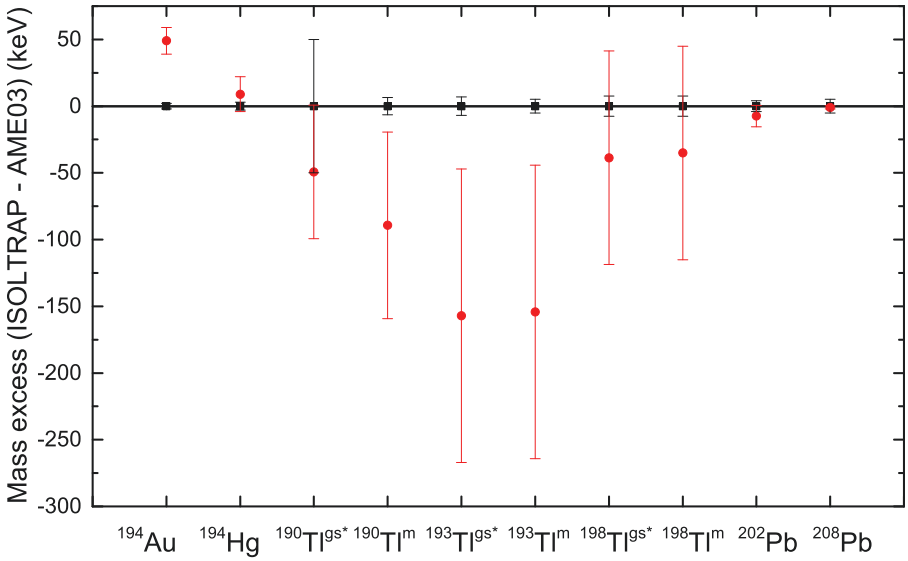

Figure 5.1: Differences of mass-excess values obtained at ISOLTRAP (black) and literature data taken from AME2003 [39] (red). Ground states marked with * are obtained by subtracting the excitation energy from the measured isomeric state. Apart from ^{208}Pb the uncertainties could be reduced for all nuclides.

which are not as reliable as direct Penning-trap mass measurements. Furthermore, the mass of ^{197}Au, which served as reference for the ^{194}Au measurement, was determined at TRIGA-TRAP [85] and no deviation to the literature value in AME2003 was found.

Mercury $Z = 80$

In the experimental campaign B the mass of ^{194}Hg was determined. In total 4 resonances were recorded. Due to long excitation times of up to 10 s the mass uncertainty could be reduced by a factor of 4. The mass-excess value of $-32184(3)$ keV has been obtained, being implemented in AME2012 with a significance of 100 %. The count-rate analysis was performed.

Thallium $Z = 81$

Thallium mass measurements were performed for three isotopes: ^{190}Tl^m, ^{193}Tl^m and ^{198}Tl^m. For all of them the first isomeric state was measured. This is not suprisingly since it was seen before, that the production rate of the high-spin state of Tl is favored [86]. In case of ^{190}Tl^m and ^{193}Tl^m the spin state could be identified thanks to an experimental campaign in 2011 [86]. Accordingly, the masses could be assigned to the first isomeric state. In the experimental campaign C for ^{190}Tl^m and ^{193}Tl^m in total 9 and 4 resonances were recorded, respectively. An example of a spectrum of ^{193}Tl^m is shown in Fig. 5.2. For ^{190}Tl^m the excitation time varied between 300 ms and 4 s. The mass excess for ^{190}Tl^m was determined to be $-24289.3(6.4)$ keV. In case of ^{193}Tl^m the excitation time was chosen between 100 ms and 2.5 s and a mass-excess value of $-27104.3(5.2)$ keV was obtained. Note that both values, i. e. the results of ^{190}Tl^m and ^{193}Tl^m, were combined with later measurements at ISOLTRAP [83]. These values are included in AME2012 with a significance of 100 %.

The first isomeric state of ^{198}Tl was measured within the experimental campaign D. In total 3 ToF-ICR spectra were recorded with an excitation time of 1200 ms. A count-rate analysis was possible due to high count rates. The obtained mass excess of $-26985.1(7.5)$ keV agrees within $1\,\sigma$ with the value included in the AME2003. The previous value was determined by beta-decay studies with a tenfold larger uncertainty.

Lead $Z = 82$

Within two experimental campaigns, labeled E and F, the mass-excess values of ^{202}Pb and ^{208}Pb were determined to be $-25941.4(4.1)$ keV and $-21749.4(5.1)$ keV, respectively. Both results agree well within the error bars with the AME2003 values. For ^{202}Pb 10 resonances were taken with excitation times of up to 10 s and for ^{208}Pb 4 resonances were recorded with 1200 ms excitation time. In the case of ^{202}Pb the error bar could be reduced by a factor of 2 and the influence on the value published in AME2012 is 84 %. The high influence on the result published in AME2012 is due to the fact that one of the

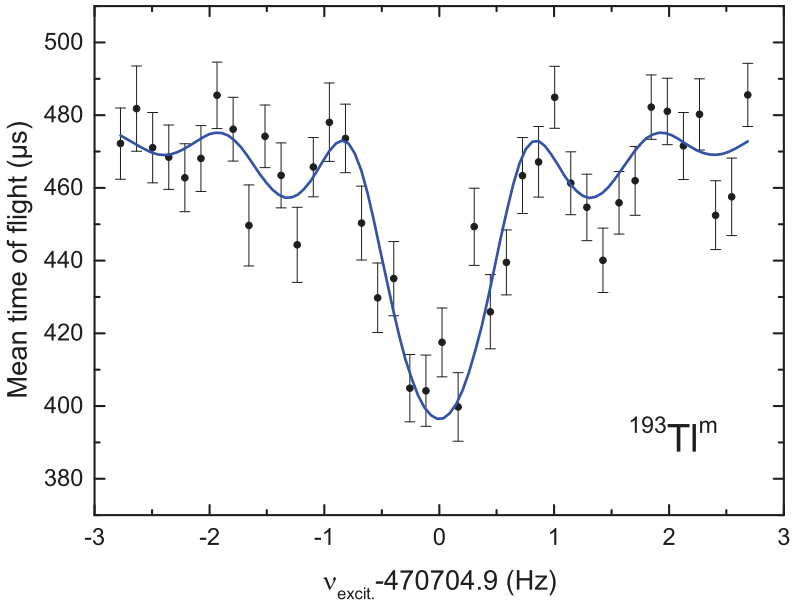

Figure 5.2: Time-of-flight ion-cyclotron resonance curve of $^{193}\mathrm{Tl}^{m}$ with an excitation time of 1 s. About 1250 ions were recorded to obtain this spectrum. The data (black circles) are fitted by the theoretical lineshape (blue line) [52].

masses contributing to the previous literature value, published in AME2003, is not taken into account anymore. The measurement of ^{208}Pb serves as a consistency check of the ISOLTRAP mass spectrometer.

5.3 Discussion[1]

The thallium region is of high interest due to low-lying isomeric states and deformed nuclides where effects like shape coexistence or shape staggering can be observed. In the present chapter nuclear structure of nuclides in the thallium region will be discussed. The evolution of the nuclear structure of Tl isotopes is studied by employing finite-difference mass formulas to the ground state masses of thallium and its neighbors lead, mercury and gold. On the one hand Tl ($Z = 81$) is only one proton missing to the magic and spherical Pb ($Z = 82$) isotopes. On the other hand it is close to the Hg ($Z = 80$) and Au ($Z = 79$) isotopes, which exhibit shape staggering and deformation, respectively. Therefore it is interesting to study how this change in structure evolves along an isotopic chain when protons are added from $Z = 79$ to $Z = 82$. Moreover, the excitation energy of low-lying isomers in the thallium region will be discussed.

[1] Parts of this chapter are taken from the author's paper [1].

Nuclear Structure Studies of Neutron-Deficient Thallium Isotopes

There are two different approaches for the discussion of deformation, which will be described in this chapter. One of them is based on the comparison of the empirical pairing gap with mean-square nuclear charge radii (a) and the another possibility is to link the slope of the empirical pairing gap to the strength of staggering in the two-neutron separation energy (b). Thus, for the second approach only mass data are used.

Approach (a)
As discussed already in Chap. 2 the binding energy itself is not suitable to reveal nuclear struture information. To get a detailed insight in the structure of a nucleus, finite-difference mass formulas, such as the empirical pairing gap $\Delta^3_{\mathrm{n}}(Z,N)$ (see Eq. 3.5), are employed. The three-point indicator of near-spherical nuclides has an overall downsloping trend with increasing neutron number N. In addition, for spherical systems it exhibits a parabolic shape between magic numbers (see for example Fig. 3 of [71]) with a downsloping trend towards closed shells. Furthermore an odd-even staggering is present along the isotopic chains as shown in Fig. 5.3. Here, experimental data of Pb (blue upward triangles), Tl (red circles) and Hg (green downward triangles) isotopes are plotted between $N = 126$ and mid-shell, which qualitatively agree with the theoretically expected trend. Comparing the data to Fig. 19 in Ref. [87], the pronounced dip around mid-shell ($N = 104$) in the Tl chain has disappeared and a smooth trend becomes visible using the new mass values. The empirical pairing gap of Au isotopes (black squares) clearly differs from the general trend of near-spherical nuclides around mid-shell, where Au is known to be deformed. Thus, one can conclude that Tl behaves rather spherical. This is also confirmed by theory as shown in Fig. 5.4, where microscopic calculations using the Hartree-Fock-Bogoliubov (HFB) model in the spherical approximation [88, 89] (gray and black solid lines) are compared to experimental Tl data (red circles). Calculations using the HFB model [89] and including static deformation (dashed black line) clearly show discrepancies to the data around mid-shell.
Next, the conclusions from masses will be compared to another observable being sensitive to deformation: the mean-square nuclear charge radii. Figure 5.6 shows mean-square nuclear charge radii $\delta\langle r^2\rangle$ in the thallium region. Lead (blue upward triangles) and thallium (red circles) behave quite smooth. The linear downward trend for decreasing neutron number N with an odd-even staggering added on top of it, exhibits just a slight slope change around $N = 110$ and $N = 113$ for Pb and Tl, respectively. In the case of Hg (green downward triangles) a strongly enhanced odd-even staggering for $N < 106$ indicates shape staggering, whereas Au (black squares) exhibits clear deformation for $N < 107$. For lower N in the gold region more recent values are under investigation [90].
Further details about mean-square nuclear charge radii of Tl can be found in Fig. 4 in Ref. [91]. Here, lines of different strength of the quadrupole deformation parameter $\langle\beta^2\rangle^{1/2}$ are depicted. These lines are calculated based on the liquid-droplet model [92]. Beyond mid-shell and for $N < 113$, the mean-square nuclear charge radii deviate from the $\langle\beta^2\rangle^{1/2} = 0$ line indicating sphericity, however they are still below the $\beta_2 = 0.2$ line, which alludes only slight deformation.

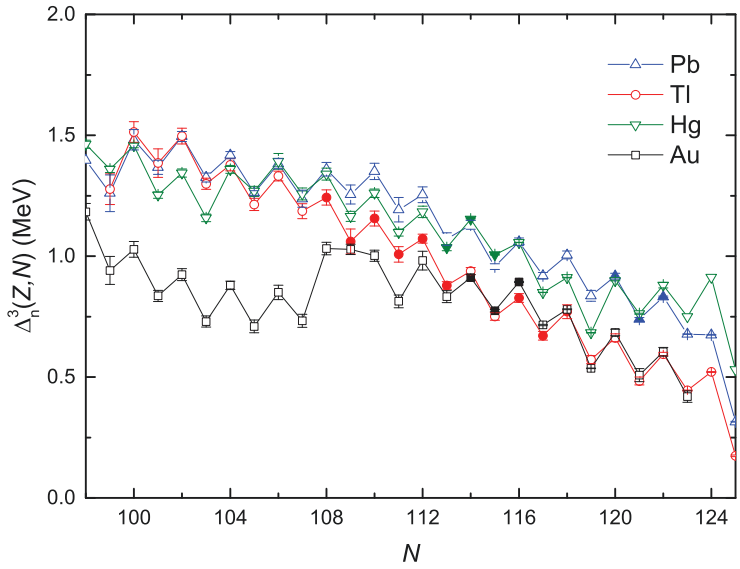

Figure 5.3: Empirical pairing gap $\Delta_n^3(Z,N)$ (see Eq. (3.5)) versus neutron number N in the thallium region. The Au chain clearly differs from Hg, Tl and Pb around mid-shell ($N = 104$). Data are taken from [58]. Data influenced by ISOLTRAP results are indicated by filled symbols.

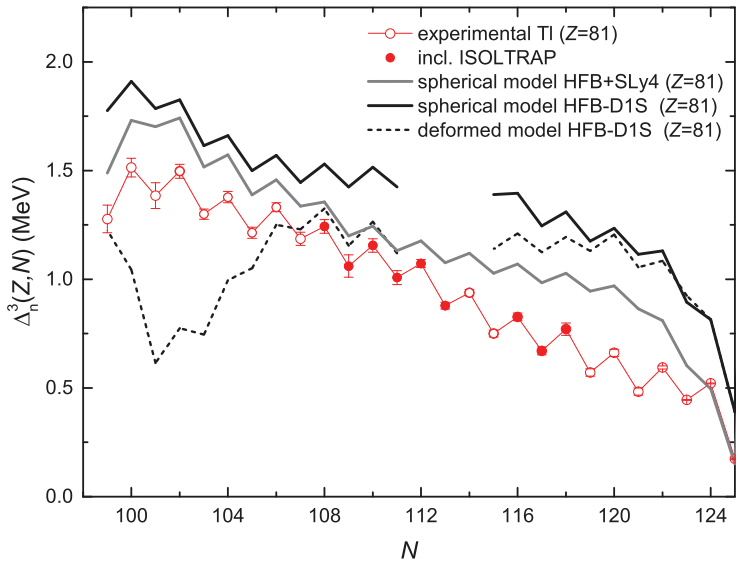

Figure 5.4: Three-point empirical pairing gap $\Delta_n^3(Z,N)$ for thallium isotopes as a function of neutron number N. The experimental values (red circles) are taken from [58] and compared to different theoretical results: a spherical HFB model by J. Dobaczewski (gray solid line) [88] as well as spherical (black solid line) and deformed (black dashed line) HFB-D1S calculations of the Bruyères-le-Châtel group [89]. The binding energies around $N = 114$ are not considered in the HFB-D1S calculations since the value likely contains a numerical artefact.

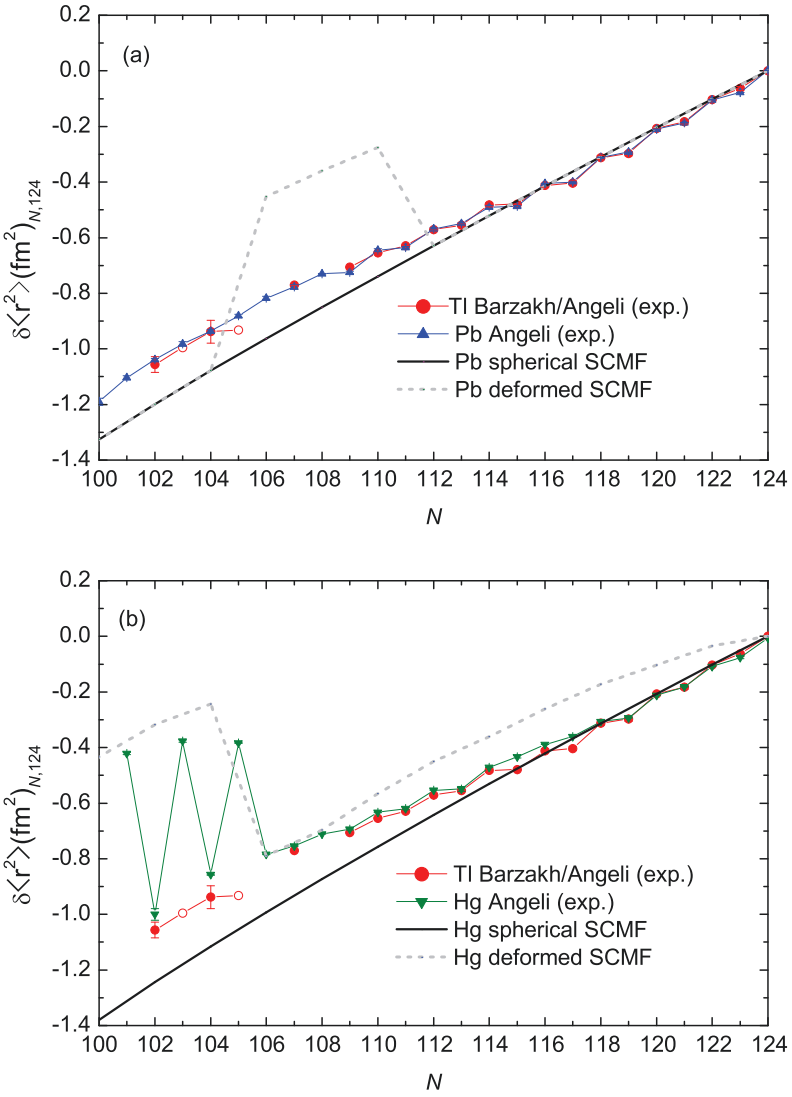

Figure 5.5: Theoretical values of $\delta\langle r^2\rangle$ [93] are compared to experimental data [91, 94]. Mean-square nuclear charge radii of (a) Tl (red circles) are compared to the spherical Pb (blue upward triangles) and in (b) Tl (red circles) is shown together with to Hg (green downward triangles). The theoretical results are plotted for the spherical case (black line) and for the statically deformed case (gray dashed line). For nuclides marked with open symbols the state ordering is not clear.

In the following, theoretical results for even-even nuclides are considered for Pb and Hg isotopes. Figure 5.5 shows a comparison between experimental and theoretical predictions of mean-square nuclear charge radii. Here, M. Bender employed a non-relativistic self-consistent mean-field (SCMF) model with the Skyrme interaction SLy4 [95] and a density-dependent pairing force to study quadrupole correlation effects for even-even nuclides. The spherical solution (black line) and the statically deformed solution (gray dashed line) for the isotopic chain of lead (blue upward triangles in Fig. 5.5(a)) and mercury (green downward triangles in Fig. 5.5(b)) are shown. As expected, experimental lead data agree better with the spherical solution than with the deformed solution although a slight deviation is visible for $N < 112$. The mean-square nuclear charge radii of thallium (red circles) show a similar behavior to this spherical solution and accordingly the lead isotopes. For mercury the spherical solution describes data down to $N = 110$ and from then on the deformed solution is closer to the data, especially in the region where shape staggering occurs. Thus one can conclude also from mean-square nuclear charge radii that the thallium isotopic chain behaves rather spherical.
Next, the empirical pairing gap $\Delta^5_{\mathrm{n}}(Z,N)$ (see Eq. (3.6)) will be considered together with mean-square nuclear charge radii information. Comparing these two observables, see Fig. 5.6 and Fig. 5.7, a coincidence can be seen in the Au isotopes for $N < 109$. A parabola appears in the empirical pairing gap and for the same region deformation is setting in as can be seen by the sudden rise in mean-square nuclear charge radii. This is similar to mercury, where the parabola is less pronounced, but present in the region of shape staggering. The isotopic chains of Tl and Pb show a smooth trend compared to Hg and Au. The fact, that the empirical pairing gap is sensititve to deformation is also discussed in Fig. 5 in Ref. [1] using a model, which confirms the impact of deformation on the five-point indicator $\Delta^5_{\mathrm{n}}(Z,N)$.

Approach (b)
The two-neutron separation energy $S_{2\mathrm{n}}$ is commonly used for the investigation of nuclear structure effects (see Eq. (3.4)). Figure 5.8 shows $S_{2\mathrm{n}}$ from the deformed Au ($Z = 79$) to the proton magic Pb ($Z = 82$) isotopes. The isotopic chains of Au (black squares), Hg (green downward triangles), Tl (red circles) and Pb (blue upward triangles) show all the general linear trend going down with a more or less pronounced odd-even staggering superimposed. Note, that this staggering is not the same, as the staggering in Fig. 3.4. Since $S_{2\mathrm{n}}$ is taking into account only every second isotope, the odd-even staggering, which has its origin in the pairing energy, is not visible. The Tl chain of $S_{2\mathrm{n}}$ became smoother by adding new ISOLTRAP data. In the case of Au a clear irregularity is visible around $N = 109$ giving a hint to a change in nuclear structure.

Next, the unexpected staggering of $S_{2\mathrm{n}}$ will be discussed. Initially the so-called γ-parameter was introduced by B. S. Reehal [96] to describe the strength of staggering of mean-square nuclear charge radii. The γ-parameter is given as

$$\gamma(X(N)) = 2\frac{X(N) - X(N-1)}{X(N+1) - X(N-1)}, \tag{5.10}$$

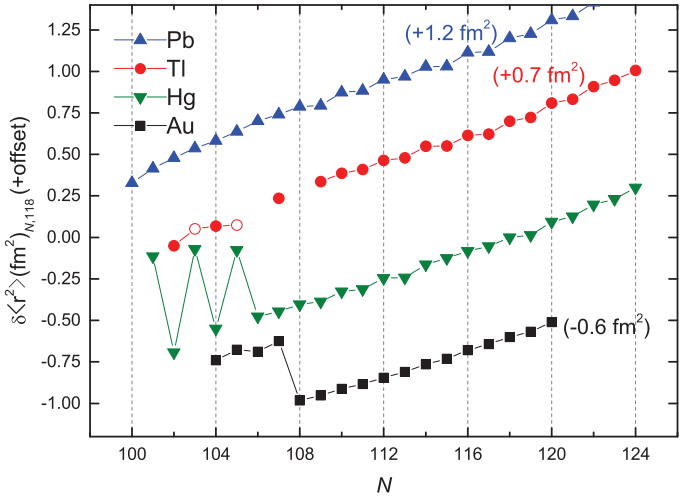

Figure 5.6: Differences in mean-square nuclear charge radii for ground states in the thallium region. It is obvious that for gold (black squares) one can see deformation setting in at $N = 107$ and in the case of mercury (green downward triangles) shape staggering is visible for $N < 106$. Lead (blue upward triangles) and thallium (red circles) shows a rather smooth trend going down for decreasing neutron numbers. Note that an offset, as indicated for each nuclide, has been added for better visibility. Data were taken from [91, 94]. Error bars are smaller than the symbol size. Open symbols denote nuclides where the state ordering is not certain.

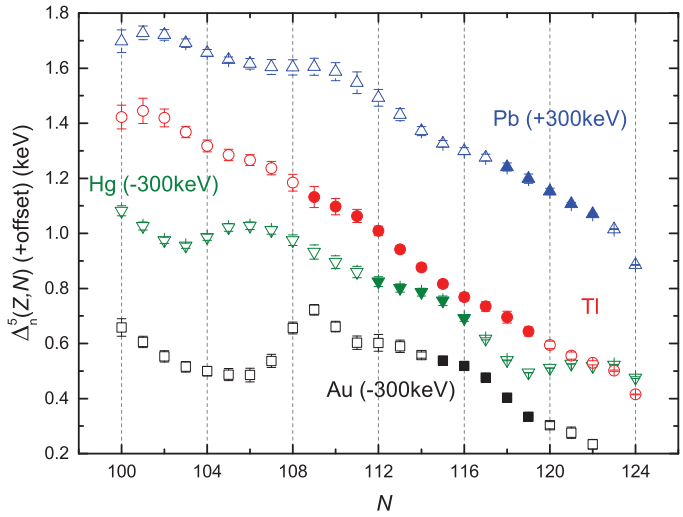

Figure 5.7: Empirical pairing gap $\Delta^5_n(Z, N)$ (see Eq. (3.6)) versus neutron number N in the thallium (red circles) region. For better visibility an offset was added to the values of Au (black squares), Hg (green downward triangles) and Pb (blue upward triangles) as indicated in parentheses. A dip is visible in Hg for $100 \leq N \leq 106$ and for Au in $100 \leq N \leq 108$. This coincides with irregularities in mean-square nuclear charge radii. Data were taken from [58]. Filled symbols denote data including new ISOLTRAP results.

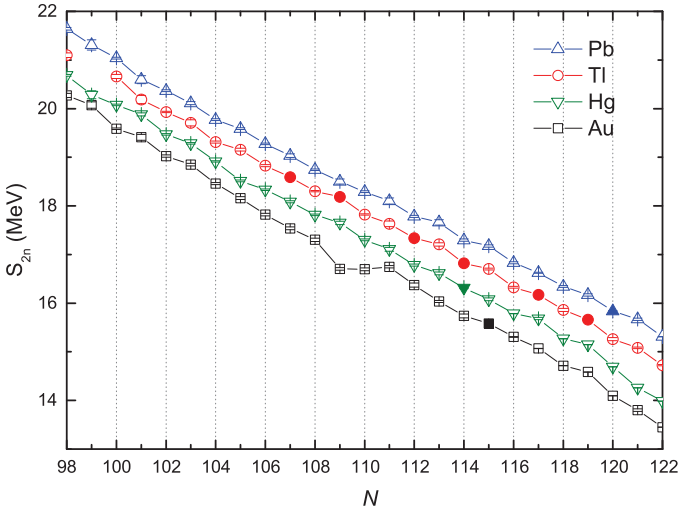

Figure 5.8: Two-neutron separation energies S_{2n} versus neutron number N in for thallium isotopes (red circles) and its neighbors lead (blue upward triangles), mercury (green downward triangles) and gold (black squares). Filled symbols indicate a contribution from the ISOLTRAP data discussed within the present thesis. In the gold chain a clear dip around $N = 109$ is visible while the lead, thallium and mercury chain follow a rather smooth trend. Data were taken from [58].

with X(N) being an observable that exhibits odd-even staggering, e. g. mean-square nuclear charge radii. Here, it will be tested to what extent such an investigation can be mapped onto masses, i. e. the two-neutron separation energy.
The γ-parameter can be modified by taking the absolute value and applied to the two-neutron separation energy. Looking at $\gamma\prime = |\gamma(S_{2n}(N)) - 1|$ instead of $|\gamma(S_{2n}(N))|$ leads to a positive number being close to zero, whereas $\gamma\prime = 0$ reflecting that there is no staggering present at all. The comparison of

$$|\gamma(S_{2n}(N)) - 1| = \left|2\frac{(S_{2n}(N) - S_{2n}(N-1))}{S_{2n}(N+1) - S_{2n}(N-1)} - 1\right| \tag{5.11}$$

to the slope of the empirical pairing gap $\Delta^5_n(Z,N) - \Delta^5_n(N-1)$ is shown in Fig. 5.9 for (a) Au, (b) Hg, (c) Tl and (d) Pb. A symmetric behavior of both curves is clearly visible. In case of gold, in the region around $N = 107$ (blue shaded) a deviation from the symmetric pattern is observed. Similar effects are present in mercury. Here, the region, which is known for shape staggering (compare Fig 5.6), is not symmetric (see Fig. 5.9 b, blue shaded). Considering Tl and Pb, a symmetric pattern is visible along the whole isotopic chain. Here, error bars are quite large compared to Au and Hg, so that arguments could be questioned. In order to see whether this link is reproducible in other regions of the nuclear chart, lower Z nuclides have been studied as well. The same behavior as in the thallium region could be demonstrated.
Taking the absolute in Eq. (5.11) of course some information is neglected. Considering γ in its initial form it reveals tiny irregularities, such as slope changes in the trend of

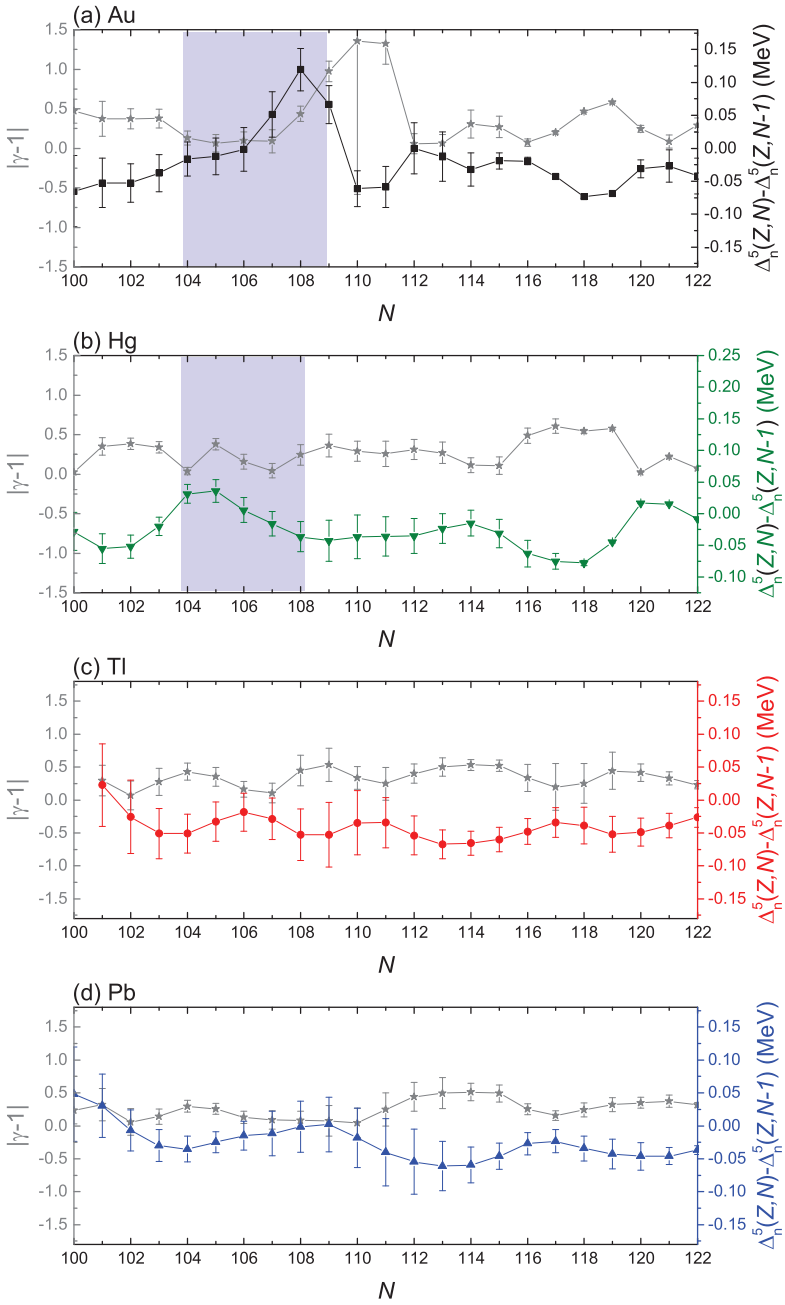

Figure 5.9: Slope of the empirical pairing gap $\Delta_n^5(Z,N) - \Delta_n^5(Z,N-1)$ for (a) Au (black squares), (b) Hg (green downward triangles), (c) Tl (red circles) and (d) Pb (blue upward triangles) compared to $\gamma\prime$ (gray stars) of the corresponding versus neutron number N. The shaded area in (a) indicates a region where Au exhibits deformation. The shaded area in (b) shows the region at which shape staggering is present in Hg. Data are taken from AME2012. For details see text.

S_{2n}. Another feature, which is revealed by looking at γ is the fact that the strength of staggering is fluctuating in a periodic manner along the isotopic chains.
This study of the strength of staggering in S_{2n} through the $\gamma\prime$ parameter exemplifies that deformation can affect mass values, such that higher-order mass formulas can make it quantitatively accessible. Although tested only on a few cases, this shows that mass differences offer information on the deformation of a nucleus complementary to that from mean-square nuclear charge radii.

Low-Lying Isomeric States

The investigation of low-lying isomeric states reveals further information on the development of collectivity along the Tl isotopic chain. Odd-N Tl isotopes for neutron numbers $103 \leq N \leq 121$ exhibit an $I = 2$ ground state and $I = 7$ isomeric state whereas even-N Tl isotopes hold an $I = 1/2$ ground state and an $I = 9/2$ isomeric state which exhibits deformation [91]. The energy of the first isomeric state in odd-N Tl isotopes decreases from $N = 126$ towards mid-shell ($N = 104$) and thus a level inversion seems within reach. The spherical shell model yields an oversimplified description of Tl isotopes which becomes clear by comparing the data with spin state predictions. A reason for the state ordering might be the effect of shape coexistence or a slight oblate deviation [97]. According to the spherical shell model the valence proton occupies the $s_{1/2}$ orbital but many $I = 9/2$ isomers have been found in the Tl isotopic chain, meaning that the valence proton occupies the $h_{9/2}$ orbital beeing above the shell closure at $Z = 82$. The excitation energy of the $I = 9/2$ isomer is decreasing for lower neutron numbers (as shown in Fig. 5.10, red circles) and reaches a minimum of less than 300 keV at $N = 108$. This reflects the evolution of the $h_{9/2}$ intruder. In the gold chain the $I = 9/2$ state is decreasing almost to zero around mid-shell (see Fig. 5.10, black squares), which results in deformation of the ground states setting in at $N = 107$. The slight deviation of Tl ground states from the spherical predictions (see Fig. 4 in Ref. [91] and Fig. 5.5) could thus be the result of ground state correlations. This is also supported by the presence of the low-lying intruder state.

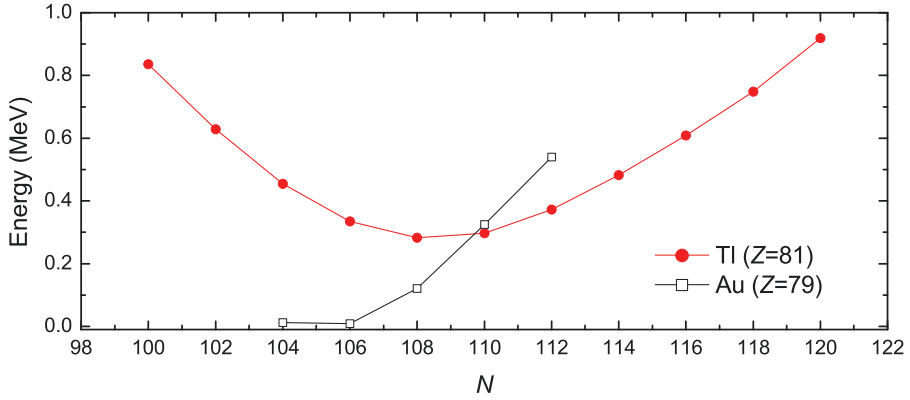

Figure 5.10: Excitation energy of the $I = 9/2$ states of thallium (red filled circles) and gold (black open squares) isotopes as a function of neutron number N. The first excited state of even-N Tl isotopes shows a parabolic shape with a minimum at $N = 108$. It reflects the evolution of an intruder, wheras the $I = 9/2$ state in Au is responsible for the deformation. The energy of the isomer in Au decreases from $N < 113$ and reaches nearly zero at mid-shell. Data were taken from [58, 98]. Error bars are smaller than the symbol size.

Chapter 6

The PENTATRAP Mass Spectrometer

The PENTATRAP experiment [38] has been developed and set up at the Max-Planck-Institut für Kernphysik, Heidelberg. The first part of the present chapter will briefly introduce the key components of the setup such as ion sources, the Penning-trap mass spectrometer, and the beamline, which interfaces the ion sources with the mass spectrometer. The second part will address the PENTATRAP magnet and the stabilization systems, which were installed to reduce magnetic field fluctuations.

6.1 The Experimental Setup of PENTATRAP

As shown in Fig. 6.1 the experimental setup extends over two floors. The ion source is located on the first floor in the accelerator hall, whereas the mass spectrometer is located in the PENTATRAP laboratory below. The different parts of the setup as well as the control system and measurement principle are introduced in the following.

6.1.1 Ions Sources

The cyclotron frequency scales with the charge-to-mass ratio of the ion. Thus, the use of ions in very high charged states, i. e. high absolute cyclotron frequencies, is advantageous in frequency measurements with relative uncertainties $\leq 10^{-11}$. For the production of highly charged ions different ion sources are available in form of a commercial electron beam ion trap (EBIT), or will be accessible in the future. In an EBIT, ions are axially confined due to a voltage applied to drift tubes. In addition, a magnetic field is used to compress a monoenergetic electron beam, which provides in combination with the magnetic field itself radial confinement of the ions. The electron beam ionizes the atoms subsequently until high charge states are produced.

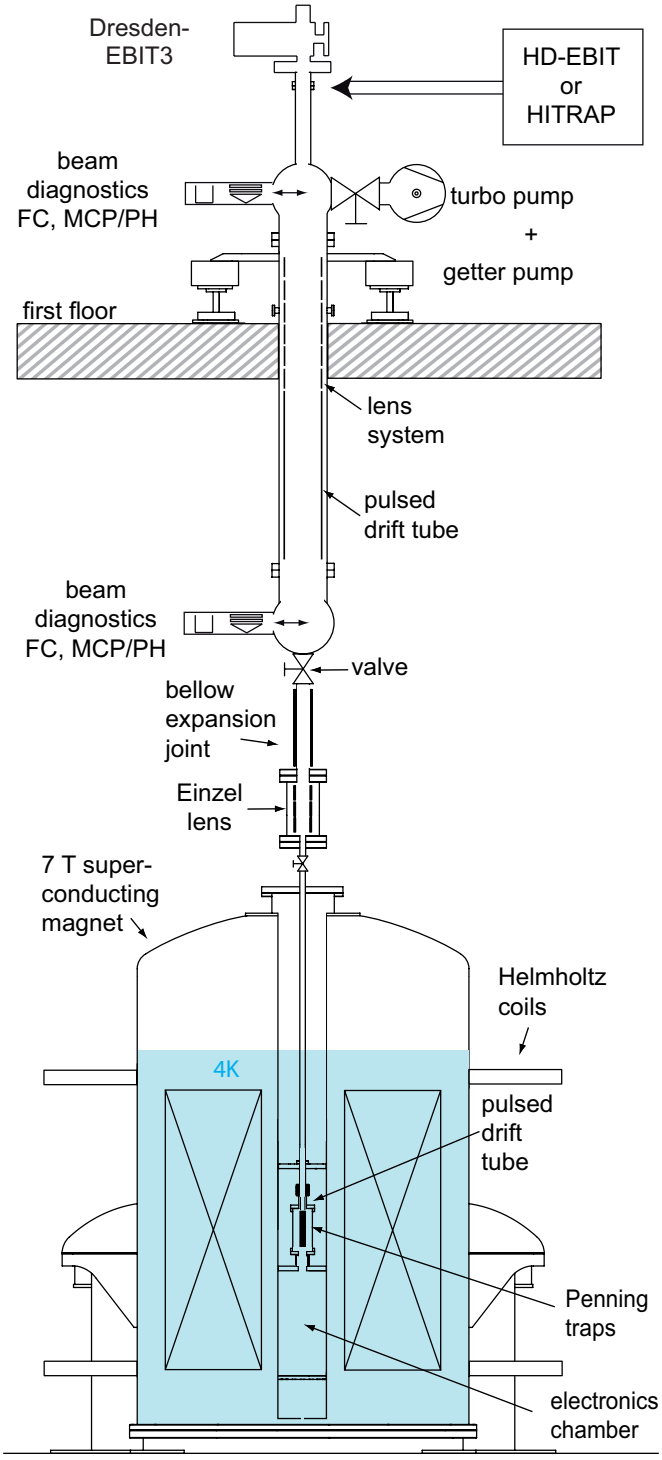

Figure 6.1: Schematic of the PENTATRAP setup. The ions are produced in the accelerator hall on the first floor. A two meter long beamline equipped with two diagnostic stations transfers the ions to the temperature-stabilized PENTATRAP laboratory where a superconducting magnet is installed. The ions are decelerated by drift tubes before they enter the trap tower. The trap chamber and the electronics chamber are installed in the center of the magnet in a 4 K environment.

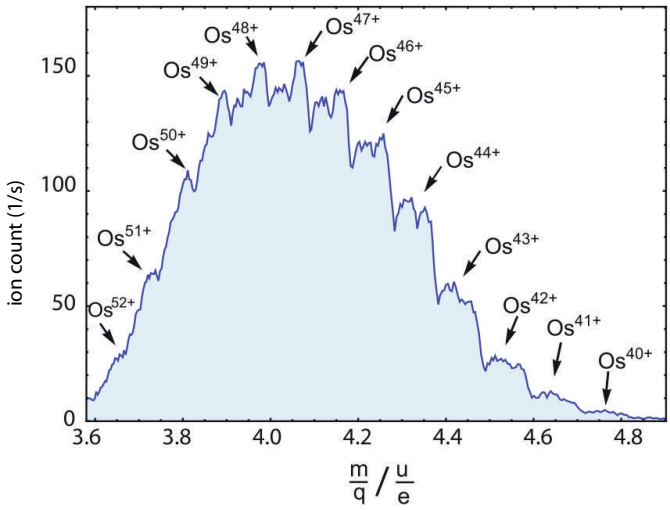

Figure 6.2: Osmium spectrum produced with the Dresden-EBIT3 in the commissioning phase of PENTATRAP. The ions were detected with an MCP detector for different charge-to-mass ratios.

Dresden-EBIT3

PENTATRAP is currently connected to a commercial ion source called Dresden-EBIT3 [99]. It is a small room temperature EBIT combined with a Wien filter, which allows one to choose a certain mass-to-charge ratio of the extracted ions. The Dresden-EBIT3 with a maximum electron beam energy of 15 keV and an electron beam current of about 50 mA is capable of producing bare ions up to $Z = 30$. Nuclides with higher Z can be ionized to helium- or neon-like charge states. The Dresden-EBIT3 was employed for commissioning of PENTATRAP. Amongst others, the production of ^{187}Re and ^{187}Os ions with charge states up to 52+ (see Fig. 6.2) was demonstrated with production rates of few hundreds of ions per second [38]. The decay of ^{187}Re to ^{187}Os is relevant for applications in neutrino physics. Details are discussed in [100].

Heidelberg-EBIT

The Heidelberg-EBIT [101] is located close to the PENTATRAP laboratory and serves as an ion source for various experiments. It is planned to connect the PENTATRAP experiment to the Heidelberg-EBIT in the future in order to provide access to heavy ions in high charge states up to $^{208}Pb^{81+}$. Currently a maximum electron beam energy of 100 keV allows for the production of Hg^{78+} or Ba^{55+} ions.

HITRAP

For the far future it is planned to adapt the PENTATRAP experiment to the HITRAP facility [102], which is located at the GSI Helmholtzzentrum für Schwerionenforschung (GSI), Darmstadt. HITRAP is connected to the accelerator complex of GSI and serves as

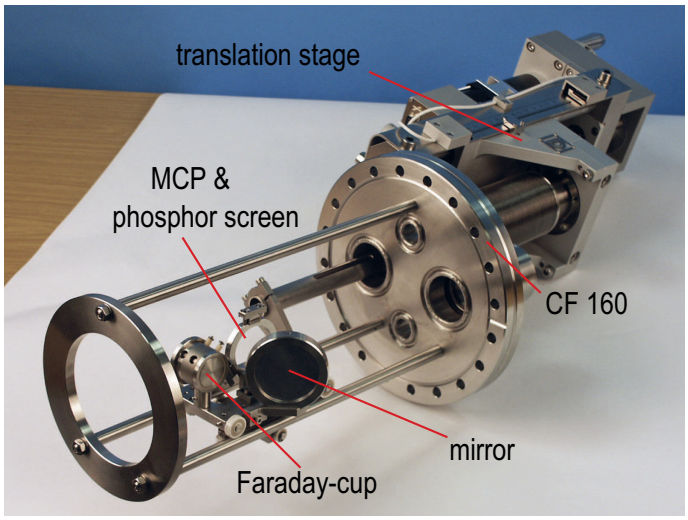

Figure 6.3: Photograph of the diagnostic system (KVI for HITRAP design) containing an MCP detector with a phosphor screen and a Faraday cup. Taken from [103].

a decelerator of the ions. At HITRAP heavy highly-charged bare nuclides will be available with masses up to uranium. GSI is currently the only facility where U^{92+} can be produced. In contrast to the Heidelberg-EBIT, at HITRAP there will be in addition highly-charged ions available with low half-lives of several tens of seconds. Very low kinetic energies of ion beams of only a few meV·q will be reached.

6.1.2 Beamline and Beam Diagnostics

The PENTATRAP beamline has a length of about 2 m and serves as a connection between the ion source placed in the accelerator hall and the Penning-trap mass spectrometer installed in the PENTATRAP laboratory (see Fig. 6.1). In the beamline, ion beam diagnostic systems are employed for optimization purposes. As shown in Fig. 6.3, these systems hold MCP detectors with phosphor-screens and Faraday cups. Hence, the beam intensity and the shape of the beam can be monitored, which facilitates the optimization of the ion transport. Below the first diagnostic station einzel lenses and deflectors are mounted to transport the ions and tune the shape of the ion beam. Moreover, a pulsed drift tube is installed to lower the ion energy from about 7 keV/q down to few hundred eV/q for an efficient ion injection into the cryogenic region in the strong magnetic field with the subsequent capture of ions in the traps. Just above the magnet a second diagnostic station is installed to monitor the ion beam before entering the cold bore. In the bore a second drift tube is placed just above of the Penning-trap tower. Here, the ion beam energy is reduced down to a few eV/q to enable the ion capture in one of the traps.

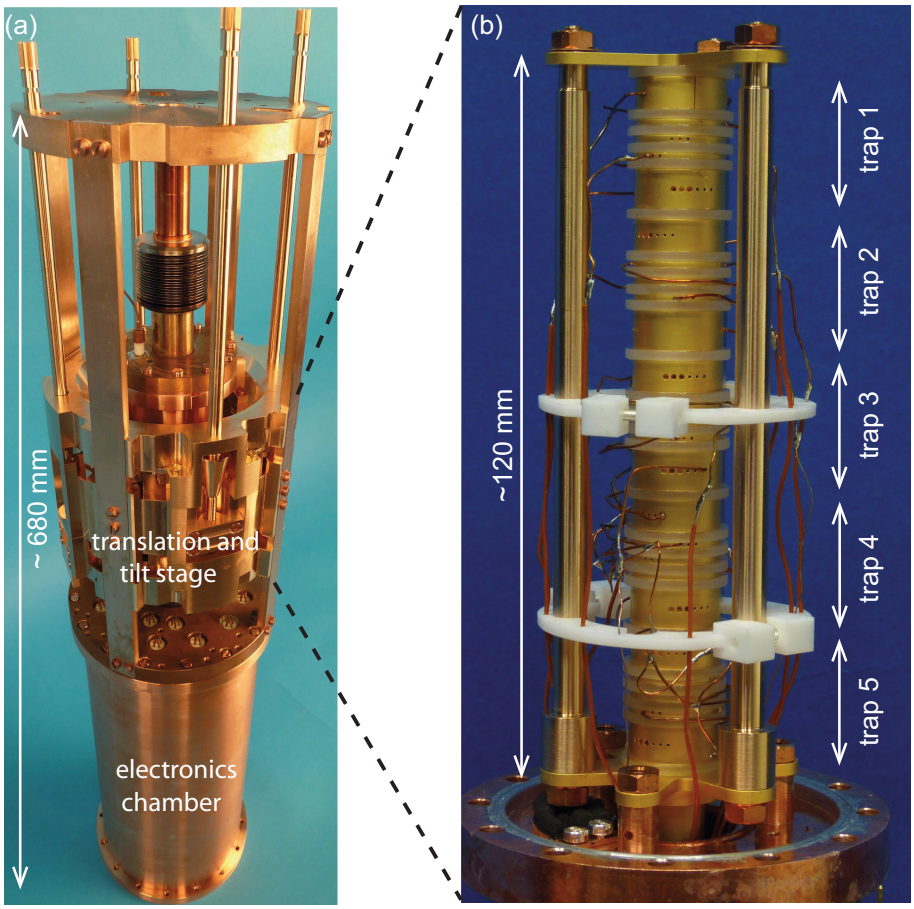

Figure 6.4: (a) Cryogenic assembly including the translation and tilt stage, the trap tower and the electronics chamber. (b) Penning-trap tower containing 5 Penning traps with 5 electrodes each. Sapphire rings are used as insulators.

6.1.3 The Cryogenic Assembly and the Trap Tower

The trap chamber with corresponding detection electronics is immersed in the liquid helium cryostat of the superconducting magnet, which also cools the coils of the magnet. Such a configuration allows in combination with charcoal absorbers to reach very good vacuum conditions of $p < 10^{-13}$ mbar, which allows ion storage times of several days. As shown in Fig. 6.4 (a), the beamline for the ion transport from the ion source to the trap is connected via a flexible titanium bellow to the top of the trap chamber, which is mounted in the center of a translation and tilt stage. This stage enables the alignment of the symmetry axis of the trap tower (see Fig. 6.4 (b)) to the magnetic field lines. It provides the possibility to translate or to tilt the tower by 2 mm or 1°, respectively. The trap tower consists of five identical, cylindrical, compensated and orthogonalized Penning traps [104]. Each trap consists of five electrodes, which are split in parts to enable dipolar

or quadrupolar excitations. Below the trap chamber a flexible titanium bellow is mounted and the electronics chamber containing the resonators for the ion detection system is attached.
In order to setup a Penning trap for high-precision mass measurements the mechanical part, i. e. trap electrodes and insulators, has to be manufactured very precisely, i. e. the tolerances of the trap electrodes are $\pm 5\,\mu m$ [38]. Apart from the mechanical unit, an essential component of a Penning trap is the electromagnetic field, which has to be stable as much as possible. In order to stabilize the magnetic field a lot of effort has been invested, which will be described in detail in Chap. 6.2. The trapping potential in a Penning trap is created by applying ultra-stable voltages to the five electrodes. As the PENTATRAP trap tower contains a stack of five traps, a voltage source with 25 channels is required to supply the stable trapping potential. Furthermore, in order to enable ion transport from one trap to another, these 25 channels have to be equipped with capabilities to dynamically change voltages. As there is no commercial voltage source available, which fulfills all requirements, an ultra-stable voltage source has been developed within this thesis in collaboration with the electronics workshop at MPI and the PTB Braunschweig. A detailed description of this voltage source is given in Chap. 7.

6.1.4 The PENTATRAP Control and Data Aquisition System

The *LabVIEW*^{TM} based control system of PENTATRAP was initially developed at GSI for experiments employing the time-of-flight detection technique [105]. It was adapted within the Ph.D. thesis of M. Goncharov [106] to the PENTATRAP setup in order to facilitate the control of an FT-ICR measurement. The control system is used to apply the settings for all hardware components such as ion sources, ion optics, diagnostics and the StaReP voltage source. A detailed description on the control of the StaReP voltage source is given in Chap. 7.2. Moreover, the control system is also used for data acquisition. Later on it is planned to implement also an online data analysis program and a logbook. Due to the high flexibility of the control system it will be possible to add elaborated measurement schemes. So far commissioning of the control system has been performed during first tests employing the Dresden-EBIT3. Moreover, the detection of the first trapped ions at PENTATRAP was performed with the control system. The high flexibility of the system allows one to change settings or even to switch damaged components without stopping the experiment. More details are given in [106].

6.1.5 Ion Detection

The ion detection at PENTATRAP will be realized via the FT-ICR technique, which is described in Chap. 2.2.3. The measurement of the eigenfrequencies will yield the free cyclotron frequency employing the invariance theorem. The so-called monitor trap (trap 1, see Fig. 6.5) is equipped with a cyclotron tank circuit to monitor magnetic field fluctuations by measuring the cyclotron frequency of an ion with a well-known mass. Furthermore, an axial tank circuit is connected to trap 1 to enable the monitoring of voltage fluctuations. The detection circuits for the mass determination are axial tank circuits, which are at-

tached to the measurement traps (trap 2–5). These allow one to measure ν_Z for a large variety of q and m, as the voltage can be tuned accordingly for a given axial frequency. The radial frequency $\nu_\pm$ can be measured via ν_Z employing sideband coupling [107]. In addition, cyclotron tank circuits are attached to trap 2–5. These are necessary for the cleaning and cooling procedure, which is carried out to prepare the ion for the measurement. Details of the detection system and the development of the tank circuits are described in the Ph.D. theses of C. Roux [108] and A. Dörr [109].

6.1.6 The Measurement Principle

In many Penning-trap experiments, two ion species are measured subsequently in order to determine the mass ratio. The time interval between the measurements has to be as small as possible since temporal magnetic field fluctuations are the limiting factor of the accuracy on mass-ratio measurements. To overcome this issue, PENTATRAP is equipped with five traps. This enables a large variety of measurement schemes, including the possibility for fast ion exchange between the traps. One example is illustrated in Fig. 6.5 and will be discussed in the following. There are 3 ion species loaded in the traps. An ion (monitor ion, gray) with a well- known mass is stored for a continuous measurement of ν_c or ν_z in trap 1. That allows, according to Eq. (2.5) and Eq. (2.9), to deduce magnetic field fluctuations or voltage fluctuations, respectively. Traps 2–5 serve for preparation and mass-ratio measurements of the ions of interest. Measuring the cyclotron frequency of the ion with charge state q_1, mass m_1 (see Fig. 6.5, green) in the magnetic field $B_3(\mathrm{t}_1)$ of trap 3 and the cyclotron frequency of the ion with charge state q_2, mass m_2 (see Fig. 6.5, black) in the magnetic field $B_4(\mathrm{t}_1)$ of trap 4 simultaneously at time t_1 allows to determine the frequency ratio:

$$R(t_1) = \frac{\nu_{\mathrm{c},1}}{\nu_{\mathrm{c},2}} = \frac{\frac{q_1}{m_1} B_3(t_1)}{\frac{q_2}{m_2} B_4(t_1)}. \tag{6.1}$$

This measurement is repeated at time t_2 after swapping the ions by shifting them from traps 3, 4 and 5 to the adjacent traps 2, 3 and 4 resulting in:

$$R(t_2) = \frac{\nu_{\mathrm{c},1}}{\nu_{\mathrm{c},2}} = \frac{\frac{q_1}{m_1} B_4(t_2)}{\frac{q_2}{m_2} B_3(t_2)}. \tag{6.2}$$

For $q_1 = q_2$ the mass ratio is obtained by:

$$\sqrt{R(t_1) \cdot R(t_2)} = \frac{m_2}{m_1} \cdot \sqrt{\frac{B_3(t_1)}{B_4(t_1)} \cdot \frac{B_4(t_2)}{B_3(t_2)}} = \frac{m_2}{m_1}. \tag{6.3}$$

The ratio B_3/B_4 is assumed to be constant over the time because it depends mainly on the geometry of the magnet. Thus, it cancels out in Eq. (6.3). The mass ratio measurement is repeated several times to average out the small temporal fluctuations of the ratio B_3/B_4. In addition several magnetic field stabilization systems have been installed (see Chap. 6.2). The unique five-trap design allows for many more measurement schemes which have to be tested in order to find the best.

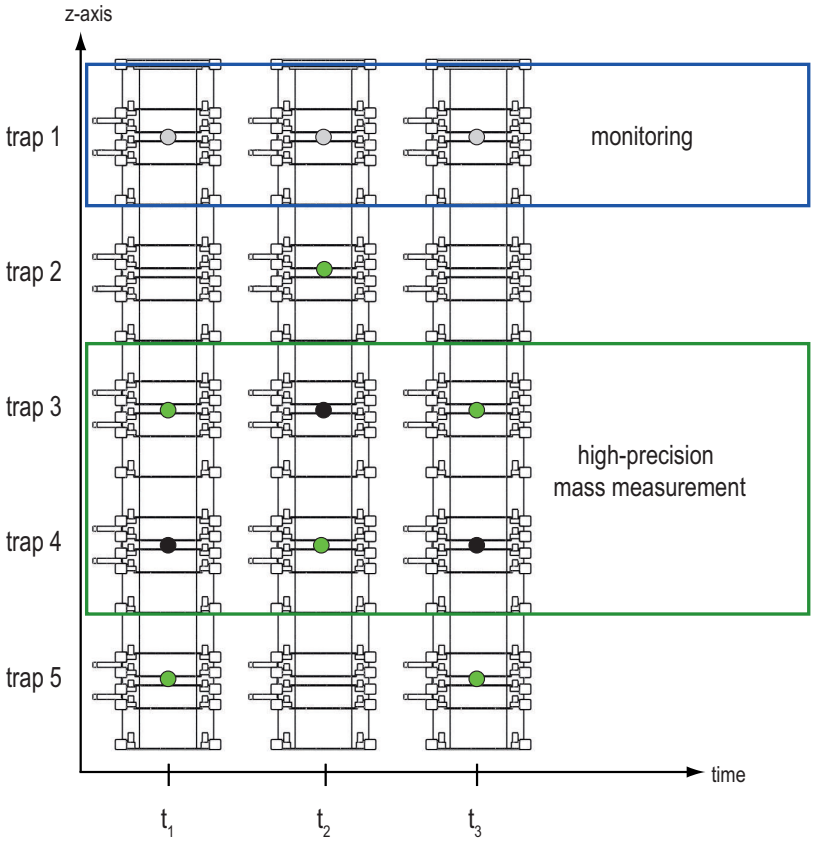

Figure 6.5: Example of a measurement scheme at PENTATRAP. The first trap contains an ion of a well-known mass (gray) and enables the monitoring of magnetic field fluctuations or voltage fluctuations by measuring ν_c or ν_z, respectively. The remaining four traps are used for simultaneous mass-ratio measurements. One ion species (green) is initially stored in trap 3 and trap 5, while a second ion species (black) is captured in trap 4. The existence of trap 2 facilitates to move the ions to adjacent traps, meaning effectively swapping ion species in trap 3 and trap 4. For details see text.

6.2 Stabilization Systems at PENTATRAP

The PENTATRAP experiment is placed in a laboratory with different stabilization systems to reduce environmental influences on the magnetic field, which would lead to an increased uncertainty in the mass measurements. In order to reduce e. g. the influence of fluctuations of the earth's magnetic field and other environmental distortions a regulation system was implemented within the Ph.D. thesis of J. Repp [100] and the Bachelor's thesis of A. Rischka [110]. The vertical components of low frequency stray magnetic fields, are actively shielded by means of a feedback control system based on a flux-gate magnetometer, which is connected to a pair of Helmholtz coils mounted around the magnet [38]. Combined with the self-shielding of the magnet (shielding factor >100), the estimated total shielding factor exceeds 1000. In order to shield high-frequency magnetic fields and stray electrical fields, the PENTATRAP magnet can be enclosed in an aluminum housing. The aluminum housing is equipped with a temperature stabilization system which reduces temperature fluctuations to about 20 mK per day [38]. Moreover, the magnet is mounted on antivibration pneumatic pads as shown in Fig. 6.6. These are installed on vibrational damped concrete blocks to achieve a decoupling from the building. Thus, the vibration amplitude of the concrete blocks remains below 1 µm. Apart from these external arrangements, a stabilization of the helium pressure and helium level in the magnet is implemented. With all stabilization systems included we are aiming for a temporal stability $\Delta B/B \cdot 1/\Delta T$ of at least a few ten ppt per hour.

In the following, the setup and commissioning of the helium pressure and level stabilization will be discussed. The superconducting 7 Tesla magnet of PENTATRAP holds a cold bore in which the trap chamber and the electronics chamber are cooled down by liquid helium, as shown in Fig. 6.1. The helium reservoir contains the coils of the magnet. Both, the bore and the reservoir are connected by a small hole ($\varnothing < 1$ cm) at the bottom of the bore (see Fig. 6.7). The temperature of boiling liquid helium is a function if its pressure. Consequently the materials with a temperature-dependent susceptibility installed in the vicinity of the trap tower influence the magnetic field if the temperature changes. Thus a pressure stabilization of the helium gas in the bore of the magnet is of great importance. As the pressure will be kept constant in the bore, a pressure change in the reservoir will cause a change of the level in the bore. A level fluctuation in the bore would result in temperature fluctuations and thus, the magnetic field is affected by a level change.
The basic principle of the stabilization system relies on the stabilization implemented at the THe-Trap experiment [111, 112], which was adapted from [113]. At THe-Trap a pressure and level stabilization of about ± 0.6 µbar and ± 40 µm has been demonstrated. At PENTATRAP we are aiming for similar stabilities. The amount of materials with a strongly temperature-dependent susceptibility such as G10-CR[1] is much smaller at PENTATRAP compared to the setup of THe-Trap. Therefore, the requirements on the stabilization system at THe-Trap are more demanding.

[1] G10-CR is a fiber glass with a temperature-dependent susceptibility [114, 115].

Figure 6.6: Photograph of the PENTATRAP magnet. On the top, a part of the beamline towards the ion source is shown with the beam diagnostic station attached. The magnet is placed on antivibration pneumatic pads in the center of the Helmholtz coils, which are used to reduce environmental magnetic fluctuations.

6.2.1 The Setup of the Helium Pressure and Level Stabilization System

The PENTATRAP magnet contains two connected chambers filled with liquid helium: the reservoir and the bore (see Fig. 6.7). The aim is, to stabilize the helium pressure and helium level in the bore as perfect as possible. Thus, the pressure regulation has to compensate the helium boil-off. As there are no commercial stabilization systems available, the design was adapted from THe-Trap [111]. Several modifications were made to adjust the stabilization system to the PENTATRAP magnet.

Requirements

Differential pressure transducers with a high resolution of $\leq 1\,\mu$bar are available from *MKS Instruments*. These can be combined with an absolute pressure reference (APR) in order to stabilize the pressure in the bore of the magnet relative to the APR. The PENTATRAP APR was adapted from [112] and constructed and setup at MPIK.
The level measurement is more challenging as the detection of the level has to be carried out in the cryogenic region of the bore, in contrast to the pressure, which is measured at room temperature. Thus, the level sensor must be suitable for cryogenic environments and at the same time the heat transfer to the system has to be minimized. Level detection techniques based on the measurement of the resistance of a superconducting wire immersed in liquid helium would lead to an increased helium boil-off and would disturb the stabilization mass measurement tremendously. The readout of the commercial level sensor, which was delivered with the magnet and is placed in the reservoir, results in a rise of pressure of a few hundred µbar when a current flows through the wire to determine the level. Therefore, a capacitive level sensor was chosen for the helium level stabilization as it provides a high resolution and yields in a low heat input. It contains a resonator placed in the bore and an oscillator at room temperature, as shown in Fig. 6.8. Details are described in [103].

Principle of the Stabilization System

In order to describe the basic principle of the stabilization system one can assume two circuits (green and purple circuit in Fig. 6.7), which are coupled due to the small hole at the ground of the bore. Two dosing valves D1 and D2 are employed in the regulation system of the level and pressure, respectively.

- In cases where the level is too high/low the dosing valve D1 will open/close leading to a pressure release/build up in the reservoir. Due to the connection of the bore to the reservoir, the level in the bore is affected by switching D1.
- In cases when the pressure in the bore is too high, D2 will open. For a pressure below the reference pressure D2 will be closed, such that the helium boil-off will lead to a rise of the pressure.

Note, that the pressure release is carried out actively by opening the valves D1 and D2, while a pressure build-up is only possible by closing the valve and waiting until the helium

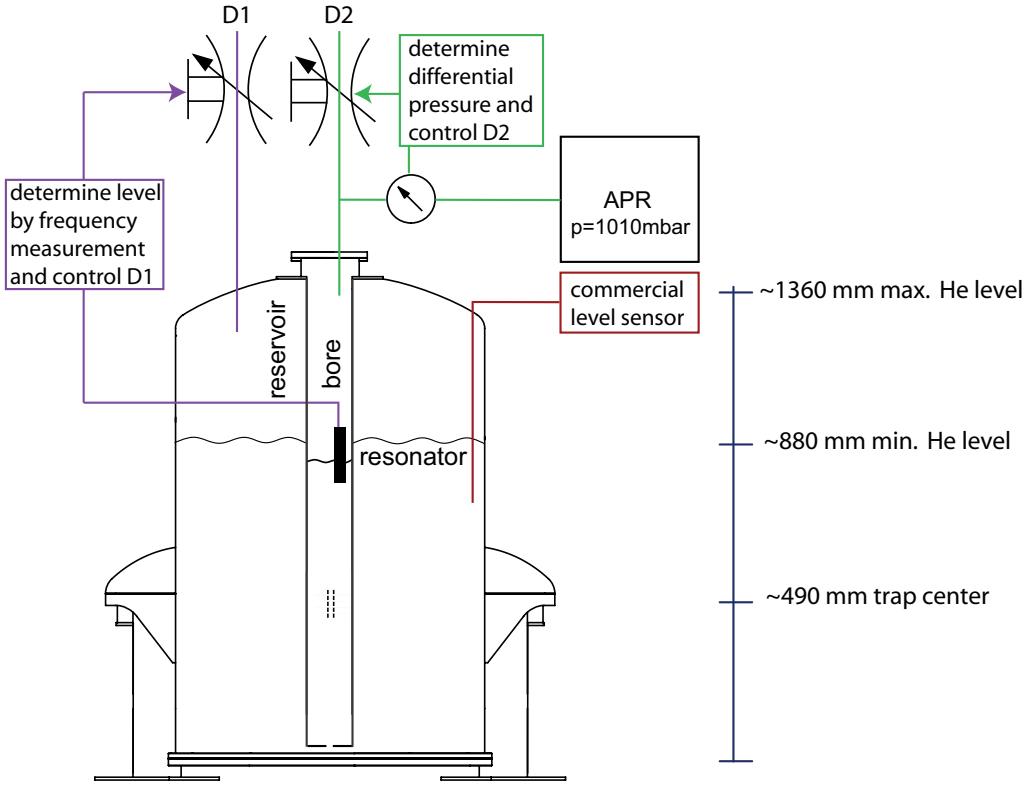

Figure 6.7: Principle of the He pressure and level stabilization system. The level and pressure stabilization circuit is shown in purple and green, respectively. The commercial level sensor (brown) serves for testing and characterization purposes only. It will be switched off while precision measurements are performed. For details see text.

boil-off is sufficient to reach a certain pressure.
On the one hand, the dosing valves (D1, D2) have to be chosen large enough to compensate the boil-off, which is about 1 l helium in gas form per minute at each valve. On the other hand the fine tuning of the valve is required with a high resolution to tune the pressure in the µbar range.
The level stabilization system is based on the stabilization of the frequency of a resonator (Fig. A.1), which is partly immersed in liquid helium. As soon as the He level changes the resonance frequency of the resonator is affected. The frequency signal triggers the controller to tune the valve D1, which is regulated to compensate for the frequency shift.

Absolute Pressure Reference (APR)

The differential pressure transducer *AD120* (*MKS Instruments*) is connected to an absolute pressure reference (APR). The APR design is adapted from the APR at THe-Trap.

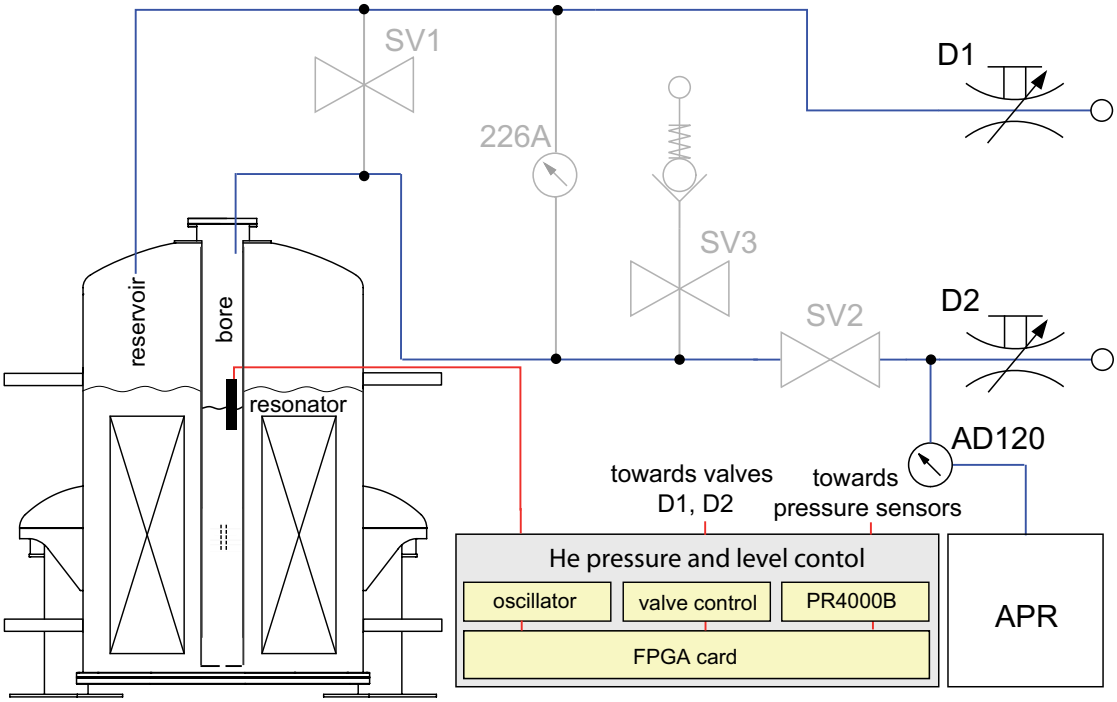

Figure 6.8: Schematic of the helium pressure and level stabilization system. Red lines indicate electrical signals and blue lines represent the helium-gas filled tubes of the system. Dosing valves (D) for the stabilization system and safety valves (SV) are shown. The pressure sensors *226A* and *AD120* are used for test and stabilization purposes, respectively. All parts shown in gray serve as safety system to prevent damage of the pressure sensor *AD120* in case of a quench or other events causing a rise of pressure. All safety valves shown here are drawn in operation mode. Figure adapted from [103].

It is a non-magnetic stainless steel chamber with a volume of 20 l enclosed in a styrofoam housing (see Fig. A.2). The styrofoam provides damping of environmental temperature fluctuations in the laboratory. In order to actively temperature stabilize the APR a heating wire is wrapped around the chamber between the styrofoam and the stainless steel chamber. The PENTATRAP APR was installed at the stabilization system of THe-Trap, where the active temperature regulation has been successfully tested. However, the APR test at THe-Trap has also shown, that there is a drift of the APR pressure of about 80 µbar/day, which has to be further investigated. For test purposes the APR has been filled with nitrogen to a pressure of 1010 mbar. Later, it will be filled with helium as there will be a connection during the setup of the stabilization system of the APR to the magnet system. The whole stabilization system is held above the environmental pressure to prevent air entering the system in case of a leak.
The environmental air pressure has been observed for several month. Depending on the weather the pressure fluctuates from 960 to 990 mbar. As the *AD120* sensor should not be exposed to more than 100 mbar differential pressure, the pressure in the bore and thus in the APR has to be chosen such that $p_{\mathrm{APR}} - p_{\mathrm{room}} \leq 100\,\mathrm{mbar}$ with $960\,\mathrm{mbar} \leq p_{\mathrm{room}} \leq$

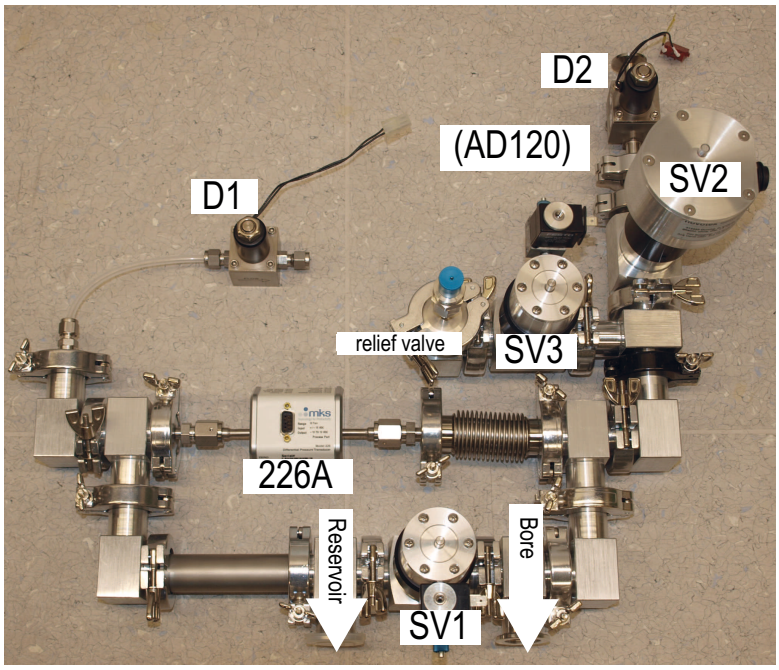

Figure 6.9: Photograph of the valve system of the current setup. Taken from [103].

990 mbar. As the pressure in the bore of the magnet is stabilized relative to the pressure of the APR, the stability of the complete system is limited by the stability of the pressure in the APR.

Safety Valve System

The stabilization system contains three safety valves (Fig. 6.9, SV1, SV2 and SV3) and an additional differential pressure transducer *226A* (*MKS Instruments*), which is installed between the tubes connected to the reservoir and the bore (see Fig. 6.8). In the case of an unexpected rise of pressure in the magnet, e. g. a quench or other events like filling helium, the differential pressure transducer *AD120 (MKS Instruments)* should be decoupled from the system to prevent it from damage. The safety valves are switched already at a low pressure increase of a few hundred µbar, whereas the safety valve system from the magnet itself (see Fig. A.3) reacts only at an overpressure above 200 mbar[2]. As the *AD120* is designed for max. 100 mbar overpressure we need to guarantee that the safety valves are switched at an early stage of a quench. For every helium filling one has to open SV1, which leads to a pressure equalization between the bore and the reservoir. However, the safety mode (switch SV1–3) allows one to fill without waiting for the complete equalization of the pressure in the bore and in the reservoir. After each helium refill it takes several hours until the system is back in the stabilized mode.

[2]The pressure in the magnet is about a few ten mbar above the environmental pressure, if the stabilization system is in operation.

Control of the Stabilization System

Initially the control of the pressure stabilization was realized by employing a commercial controller *(Type 250, MKS Instruments)*. At that stage the pressure regulation system was installed in a slightly modified version and the level stabilization was not implemented yet. Meanwhile, the complete stabilization system is controlled by one combined digitized system developed within the Master's thesis of A. Rischka [103]. This system is more flexible compared to the commercial controller and allows one to consider the coupling of the bore and the reservoir. For first tests two independent proportional-integral-derivative (PID) controllers are employed to address the dosing valves D1 and D2. The setting of PID regulation parameters as well as the data acquisition is realized by a microcontroller being implemented on a field-programmable gate array (FPGA) board. The pressure sensors (*AD120* and *226A*) are read out and supplied by the commercial device *PR4000B* (*MKS Instruments*), which can be connected via a serial interface to the FPGA board. The FPGA board is connected to the PENTATRAP control PC where a *LabVIEW*™ based program allows one to control the stabilization system. For more details see [103].
Assuming two independent PID controllers one has to ensure that the time constant of the pressure regulation system differs from the time constant of the level stabilization system, to minimize the influence of the systems to each other. For the future an elaborated regulation system will be implemented, which will take into account the coupling of the reservoir to the bore.

6.2.2 Commissioning of the Helium Pressure and Level Stabilization System

For the initial tests only the pressure stabilization was set up. The valve D1 was replaced by a blank plug and SV1 was open. In that configuration the pressure was stabilized to $\pm 3\,\mu$bar over 4 days. The same performance was achieved later on in a combined measurement, i. e., when the pressure and level stabilization system were both in operation.
In order to see how the regulation system reacts under stress, the commercial level sensor (see Fig. 6.7) was read out, which leads to an increase of the bore pressure by about $300\,\mu$bar. Depending on the settings of the regulation system, it lasts 2–3 minutes to stabilize the pressure after this kind of distortion.
Within the commissioning of the level stabilization [103] the frequency change was determined as a function of the helium level. According to that measurement the sensitivity is given as $1.0(0.2)\,\mu$m/Hz. The level stabilization system has been tested only for a very short time as shown in Fig. 6.10. The time constants of the level regulation and pressure regulation are not tuned yet. Thus, both systems influence each other, which leads to continuous level oscillations. Furthermore the sampling rate of the frequency, i. e. level measurement has to be increased. The sampling rate of the present setup is at 1 Hz. Level fluctuations with the present setup are below $\pm 40\,\mu$m. In summary, these test measurements represent a proof of principle. There are many issues which have to be addressed, when the PENTATRAP experiment is in operation and ions of a well-known mass can be used to determine the magnetic field stability by measuring the cyclotron frequency.

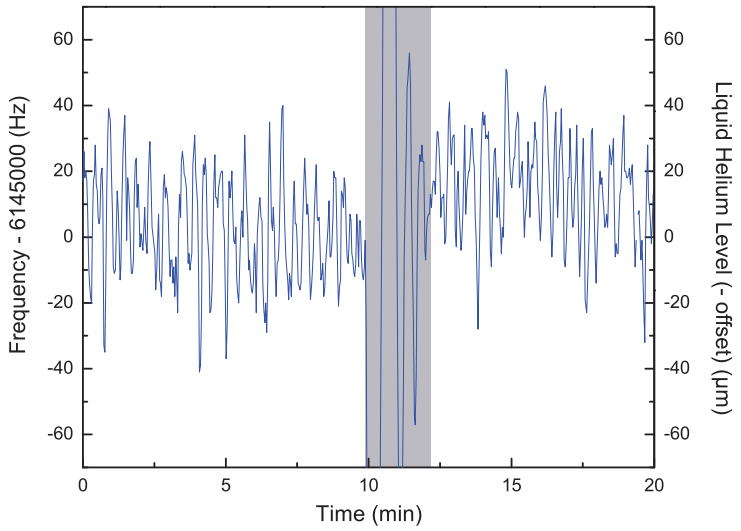

Figure 6.10: Stabilized helium level determined via the frequency measurement of the level resonator. Fluctuations of 1 Hz correspond to 1 µm level fluctuations. The gray marked region indicates a disturbance due to a level readout employing the commercial level sensor. With the current settings, both the pressure and level regulation system influence each other, which yields continuous level oscillations.

6.2.3 Outlook

A characterization of the helium pressure and level stabilization system will be possible, if the cyclotron frequency of ions of a well-known mass can be measured at PENTATRAP to determine the magnetic field stability on longer time scales. This measurement will allow one to determine the dependence of the cyclotron frequency on the pressure and level of the helium. So far, a proof of principle of the stabilization has been achieved, whereas the safety valve system still has to be tested and characterized.
If the complete system is installed and tested and an enhanced sensitivity of the pressure system stabilization is required, one can add a pressure transducer with a resolution of 100 nbar. As such a pressure transducer has a full scale range of only 10 mbar, the switching on of the stabilization system has to be done in a well-controlled manner. This can be realized by a pre-regulation employing the current setup and a modification of the APR, i. e. an additional connection tube has to be attached to the top flange of the APR.

Chapter 7

StaReP – an Ultra-Stable Voltage Source

PENTATRAP is aiming for high-precision mass measurements, i. e., relative uncertainties in the cyclotron frequency on a level of 10^{-11}. The cyclotron frequency will be obtained employing the invariance theorem (Eq. (2.15)) and thus the relative uncertainty is given as:

$$\frac{\Delta\omega_\mathrm{c}}{\omega_\mathrm{c}} = \left(\frac{\omega_+}{\omega_\mathrm{c}}\right)^2 \cdot \frac{\Delta\omega_+}{\omega_+} + \left(\frac{\omega_\mathrm{z}}{\omega_\mathrm{c}}\right)^2 \cdot \frac{\Delta\omega_\mathrm{z}}{\omega_\mathrm{z}} + \left(\frac{\omega_-}{\omega_\mathrm{c}}\right)^2 \cdot \frac{\Delta\omega_-}{\omega_-}. \tag{7.1}$$

As the uncertainty contribution of the axial frequency is suppressed with $(\frac{\omega_\mathrm{z}}{\omega_\mathrm{c}})^2$, the axial frequency has to be measured on a level of at least $2 \cdot 10^{-8}$ for typical frequencies at PENTATRAP (see Tab. 2.1). Due to the dependence of the axial frequency on the trapping voltage (Eq. (2.9)), the relative voltage stability should be below

$$\begin{aligned} \frac{\Delta U}{U} &= 2 \cdot \frac{\Delta\omega_\mathrm{z}}{\omega_\mathrm{z}} \\ &= 4 \cdot 10^{-8} \end{aligned} \tag{7.2}$$

within about 10 minutes, which is a typical duration of a measurement cycle. Hence, an ultra-stable voltage source is needed to supply the Penning-trap electrodes with stable potentials. The requirements are very demanding and no commercial source is available with these specifications. Therefore, an elaborated source called StaReP (**Sta**ble **Re**ference for **P**enning Trap Experiments) was developed in collaboration with the electronics workshop at MPIK and the Physikalisch-Technische Bundesanstalt (PTB), Braunschweig. In the present chapter the requirements on the voltage source, the main components of the setup as well as commissioning measurements of StaReP will be presented.

7.1 Requirements

PENTATRAP contains in total five Penning traps which consist of five electrodes each. Therefore a voltage source with 25 channels is required, which provides voltages in the

Table 7.1: Trapping voltages for several elements in different charge states.

Z	Ion	Voltage (V)
2	$^{4}He^{1+}$	−19.69
2	$^{4}He^{2+}$	−9.85
18	$^{40}Ar^{2+}$	−98.45
18	$^{40}Ar^{18+}$	−10.94
54	$^{132}Xe^{7+}$	−92.83
54	$^{132}Xe^{20+}$	−32.49
54	$^{132}Xe^{54+}$	−12.03
82	$^{208}Pb^{11+}$	−93.08
82	$^{208}Pb^{40+}$	−51.19
82	$^{208}Pb^{82+}$	−12.49

Table 7.2: Parameters of StaReP.

Parameter	Value
Number of channels	25
Voltage range	0 to −100 V
Stability	$\leq 4 \cdot 10^{-8} \cdot U_{\text{out}}$ within 10 min
Resolution	$\leq 1.5\,\mu V$
Stability (temperature)	$\leq 4 \cdot 10^{-7} \cdot U_{\text{out}}/K$
Ramping	(0–100 %) U_{out}
Control	*LabVIEW*™, USB

range of 0 to −100 V. The large voltage range allows one to trap ions with a wide q and m range at a fixed axial frequency as can be seen in Tab. 7.1. Moreover, low noise, i. e. $\leq 1\,nV/\sqrt{Hz}$ (cp. [116]), and a relative stability of $\leq 4 \cdot 10^{-8}$ within about 10 minutes is important to enable ion storage for high-precision mass measurements.
A high resolution of few µV is indispensable to tune the trapping potential properly. For the realization of the measurement scheme depicted in Fig. 6.5, a ramping option, which allows the transportation of ions from at least 3 traps to their adjacent traps, is compulsory. The StaReP control is implemented in the PENTATRAP control system. It is based on *LabVIEW*™, which allows one to run a whole measurement cycle automatically [106].
The PENTATRAP laboratory is temperature stabilized to better than 100 mK within 24 hours. Nevertheless, there are still temperature fluctuations within this range. The aim is to reach a temperature stability of StaReP of better than $4 \cdot 10^{-7} \cdot U_{\text{out}}/K$. A summary of the required specifications for the StaReP voltage source is given in Tab. 7.2.
There is no commercial solution available, which fulfills the mentioned requirements. So far the *UM 1-14* power supply from *Stahl-Electronics* [117] was employed. But its small voltage range of 0 to −14 Volt limits the range of the charge-to-mass ratio for measurements at the axial frequency, which is about 600 kHz in the PENTATRAP experiment. Furthermore, the *UM 1-14* contains only 3 independent precision channels.

Table 7.3: Different parts of StaReP with its functionality are summarized. For details see text.

Part	Functionality
StaReP transformer LV	supply mainboard and reference module
StaReP transformer HV	supply HV amplifier
Reference module	provide reference V_{ref} for precision and ramping DACs
DAC module: precision path	enable high resolution for precision mode
DAC module: ramping path	enable ion transport on few hundred ms time scale
HV amplifier	amplification by a factor of 10
StaReP controller	set voltage, monitor temperature and supply voltages

7.2 System Architecture

The unique architecture of StaReP includes different parts: the StaReP transformer in the power supply rack and the electronic rack comprising a reference module, a master module and 25 channels that are grouped in so-called 5-channel-modules, see Fig. 7.1. The modular architecture allows one to exchange either single channels or 5-channel-modules easily in the case of failure. The communication is implemented via SPI to the PENTATRAP control system. In the following the single components (see Tab. 7.3) and the overall setup of StaReP, which is depicted in Fig. 7.2, will be introduced in detail.

Transformer and Shielding Concept

In order to reach the required high stability of the voltage source it is important to be shielded from external distortions. Therefore, for the high-precision experiments PENTATRAP [38] and ALPHATRAP [118], being located next to each other, an own transformer station (so-called MPIK-transformer-station 2) is employed. The power from the MPIK-transformer-station 2 is guided to a power distribution cabinet, where a filter can be implemented. The filtered voltage provides the PENTATRAP laboratory, the ALPHATRAP laboratory and the StaReP transformer[1], which holds a LV transformer and a HV transformer (see Fig. 7.2, (2)). The LV transformer supplies the reference module and the mainboard including the digital-to-analog converter (DAC) module, whereas the HV transformer is required to power the HV amplifier. The transformers have been designed at MPIK according to a PTB application [119]. Both, the LV and HV transformer, are surrounded by a Mu-metal layer to prevent the stray field influence on the rectifier boards and secondly to minimize environmental disturbances. The inner core and the windings have been provided by *ELNA Transformatoren GmbH*. Different stages of the manufacturing process are shown in Fig. A.4. The voltages are rectified, filtered and preregulated before they are linked to the electronic rack. The StaReP shielding concept is displayed in Fig. 7.3. In order to reduce capacitive coupling between primary and secondary windings, copper shieldings (blue) are implemented separately for each channel. These shieldings are guided potential-free to the PENTATRAP experiment. The triax cable for the connection of StaReP with PENTATRAP was manufactured especially for the presented setup (see

[1] The StaReP transformer will be called transformer in the following.

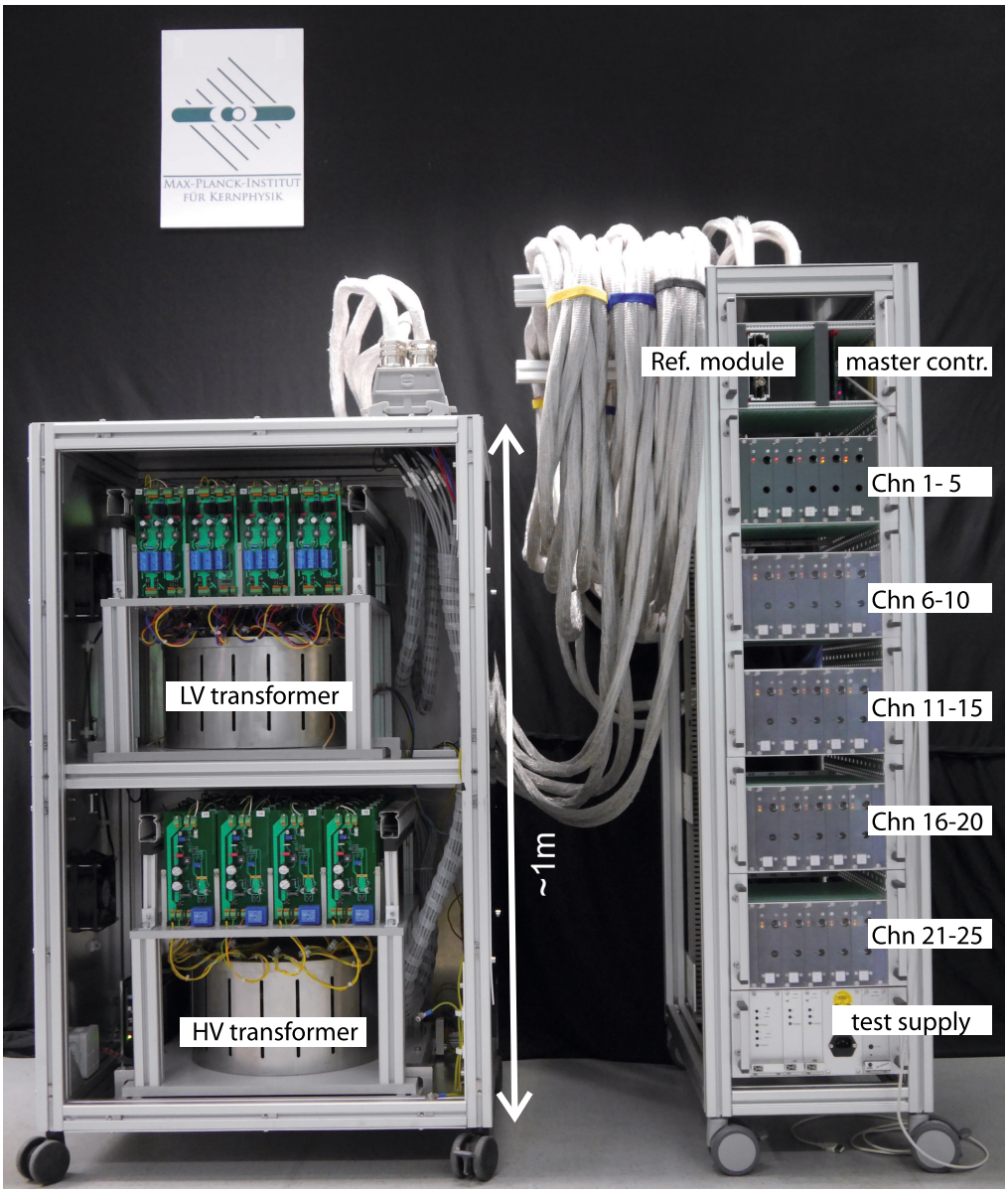

Figure 7.1: The StaReP voltage source consists of a power supply rack (left) and an electronic rack (right) comprising 25 channels, the master module and the reference module. The power supply rack will be placed in the hall in front of the laboratory, while the electronic rack will be located in the temperature stabilized PENTATRAP laboratory.

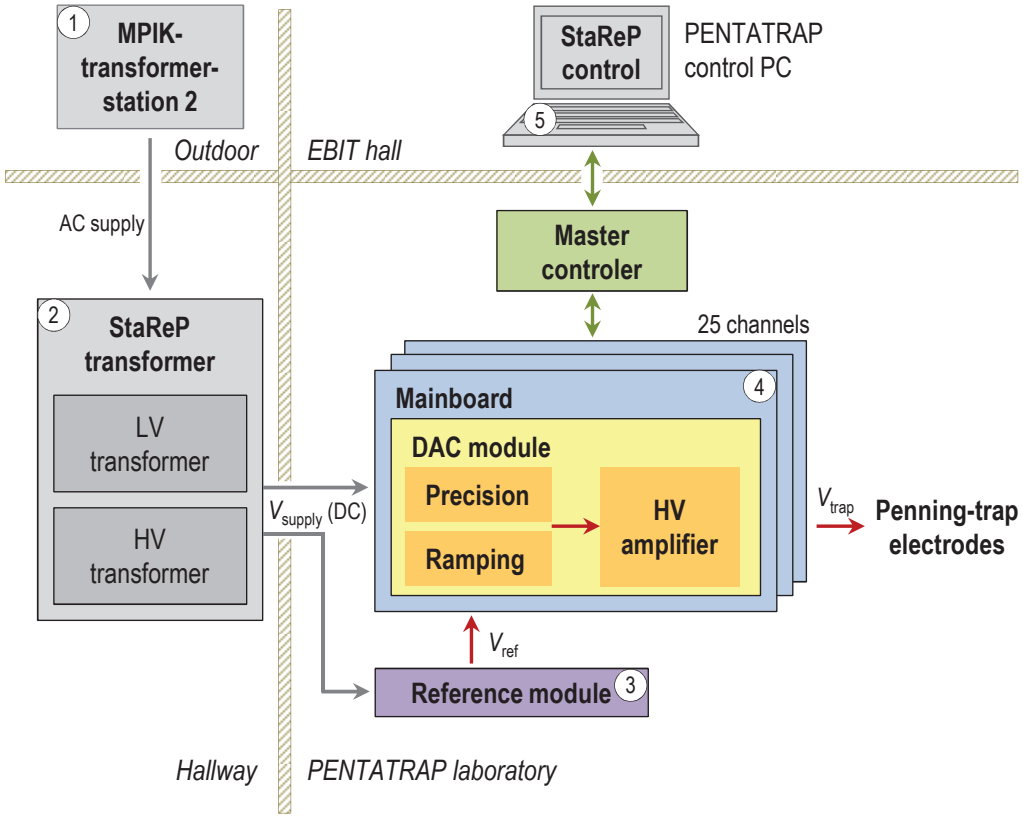

Figure 7.2: Schematic of StaReP. The MPIK-transformer-station 2 (1) supplies the StaReP transformer (2), which comprises a LV and HV transformer as well as rectifiers and voltage regulators. DC voltages are then guided to the reference module (3) and the 25 StaReP channels (4). The reference module provides the reference voltage for the precision and ramping DACs. The StaReP control is implemented in the PENTATRAP control system (5). For details see text.

photograph in Fig. 7.3). On the one hand, a small meshed shielding is provided and, on the other hand, the insulation part is made of teflon to facilitate the handling. The cable core has a diameter of only 0.5 mm, such that the cable can be connected to *Lemo* triax connectors.

The Reference Module

The reference module is supplied by the LV transformer and is placed in the electronic rack in the upper module (see Fig. 7.1) in the temperature stabilized PENTATRAP laboratory. It is embedded in a copper housing and surrounded by a 10 mm layer of styrofoam to reduce the influence of environmental temperature fluctuations. The reference module provides the reference voltage of +10 V for the coarse DAC, fine DAC and ramping DAC of the

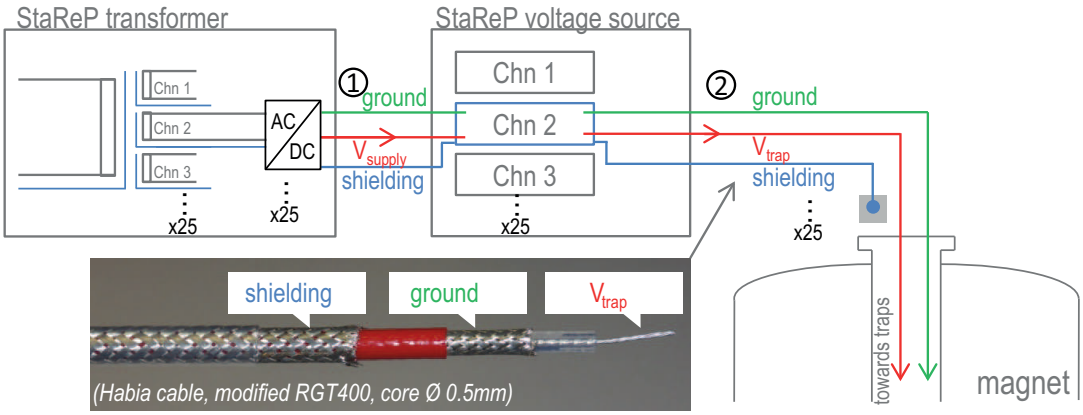

Figure 7.3: Schematic of the shielding concept. In order to minimize noise from the network as much as possible a special transformer has been designed. The capacitive coupling between the primary and secondary windings is reduced by means of copper shieldings (blue). For each of the 25 channels there is a three-core cable connecting the transformer with the StaReP source and a triax cable, which serves as connection between the StaReP source and the PENTATRAP setup. The three-core cable (1) contains the DC supply voltage (red), a ground potential (green) and a shielding potential (blue). The triax cable (2) contains the trapping voltage (red), i. e. a low noise, ultra-stable DC voltage, the ground (green) with respect to the Penning-trap voltages, and the shielding (blue). The trap and ground potential are guided to the Penning traps in the cryogenic region of the PENTATRAP setup, whereas the shielding will be connected at room temperature to a certain potential for each channel separately.

25 channels, which define the resolution of the voltage source. It comprises one or more[2] references (*VRE102A*). The employment of several references in parallel is advantageous since the statistical noise reduces with a factor of $1/\sqrt{N}$ with N being the number of references in use. In several tests the relative stability of V_{ref} has been demonstrated to be $\approx 2 \cdot 10^{-8}$ within a few minutes. This voltage was measured employing the *Fluke 8508A* [120] multimeter. The stability of V_{ref} limits the overall performance of StaReP. Another reference module employing 8 *AD587* references in parallel instead of 4 *VRE102A* references was set up and a similar performance was demonstrated.

25 Voltage Source Channels

Each channel contains low noise voltage regulators, a slave controller, a DAC module and an HV amplifier as shown in Fig. 7.4. The DAC module contains a precision and ramping path. For mass measurements, i. e. when a stable potential and a high resolution is required, the precision path is used. For the ion transfer from one trap to an adjacent trap, the voltage has to be dynamically varied. This so-called ramping mode is realized in the ramping path. The output voltage of the DAC module is in the range of 0 to +10 V. This voltage is then converted to 0 to −100 V by the HV amplifier.

[2]The final design and number of references is not decided yet.

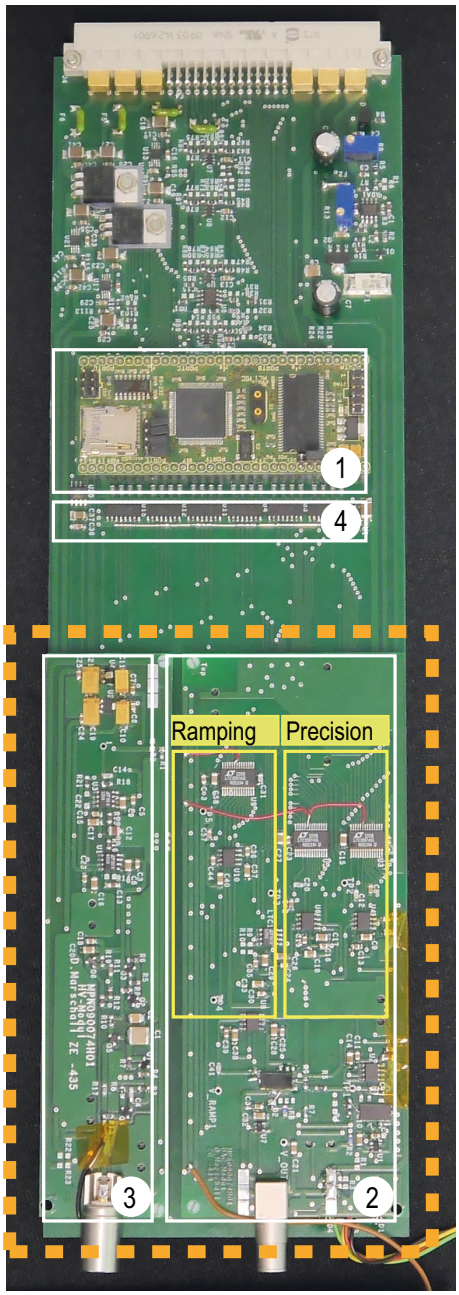

Figure 7.4: Photograph of one voltage channel comprising the slave controller (1), the DAC module (2) including precision and ramping paths as well as the HV amplifier (3). Optocouplers (4) ensure the separation of digital and analogue ground. The DAC module and the HV amplifier are embedded in a copper box (orange dashed line) surrounded by a styrofoam layer.

Table 7.4: Key components of StaReP are listed.

	Component	Manufacturer
Voltage reference	*VRE102A*	*Apex Microtechnology*
Both precision DACs (16 bit)	*LT1597*	*Linear Technology*
Ramping DAC (16 bit)	*LT1597*	*Linear Technology*
OP (precision and ramping path)	*OPA277A*	*Texas Instruments*
OPs (HV module)	*LT1250, LT6010*	*Linear Technology*
Resistors (in signal path)	*SMR3DZ*	*Vishay*

The resolution of the precision mode is defined by the DACs in the precision path. Two 16 bit DACs, the fine DAC and the coarse DAC, are in use. As shown in Fig. 7.5, the output signal of the fine DAC is weighted by a factor of 1/10000 compared to the output signal of the coarse DAC. The weighted sum of both DACs is theoretically tuneable in steps of 15 nV. Due to the amplifier behind the DACs the overall resolution would be 150 nV. In order to be able to correct for the differential nonlinearity of the coarse DAC, the weightage factor has been chosen such that the output range of the fine DAC is much larger then the step size of the coarse DAC. Although the output voltage range of the fine DAC has been chosen to be about 1 mV the step size is still well below the required resolution of $\leq 1.5\,\mu V$ without using the least significant bits of the fine DAC. Thus, the output voltage of the DAC module is not affected by the differential nonlinearity of the coarse or fine DAC. The design of the DAC module has been chosen in a way that commercial resistors were available and a high resolution can be achieved. Further combinations of resistors can be considered in future studies in case that an optimization is required. The ramping path is equipped with only one DAC as a lower resolution is sufficient to transport the ions to the adjacent traps.
The HV amplifier has been developed by S. Sturm (MPIK). It is based on a temperature compensated design using a combination of a zero-drift amplifier and a low noise amplifier. This setup eliminates temperature caused drifts in the output voltage due to drifting input bias voltages of the amplifiers.
The 25 channels are equipped with resistors (see Tab. 7.4) and other components being sensitive to the environmental temperature. These sensitive parts of the channels are spatially separated from other components producing a significant amount of heat. In addition they are embedded in a housing of copper surrounded by styrofoam.

The StaReP Control

The StaReP control is implemented in the PENTATRAP control system. The signals, i. e. voltages and trigger signals, from the PENTATRAP control system are sent via an USB-SPI-module to the master controller of the voltage source being placed in the upper housing of the electronics rack, see Fig. 7.1. The master controller communicates with the slave controllers, which are placed on each of the 25 channels. A schematic of the control system is depicted in Fig. 7.6. StaReP can be operated in two modes: ramping mode for adiabatic ion transport and sleeping (precision) mode for high-precision mass

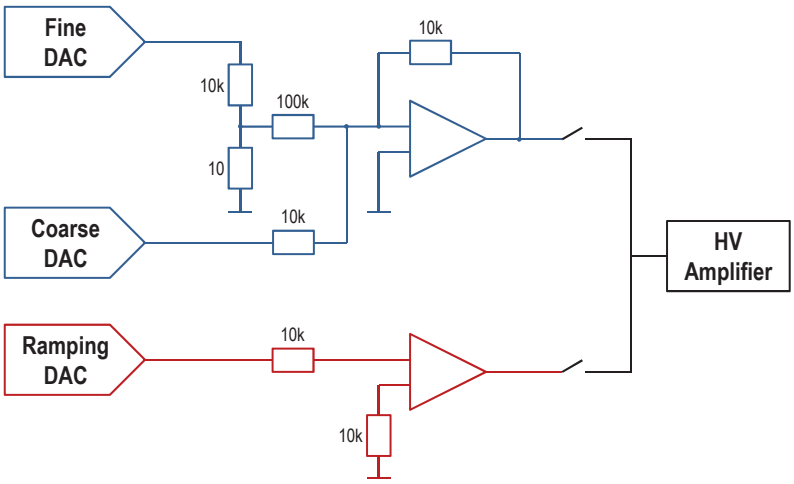

Figure 7.5: The precision (blue) and ramping (red) path are depicted. The precision path holds two 16 bit DACs. Overall the effective resolution of the combination of both DACs and the weightage resistors *(Vishay)* is about 26 bit which corresponds to $\leq$1.5 µV. In order to switch between the precision and the ramping mode two relais are implemented between the DAC module and the HV amplifier. For the ion transport a reduced resolution is required, thus one 16 bit DAC is sufficient in the ramping path.

measurements. Note the slight difference between precision mode and sleeping mode: The precision mode means that the precision path (allowing high resolution) is used. In the sleeping mode the precision path is employed as well, but in addition the clock of the slave controller is switched off. In the ramping mode the number of steps as well as the voltage step size is variable. Each ramping step takes at minimum 8 µs and a complete adiabatic ion transport from one trap to the adjacent trap is possible within a few 100 ms. It is important to keep this time as short as possible to reduce the influence of magnetic field fluctuations. A test version of the user interface is shown in Fig. 7.7.

For monitoring reasons the control system allows to read out temperatures on the main-

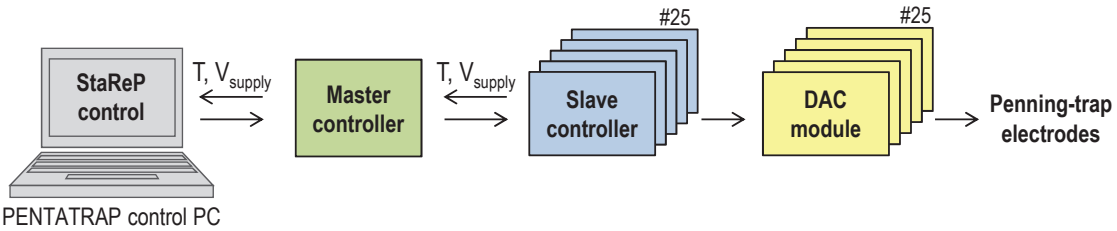

Figure 7.6: The PENTATRAP control system includes the StaReP control. Signals are first sent to the master controller, which distributes the settings to the 25 slave controllers. The signals are then set to the DACs in the ramping or precision path, depending on the operation mode. For precision measurements a sleeping mode was implemented. This allows one to stop any activity of the slave controllers.

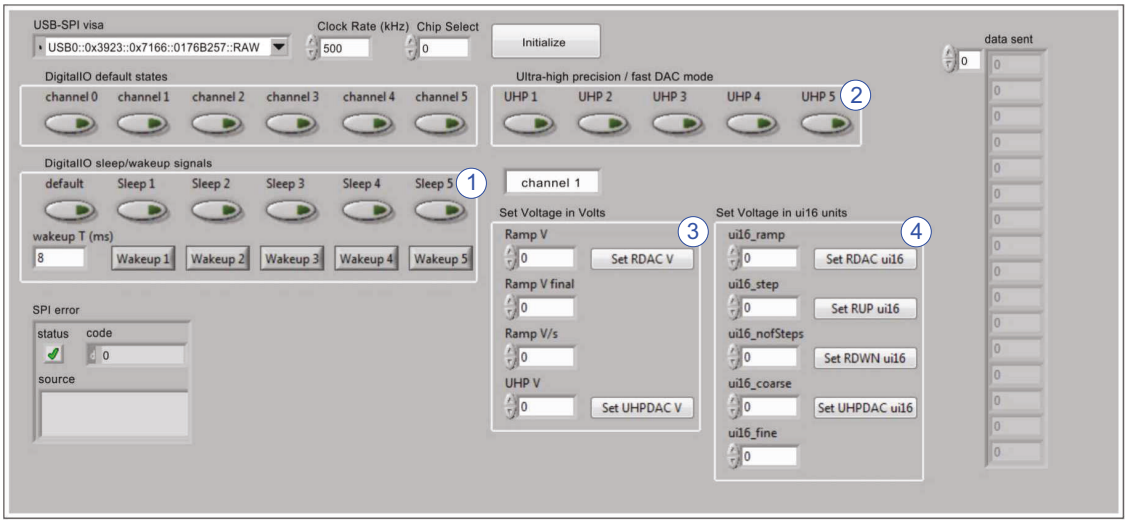

Figure 7.7: Test control system of StaReP. The *LabVIEW*™ based user interface allows to set the sleeping mode (1), the precision or ramping mode (2) and the voltage, either in Volts (3) or as a bit combination of the DACs (4). Moreover, the ramping speed can be controlled.

boards as well as a readout of the supply voltages for the mainboard in order to check whether they are set properly. This facilitates troubleshooting in the case of failure. Additional to the StaReP control via the control system of PENTATRAP, the readout of temperature and supply voltages on the mainboard can also be requested and shown by a keypad and display placed in the upper module of the electronic rack.

7.3 Characterization of StaReP

Several measurements have been performed to characterize the voltage source. Note, that some tests have been performed with the first version of StaReP called Rev.0 and others with the second version called Rev.1. The main difference between Rev.0 and Rev.1 are different layout versions of the mainboard. Rev.1 is designed such that components with a high power dissipation are spatially separated from temperature sensitive components. All sensitive components are placed in a copper box, which is located in a styrofoam housing. Furthermore, connectors and voltage regulators on the mainboard have been exchanged. A test power supply is used to power Rev.0 channels, while the StaReP transformer provides the supply voltages for Rev.1 channels.

In the following 4 examples will be discussed. As we are interested in the temporal stability of the voltage source, the overlapping Allan deviation[3] is shown for all test measurements. These so-called $\sigma-\tau$ plots indicate the relative voltage stability for different time intervals. The error bars indicated in the $\sigma-\tau$ plots represent the statistical uncertainty. For more

[3]We employed the program AlaVAR 5.2 [121] to calculate the overlapping Allan deviation.

details the reader is referred to [121, 122].
Due to the high stability and low noise of the output voltage of StaReP, it is challenging to measure the voltage with a multimeter, because there are no commercial devices available with low enough background noise. The test setup was equipped with a *Fluke 8508A* multimeter [120], which is limited in the resolution by 8.5 digits with a sampling interval of 26 seconds. Thus, it is not possible to determine the stability of the voltage on shorter time scales. Moreover, the internal drift of the multimeter is $> 100\,\mu V$ per day at 100 V. A better, i. e. more sensitive test can be performed using Penning-trap experiments as the axial frequency of an ion, which is linked to the voltage via Eq. (2.9), can be measured more precisely. Therefore, tests at the *g*-factor experiment at the University of Mainz [123] and at the THe-Trap experiment at MPIK [111] have been performed.

7.3.1 Test Measurements in the PENTATRAP Laboratory

In general the measurements have shown that several hours warmup time after switching on the voltage source is needed. Then StaReP reaches its operating temperature and a strong drift which is visible in the warming up period disappears.
Rev.0 channels have been tested in the PENTATRAP laboratory without employing the transformer. Two examples are shown in Fig. 7.8 and Fig. 7.9 for $-48\,V$ and $-30\,V$ output voltages, respectively. A relative stability of few 10^{-8} could be demonstrated for both voltages in the precision mode within about 10 minutes time interval. A drift of few tens µV per day is observed.

7.3.2 Test Measurements with Ions at $-7.5\,V$ and $-89\,V$

One of the 5-channel modules of Rev.0 has been tested in the precision mode at the *g*-factor experiment [123] at the University of Mainz. A single highly charged $^{40}Ca^{17+}$ ion was trapped and the axial frequency was measured over several hours. Measurements at the *g*-factor experiment are advantageous, since it allows to determine the voltage stability on short time scales. Moreover, the determination of the voltage stability via frequency measurements in a Penning trap provides a higher resolution compared to a commercial multimeter. The axial frequency stability is shown in a $\sigma - \tau$ plot in Fig. 7.10. The ring voltage was set to $-7.5\,V$. Note, that the stability of the axial frequency is shown. To obtain the stability of the voltage, this value has to be multiplied by a factor of 2.
Two Rev.0 channels were tested in the precision mode at the THe-Trap [111] experiment. A $^{12}C^{4+}$ ion was trapped and the axial frequency was measured over several hours. This frequency was then converted to the ring voltage. The voltage stability is shown in Fig. 7.11. The relative voltage stability of $\leq 2 \cdot 10^{-8}$ was achieved at $-89\,V$.
Although both tests with ions were performed with Rev.0 channels, a direct comparison is not possible as different reference modules were in operation.

7.3.3 Thermal Characteristic

Two of the Rev.0 channels were tested with regard to the thermal characteristic. For this purpose a climate chamber was employed. The temperature was varied between

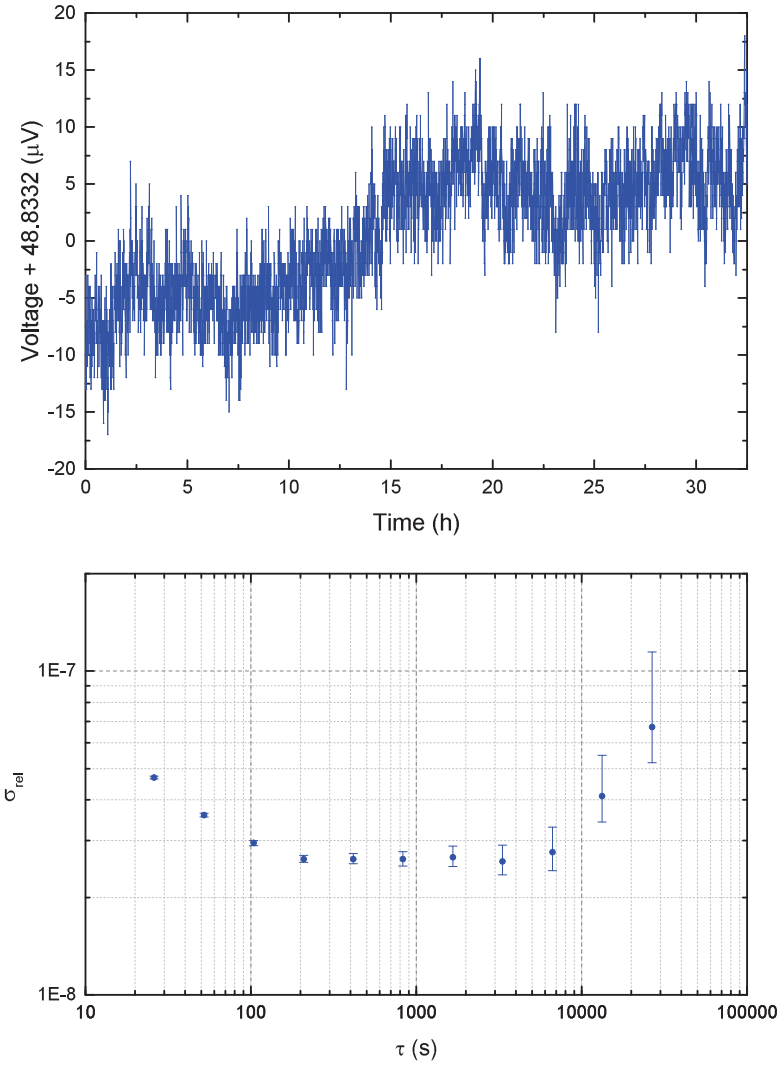

Figure 7.8: A Rev.0 channel was tested at $-48\,\mathrm{V}$ in the precision mode in the PENTATRAP laboratory. The voltage data (top) are shown and the relative Allan deviation, i. e. the relative voltage stability (bottom) was determined to be $\leq 3 \cdot 10^{-8}$ for time intervals of 10 minutes.

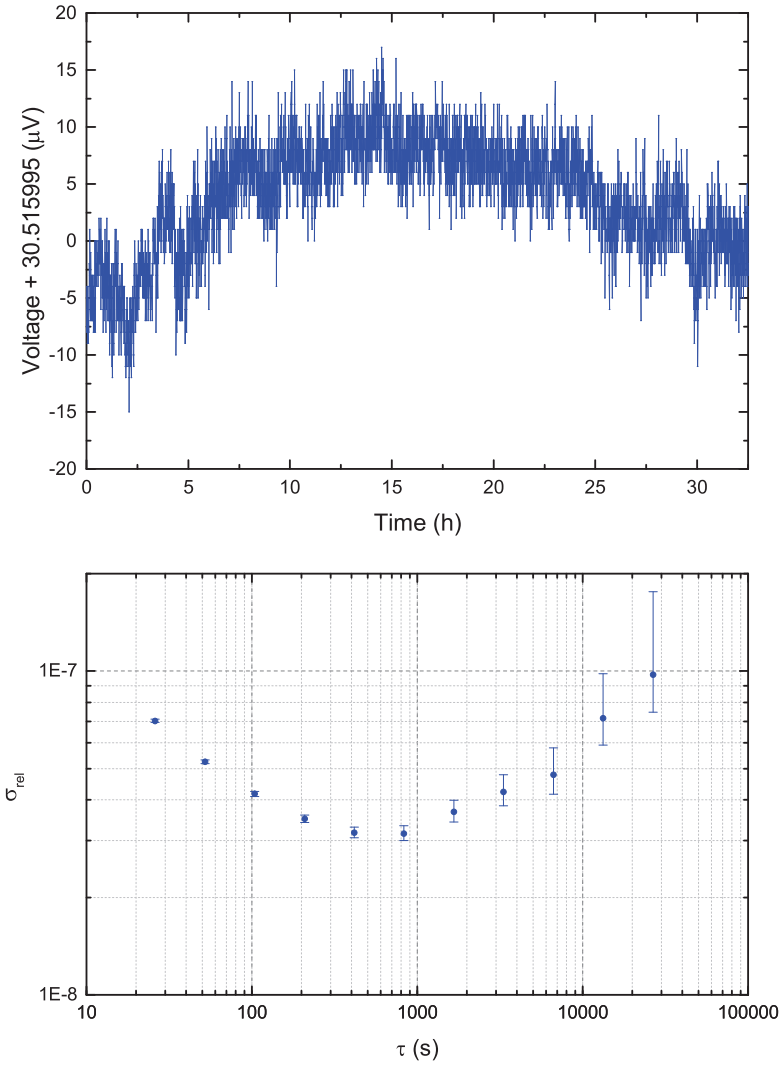

Figure 7.9: A Rev.0 channel in the precision mode at $-30\,\mathrm{V}$ was tested in the PENTATRAP laboratory at MPIK. The voltage data (top) are shown and the relative Allan deviation, i. e. the relative voltage stability (bottom) of $\leq 4 \cdot 10^{-8}$ has been obtained for time intervals of about 10 minutes.

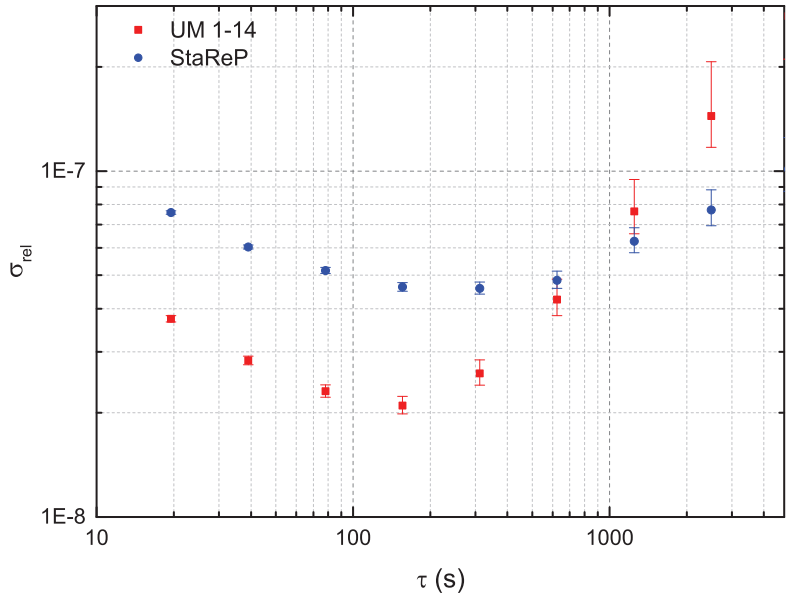

Figure 7.10: Relative Allan deviation of the axial frequency. The measurement was performed at the g-factor experiment in Mainz [123] at $-7.5\,\mathrm{V}$ ring voltage of the StaReP voltage source (blue). The measurement has been repeated employing the *UM 1-14* voltage source (red). On time scales above 800 s the performance of StaReP is more stable, but at time intervals of 100 s a factor of 3 less stable.

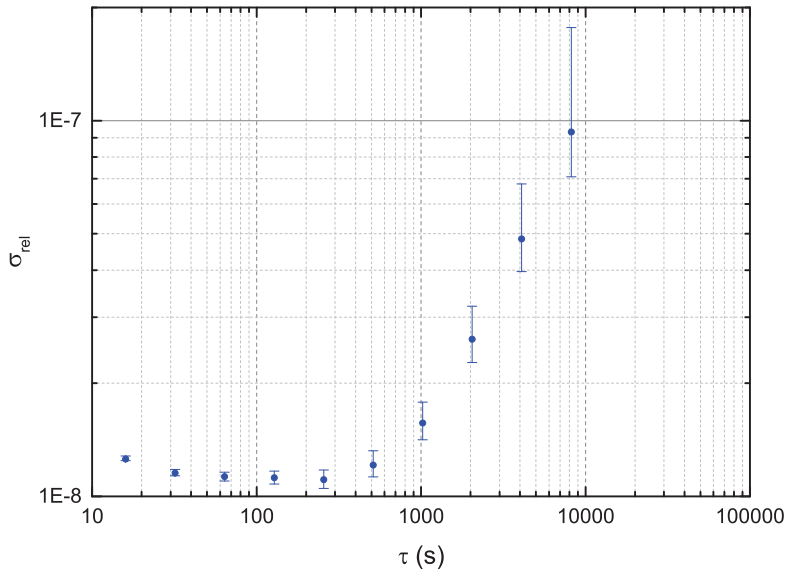

Figure 7.11: Relative voltage stability of a measurement with a Rev.0 channel of StaReP at the THe-Trap experiment. The ring voltage was determined by a measurement of the axial frequency. The relative stability of the ring voltage of $\leq 2 \cdot 10^{-8}$ within 10 minutes could be demonstrated at $-89\,\mathrm{V}$.

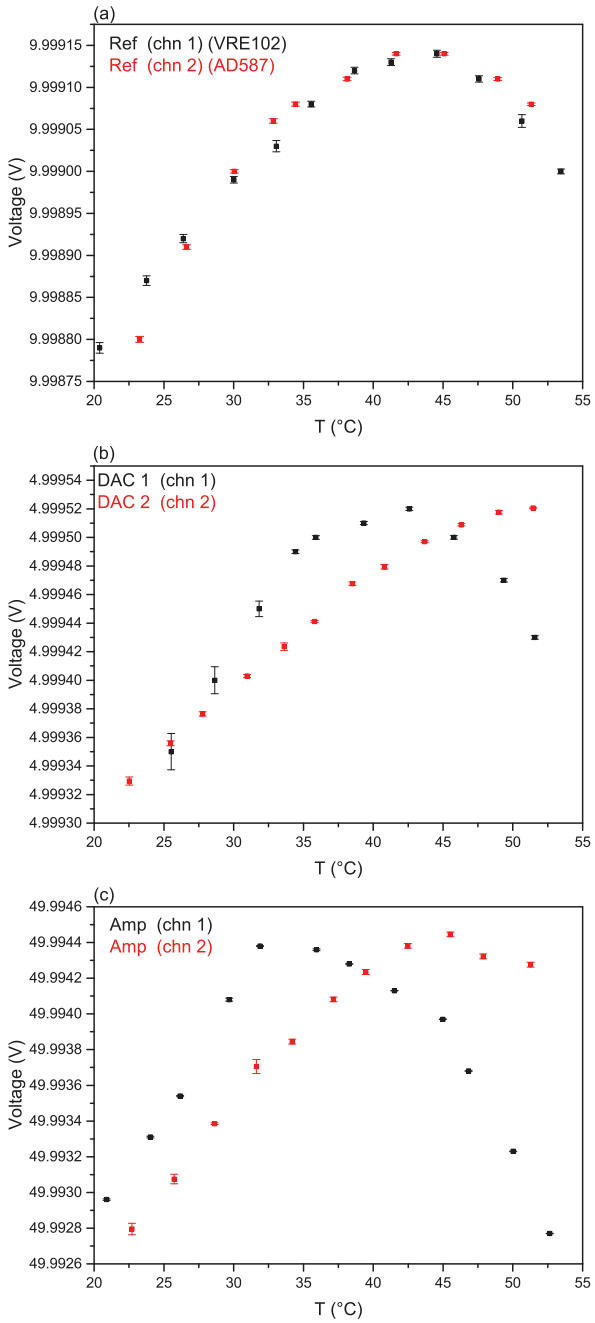

Figure 7.12: Thermal characteristic of single modules of the Rev.0 channels. Data are shown for (a) two reference modules (red: *AD587* and black: *VRE102A*), (b) two DAC modules (red and black identical in construction) and (c) two HV amplifiers (red and black identical in construction). Although both DAC modules and both amplifiers were identical in construction, the maxima of the parabolas are at different temperatures separated by about 10°C. The measurement time was not constant at all temperature steps. Error bars represent the statistical uncertainty.

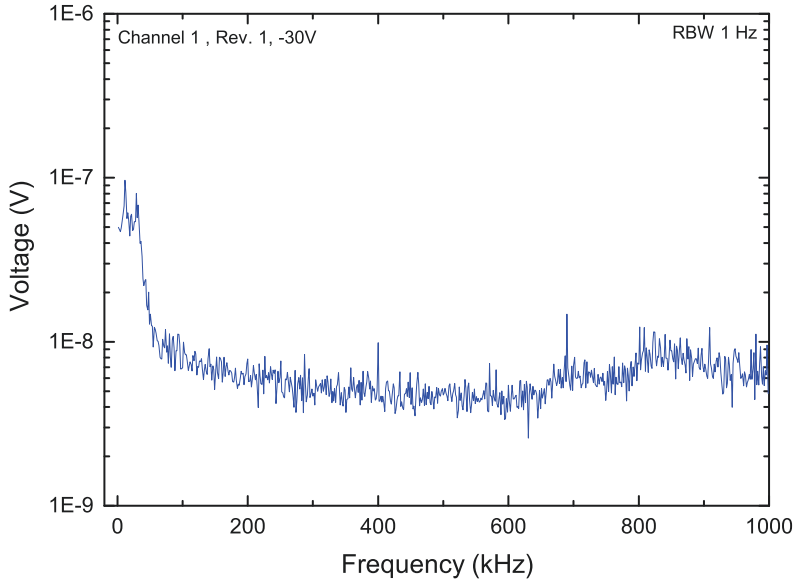

Figure 7.13: Noise spectrum of the output voltage of channel 1 (Rev.1). The noise in the low frequency range originates in the supply voltages for the HV amplifier. The increased noise around 800 kHz depends on the shielding system and can be reduced by modifying the shielding potentials.

20°C and 55°C. The thermal characteristic of both channels (black and red) exhibits a parabolic shape as shown in Fig. 7.12. Channel 1 (red) was equipped with a reference module employing 8 *AD587* references and channel 2 (black) was using one *VRE102A* reference. This measurement has shown that the ideal operating temperature of Rev.0 channels is above 40°C. As the lowest temperature coefficient of the reference module is expected at about 42°C (see Fig. 7.12 (a)), an active temperature stabilization could be employed to define the operating temperature of the reference module. In order to protect the components on the mainboard from damage, the Rev.1 channels are embedded in a copper housing and a styrofoam layer was added so that the sensitive components are now in a 30°C environment. The measurements which have been performed for Rev.0 channels will be repeated for the Rev.1 version such that the ideal temperatures of the single modules can be determined.

7.3.4 Noise Characteristic

An example of a noise spectrum recorded with the *R&S-FSV7* spectrum analyzer *(Rohde & Schwarz)* with an input resistance of 50Ω is shown in Fig. 7.13. It shows a noise spectrum of channel 1 (Rev.1) at −30 V. The noise at low frequencies can be reduced by improving the supply voltages of the HV amplifier, whereas the noise around 800 kHz can be influenced by modifications of the shielding potential. Taking into account the baseline, a noise voltage density of $\leq 2\,\mathrm{nV}/\sqrt{\mathrm{Hz}}$ at 600 kHz has been determined. Note, that there are no additional filters implemented at the output stage of the voltage source.

However, the PENTATRAP setup will be equipped with room temperature and cryogenic filter stages. Noise measurements of the output voltage including the room temperature filters of PENTATRAP are currently in progress.

7.3.5 Summary

So far, two 5-channel versions (Rev.0 and Rev.1) of StaReP have been set up and characterized. A proof of principle was shown, i. e. the complete system including the StaReP transformer was setup and commissioned. Most of the requirements (see Tab. 7.2) are fulfilled as outlined in the following.

- The required voltage range of 0 to $-100\,\mathrm{V}$ is accessible and controllable by a test version of the control system. The control system will be extended to the final version, when StaReP is connected to the PENTATRAP setup.

- The temperature characteristic has been studied for Rev.0 channels. For certain operating temperatures the required temperature stability has been achieved. For the final design of the channels, i. e. for Rev.1 channels, such a temperature characterization still has to be performed. In case it will be necessary the operating temperature of certain modules can be adjusted by an active temperature stabilization. In general, the temperature coefficient is expected to be lower in the Rev.1 version compared to the Rev.0 channels as the layout has been optimized considering the heat dissipation of several components.

- A resolution of a few µV has been achieved. Although the precision path of the DAC module provides theoretically a resolution well below $1.5\,\mu\mathrm{V}$, the limiting component is currently the reference module. An optimization of the reference module regarding the noise is required to achieve a resolution of $\leq 1.5\,\mu\mathrm{V}$. One possibility to reduce the statistical noise is to employ several voltage references in parallel. Apart from that different voltage references are currently in a test phase.

- The ramping option is available and controllable for all channels. So far, this operation mode has not been tested at a Penning-trap experiment.

- A relative voltage stability of $2 \cdot 10^{-8}$ within 10 minutes has been achieved for voltages in the range of $-30\,\mathrm{V}$ to $-90\,\mathrm{V}$. For voltages $> -10\,\mathrm{V}$ tests are in progress. A relative stability of $4 \cdot 10^{-7}$ within 10 minutes has been achieved at $-7.5\,\mathrm{V}$. Rev.0 channels and Rev.1 channels provide similar stabilities.

For all tests, which were performed without Penning-trap experiments, one has to be aware that the *Fluke 8508A* multimeter is limiting the sensitivity of the test facility. In

order to improve the tests, Penning-trap experiments are needed to determine the voltage stability via the axial frequency. As soon as PENTATRAP is ready to trap ions again the StaReP voltage source will be connected to the PENTATRAP trap tower enabling tests in different voltage ranges in the precision mode and in the ramping mode.

Chapter 8

Summary and Outlook

In the projects of this thesis two different Penning-trap experiments have been involved. On the one hand high-precision mass measurements of several nuclides in the thallium region were performed with the mass spectrometer ISOLTRAP at ISOLDE/CERN being the pioneering Penning-trap experiment at an online facility. The new mass values were used to study nuclear structure by comparing differences of binding energies to mean-square charge radii along the isotopic chains. On the other hand, important contributions to the new and unique setup of the five-trap mass spectrometer PENTATRAP at MPIK have been made. An ultra-stable voltage source was developed in collaboration with the electronics workshop at MPIK and the PTB Braunschweig. Moreover, the helium and pressure stabilization system for the PENTATRAP magnet was designed and is already partly implemented. According to the structure of this thesis, the concluding remarks on the mass results will be first discussed and the contribution to the PENTATRAP experiment will then be summarized.

Nuclear Structure Studies on Thallium Isotopes

In different experimental campaigns seven masses in the thallium region, namely ^{194}Au, ^{194}Hg, ^{190,193,198}Tl and ^{202,208}Pb, have been measured with a relative uncertainty reaching $\delta m/m \approx 2 \cdot 10^{-8}$. The measured masses have been published [1, 84] and most of them contribute significantly to the mass values published in the AME2012 [58].
The nuclear structure of the thallium isotopic chain, lying between the proton-magic lead isotopes and the deformed mercury and gold chains, has been investigated. Comparing ground-state properties of Tl, i. e. the two-neutron separation energy to differences in mean-square nuclear charge radii, a smooth behavior being characteristic for spherical nuclides was found. Moreover, microscopic calculations of the three-point-pairing gap assuming a spherical ground state agree well with the experimental results. Another indicator being sensitive for deformation is the five-point-empirical pairing gap, which was compared to differences in mean-square nuclear charge radii. In the thallium isotopes no sign of deformation was visible. In addition, the slope of the five-point-indicator was compared to the strength of staggering in the two-neutron separation energy, which reveals a symmetric pattern for lead and thallium isotopes. In the gold chain, where deformation

is existing, an asymmetric pattern became visible. In order to confirm the observation of the symmetric/antisymmetric pattern for spherical/deformed nuclides, further studies are required. The comparison of the strength of staggering in the two-neutron separation energy to the slope of the five-point empirical pairing gap has to be performed for further regions of the nuclear chart. Furthermore, one has to consider mean-square nuclear charge radii, which reveal to what extent a nucleus is deformed. If the antisymmetric patterns are in coincidence, i. e. at the same neutron numbers at which one can see clear deformation in the mean-square charge radii, this would strengthen our assumption. If the connection of symmetric or antisymmetric patterns for spherical or deformed isotopic chains can be confirmed, this comparison allows to get information on deformation effects from precise mass measurements.
Considering the first isomeric excitation energies in the even-N thallium isotopes one can find a parabola with a minimum around mid-shell, which indicates the presence of collective effects in the thallium ground states. Since the excitation energy never goes down to zero it supports the picture of a spherical nucleus. However, the spherical shell model is oversimplified for this case [86] and cannot describe this behavior properly. Further studies are needed to clarify the role of Tl, i. e. to what extent collectivity is present in thallium isotopes.
More studies in this region of the nuclear chart are in progress. The nuclear structure of the isotopic chains of neutron-deficient gold and astatine of ground and isomeric states were investigated by Penning trap mass spectrometry at the ISOLTRAP experiment. These isotopes were also studied by in-source laser spectroscopy determining differences of mean-square nuclear charge radii via the measurement of the isotopic shift [124]. Furthermore, after its installation in 2010, the multi-reflection time-of-flight mass separator was successfully used for fast beam purification especially helpful in the case of very short-lived species [125]. The device can also be used as a mass spectrometer, which allowed the mass determination of the neutron-rich ^{53,54}Ca isotopes. The masses confirmed a prominent shell closure at neutron number N=32 and corroborated the importance of three-nucleon forces in modern nuclear theory to properly describe structural evolution [126].
After the long shutdown of ISOLDE in 2012/2013, which was used to refurbish the ISOLTRAP setup, the first online experiment was dedicated to mass measurements of neutron-rich Cd isotopes. The masses of $^{129-131}$Cd contribute to the field of nuclear astrophysics addressing the question of how the heavy elements were created [127].

Contributions to the PENTATRAP Experiment

The aim of the PENTATRAP experiment [38] is to perform mass-ratio measurements of long-lived and stable highly-charged ions with a relative uncertainty of $\leq 10^{-11}$. This will allow one to contribute to the field of neutrino physics, to carry out stringent tests of QED and to test Einstein's relation $E = mc^2$.
The multi-Penning-trap experiment has been developed and setup within the last few years at MPIK. Meanwhile, in the first phase of commissioning ions were trapped successfully [106] and a lot of information for improvements on the setup were obtained. However, due to vacuum problems, an enhanced setup was designed and constructed. The modi-

fied setup is dedicated to reach a better vacuum in the Penning traps by implementing amongst others a pre-vacuum chamber. Moreover, the new design is setup in a modular way and the implementation is planned within the next few months. The first mass measurements are intended on ^{187}Re and its daughter nucleus ^{187}Os, which will be provided by the Dresden-EBIT3, to determine the Q-value being relevant for neutrino physics [128]. In order to achieve the high precision in the mass measurements a huge effort has been invested to stabilize the electric potential and the magnetic field of the Penning traps. Considering the stabilization of the magnetic field, a helium pressure and level stabilization system was adapted from the THe-Trap [111] experiment within the framework of this thesis. We are aiming for a pressure and level stability of about $1-2\,\mu$bar and 0.1 mm, respectively, over a period of about 10 minutes, which is a typical duration of a cyclotron frequency measurement [113]. This is required to obtain a constant temperature and thus a stable magnetic field as there are materials installed with temperature-dependent susceptibilities. The stabilization system was partly setup and tested. Further developments were conducted within the Master's thesis of A. Rischka [103]. In 2014, a proof of principle of the stabilization system has demonstrated a level stability of $\pm 40\,\mu$m and a pressure stabilization of $\pm 3\,\mu$bar relative to the pressure in the absolute pressure reference. However, this was a test on very short time scales. In order to better characterize the system a long-term measurement of the magnetic-field stability has to be carried out by measuring the cyclotron frequency of an ion with a well-known mass. So far, this test was not performed as the stabilization system was not implemented when ions were trapped. If it turns out that the characterization of the stabilization system with ions is limited by the sensitivity, a second pressure sensor with a higher resolution will be added. This upgrade is possible without extensive modifications of the present setup.
The central part of the PENTATRAP experiment is a stack of five cylindrical cryogenic Penning traps containing five electrodes each. In order to provide a stable potential in the Penning traps, an ultra-stable voltage source is required to supply the voltages for each of the 25 Penning-trap electrodes. As there is no commercial device available, which fulfills all requirements, an elaborated source, called StaReP (**Sta**ble **Re**ference for **P**enning Trap Experiments) was developed in the course of this dissertation in collaboration with the electronics workshop at MPIK and the PTB Braunschweig. The voltage source is one of the key components for the PENTATRAP experiment. It allows the storage of ions of a wide q/m range due to its large voltage range of 0 to $-100\,$V with a relative voltage stability of $\leq 4 \cdot 10^{-8}$ over a period of 10 minutes. Currently, two 5−channel versions, namely Rev.0 and Rev.1, of StaReP have been set up with slightly different layouts and components. Parts of the voltage source have been commissioned at existing Penning-trap experiments, namely the g-factor experiment at Mainz University [123] and THe-Trap [111] at MPIK, where the axial frequency of a trapped ion was measured to deduce the stability of the ring voltage. The precision channels of Rev.0 were tested at THe-Trap and a relative stability of $2{\cdot}10^{-8}$ at $-89\,$V has been demonstrated. Currently channels of Rev.1 are studied with regard to the temporal stability and the noise performance. Furthermore, the reference module, being one of the most important parts of the voltage source, might be improved by adding more references. Furthermore, the implementation of an actively temperature stabilized housing for the reference module would

be a possibility to set the operation temperature of the reference module in a range of a low temperature coefficient. As a next step the 25 channels will be manufactured. In the future further Penning-trap experiments, e. g. THe-Trap [111] and ALPHATRAP [118], will be equipped with some slightly modified channels of this unique voltage source.

Appendix A

Technical Drawings and Photographs

Photographs and drawings of parts of the helium pressure and level stabilization as well as the LV StaReP transformer are shown.

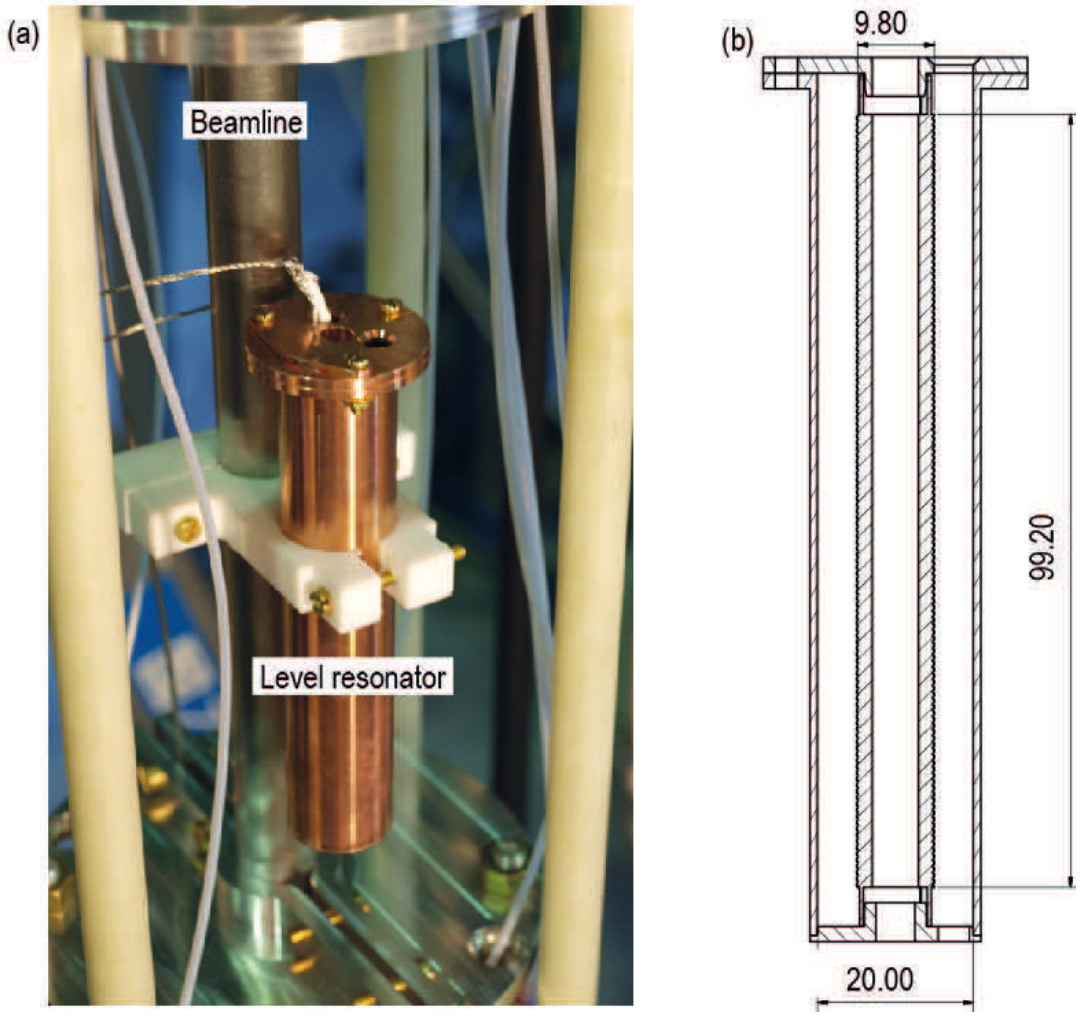

Figure A.1: Photograph (a) of the level resonator for the helium level stabilization. It is mounted at the beamline with a holder, which is designed such that the hight can be adjusted. The drawing (b) shows the dimension of the resonator in mm. Taken from [103].

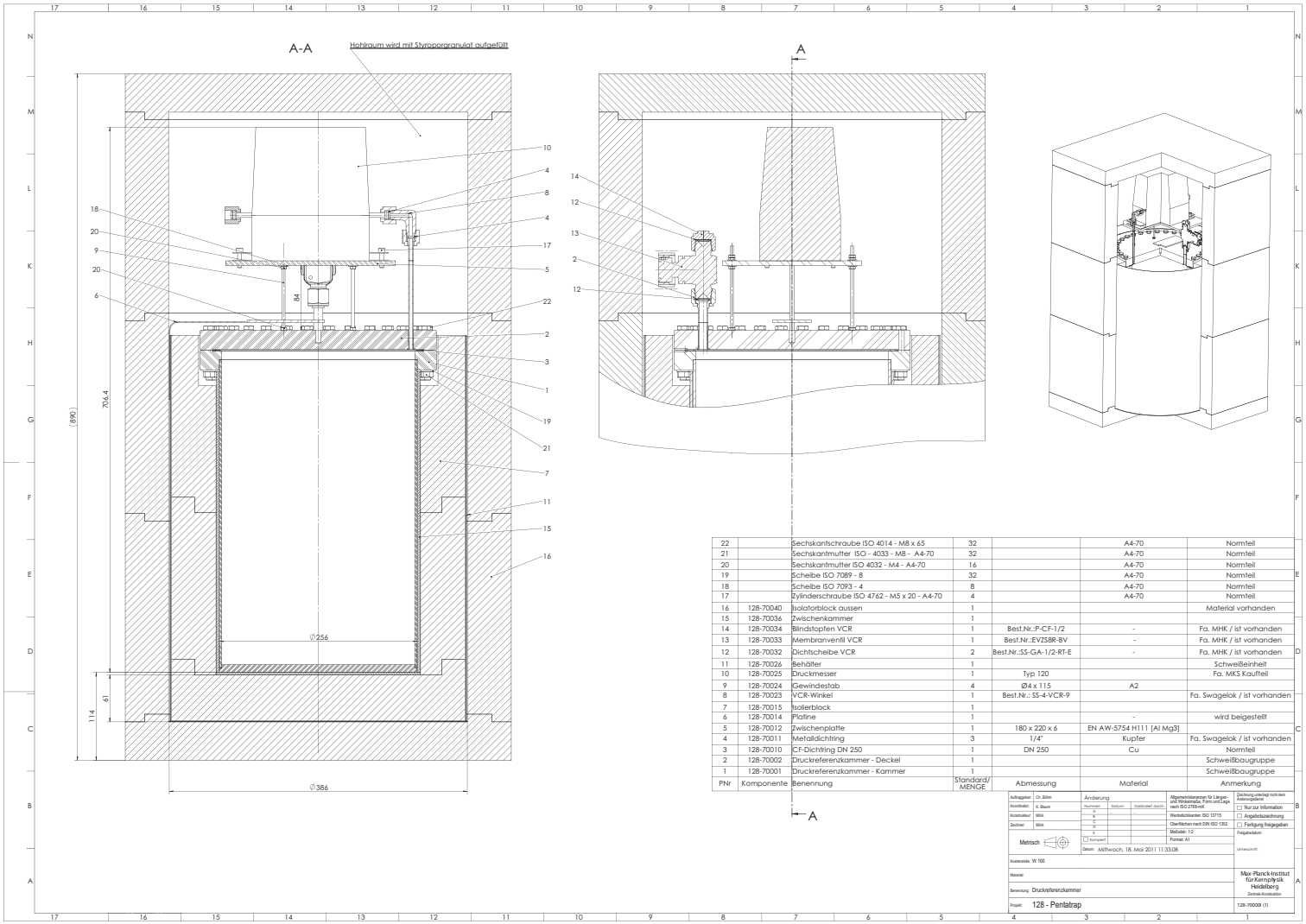

PNr	Komponente	Benennung	Standard/ MENGE	Abmessung	Material	Anmerkung
22		Sechskantschraube ISO 4014 - M8 x 65	32		A4-70	Normteil
21		Sechskantmutter ISO - 4033 - M8 - A4-70	32		A4-70	Normteil
20		Sechskantmutter ISO 4032 - M4 - A4-70	16		A4-70	Normteil
19		Scheibe ISO 7089 - 8	32		A4-70	Normteil
18		Scheibe ISO 7093 - 4	8		A4-70	Normteil
17		Zylinderschraube ISO 4762 - M5 x 20 - A4-70	4		A4-70	Normteil
16	128-70040	Isolatorblock aussen	1			Material vorhanden
15	128-70036	Zwischenkammer	1			
14	128-70034	Blindstopfen VCR	1	Best.Nr.:P-CF-1/2	-	Fa. MHK / ist vorhanden
13	128-70033	Membranventil VCR	1	Best.Nr.:EVZS8R-BV	-	Fa. MHK / ist vorhanden
12	128-70032	Dichtscheibe VCR	2	Best.Nr.:SS-GA-1/2-RT-E	-	Fa. MHK / ist vorhanden
11	128-70026	Behälter	1			Schweißeinheit
10	128-70025	Druckmesser	1	Typ 120		Fa. MKS Kaufteil
9	128-70024	Gewindestab	4	Ø4 x 115	A2	
8	128-70023	VCR-Winkel	1	Best.Nr.: SS-4-VCR-9		Fa. Swagelok / ist vorhanden
7	128-70015	Isolierblock	1			
6	128-70014	Platine	1		-	wird beigestellt
5	128-70012	Zwischenplatte	1	180 x 220 x 6	EN AW-5754 H111 [Al Mg3]	
4	128-70011	Metalldichtring	3	1/4"	Kupfer	Fa. Swagelok / ist vorhanden
3	128-70010	CF-Dichtring DN 250	1	DN 250	Cu	Normteil
2	128-70002	Druckreferenzkammer - Deckel	1			Schweißbaugruppe
1	128-70001	Druckreferenzkammer - Kammer	1			Schweißbaugruppe

Auftraggeber: Ch. Böhm
Koordinator: K. Blaum
Konstrukteur: MHK
Zeichner: MHK
Änderung
Nummer | Datum | Geändert durch
Allgemeintoleranzen für Längen- und Winkelmaße, Form und Lage nach ISO 2768-mK
Werkstückkanten ISO 13715
Oberflächen nach DIN ISO 1302
Maßstab: 1:2
Format: A1
Metrisch
Kompakt
Datum: Mittwoch, 18. Mai 2011 11:33:08
Kostenstelle: W 100
Material:
Bezeichnung: Druckreferenzkammer
Projekt: 128 - Pentatrap
Zeichnung unterliegt nicht dem Änderungsdienst
Nur zur Information
Angebotszeichnung
Fertigung freigegeben
Freigabedatum:
Unterschrift:
Max-Planck-Institut für Kernphysik Heidelberg
Zentrale Konstruktion
128-70000 (1)

Figure A.2: Drawing of the absolute pressure reference. A stainless steel chamber is attached to the differential pressure transducer *AD120* and encased in a styrofoam block. Dimensions are given in mm.

Figure A.3: PENTATRAP magnet with safety valves indicated in blue. These valves open at an overpressure of about 200 mbar.

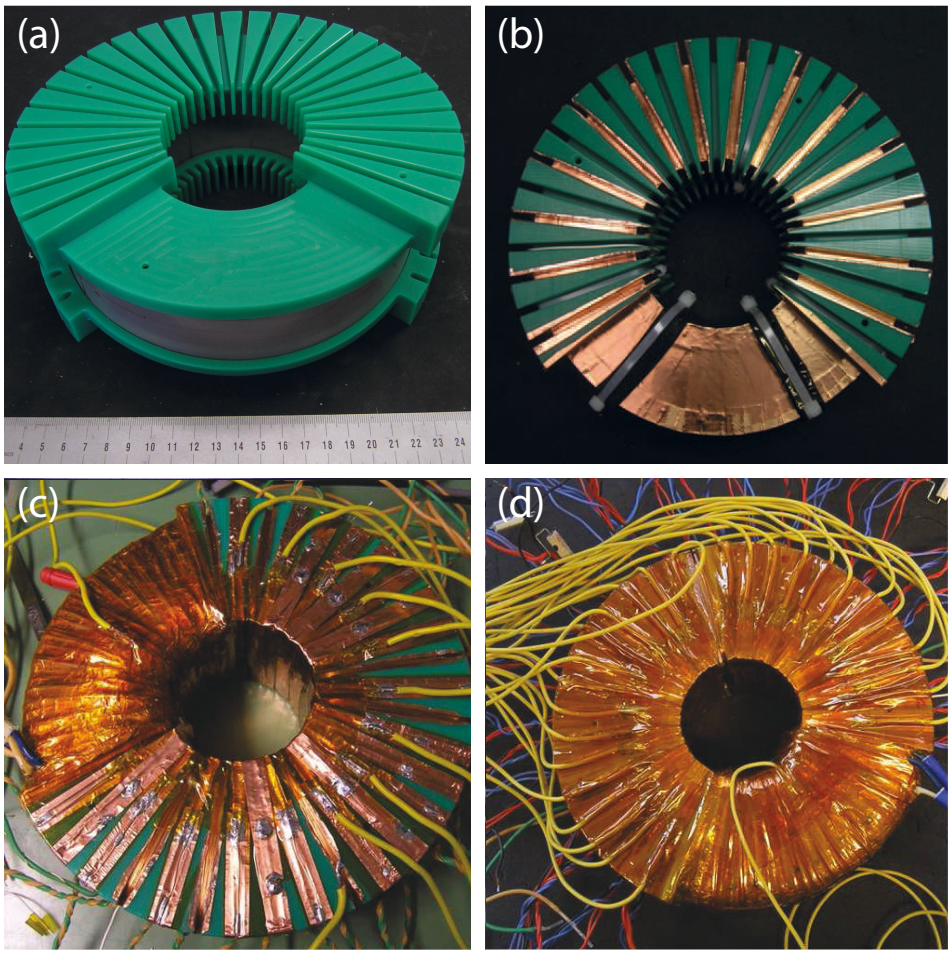

Figure A.4: StaReP LV transformer (a) without shielding, (b) partly shielded, (c) partly winded and partly shielded and (d) after shielding and winding.

Bibliography

[1] Ch. Böhm, Ch. Borgmann, G. Audi, D. Beck, K. Blaum, M. Breitenfeldt, R. B. Cakirli, T. E. Cocolios, S. Eliseev, S. George, F. Herfurth, A. Herlert, M. Kowalska, S. Kreim, D. Lunney, V. Manea, E. Minaya Ramirez, S. Naimi, D. Neidherr, M. Rosenbusch, L. Schweikhard, J. Stanja, M. Wang, R. N. Wolf, and K. Zuber. Evolution of nuclear ground-state properties of neutron-deficient isotopes around $Z = 82$ from precision mass measurements. *Physical Review C*, 90(4):044307, October 2014.

[2] K. Blaum. High-accuracy mass spectrometry with stored ions. *Physics Reports*, 425:1–78, March 2006.

[3] K. Blaum, Y. Novikov, and G. Werth. Penning traps as a versatile tool for precise experiments in fundamental physics. *Contemporary Physics*, 51:149–175, March 2010.

[4] B. Franzke, H. Geissel, and G. Münzenberg. Mass and lifetime measurements of exotic nuclei in storage rings. *Mass Spectrometry Reviews*, 27(5):428–469, 2008.

[5] A. Einstein. Ist die Trägheit eines Körpers von seinem Energieinhalt abhängig? *Annalen der Physik*, 323:639–641, 1905.

[6] T. Eronen, V.-V. Elomaa, J. Hakala, J. C. Hardy, A. Jokinen, I. D. Moore, M. Reponen, J. Rissanen, A. Saastamoinen, C. Weber, and J. Äystö. Q_{EC} Values of the Superallowed β Emitters ^{34}Cl and ^{38}K^{m}. *Physical Review Letters*, 103(25):252501, December 2009.

[7] J. C. Hardy and I. S. Towner. Superallowed $0^+ \rightarrow 0^+$ nuclear β decays: A new survey with precision tests of the conserved vector current hypothesis and the standard model. *Physical Review C*, 79(5):055502, May 2009.

[8] E. Ferri, C. Arnaboldi, G. Ceruti, M. Faverzani, F. Gatti, A. Giachero, C. Gotti, C. Kilbourne, S. Kraft-Bermuth, A. Nucciotti, G. Pessina, D. Schaeffer, and M. Sisti. MARE-1 in Milan: Status and Perspectives. *Journal of Low Temperature Physics*, 167:1035–1040, June 2012.

[9] P. C.-O. Ranitzsch, J.-P. Porst, S. Kempf, C. Pies, S. Schäfer, D. Hengstler, A. Fleischmann, C. Enss, and L. Gastaldo. Development of Metallic Magnetic

Calorimeters for High Precision Measurements of Calorimetric ^{187}Re and ^{163}Ho Spectra. *Journal of Low Temperature Physics*, 167:1004–1014, June 2012.

[10] V. M. Shabaev, O. V. Andreev, A. N. Artemyev, S. S. Baturin, A. A. Elizarov, Y. S. Kozhedub, N. S. Oreshkina, I. I. Tupitsyn, V. A. Yerokhin, and O. M. Zherebtsov. QED effects in heavy few-electron ions. *International Journal of Mass Spectrometry*, 251:109–118, April 2006.

[11] T. Stöhlker, A. Gumberidze, M. Trassinelli, V. Andrianov, H. F. Beyer, S. Kraft-Bermuth, A. Bleile, P. Egelhof, and FOCAL Collaboration. Quantum Electrodynamics in Extreme Fields: Precision Spectroscopy of High-Z H-like Systems. In S. G. Karshenboim, editor, *Precision Physics of Simple Atoms and Molecules*, volume 745 of *Lecture Notes in Physics, Berlin Springer Verlag*, page 157, 2008.

[12] S. Rainville, J. K. Thompson, E. G. Myers, J. M. Brown, M. S. Dewey, E. G. Kessler, R. D. Deslattes, H. G. Börner, M. Jentschel, P. Mutti, and D. E. Pritchard. World Year of Physics: A direct test of E=mc^2. *Nature*, 438:1096–1097, December 2005.

[13] J. J. Thomson. On rays of positive electricity. *Philosophical Magazine Series 6*, 13(77):561–575, May 1907.

[14] F. W. Aston. *Mass spectra and isotopes*. Edward Arnold London, 2nd ed. edition, 1942.

[15] G. Gamow. Mass Defect Curve and Nuclear Constitution. *Royal Society of London Proceedings Series A*, 126:632–644, March 1930.

[16] C. F. von Weizsäcker. Zur Theorie der Kernmassen. *Zeitschrift für Physik*, 96(7):431–458, 1935.

[17] H. A. Bethe and R. F. Bacher. Nuclear Physics A. Stationary States of Nuclei. *Reviews of Modern Physics*, 8:82–229, April 1936.

[18] O. Haxel, J. H. D. Jensen, and H. E. Suess. Zur Interpretation der ausgezeichneten Nukleonenzahlen im Bau der Atomkerne. *Naturwissenschaften*, 35:376–376, December 1948.

[19] H. E. Sueß, O. Haxel, and J. H. D. Jensen. Zur Interpretation der ausgezeichneten Nukleonenzahlen im Bau der Atomkerne. *Naturwissenschaften*, 36:153–155, May 1949.

[20] J. H. D. Jensen, H. E. Sueß, and O. Haxel. Modellmäßige Deutung der ansgezeichneten Nukleonenzahlen im Kernbau. *Naturwissenschaften*, 36:155–156, May 1949.

[21] O. Haxel, J. H. Jensen, and H. E. Suess. On the "Magic Numbers" in Nuclear Structure. *Physical Review*, 75:1766–1766, June 1949.

[22] O. Haxel, J. H. D. Jensen, and H. E. Suess. Modellmäßige Deutung der ausgezeichneten Nukleonenzahlen im Kernbau. *Zeitschrift fur Physik*, 128:295–311, April 1950.

[23] M. Goeppert-Mayer. On Closed Shells in Nuclei. *Physical Review*, 74:235–239, August 1948.

[24] M. Goeppert-Mayer. On Closed Shells in Nuclei. II. *Physical Review*, 75:1969–1970, June 1949.

[25] M. Goeppert-Mayer. Nuclear Configurations in the Spin-Orbit Coupling Model. I. Empirical Evidence. *Physical Review*, 78:16–21, April 1950.

[26] J. R. Pierce. *Theory and Design of Electron Beams*. D. Van Nostrand Company, New York, 1949. Chapter 3.

[27] H. G. Dehmelt. Experiments with an isolated subatomic particle at rest. *Reviews of Modern Physics*, 62:525–530, July 1990.

[28] W. Paul. Electromagnetic traps for charged and neutral particles. *Reviews of Modern Physics*, 62:531–540, July 1990.

[29] A. Kellerbauer, K. Blaum, G. Bollen, F. Herfurth, H.-J. Kluge, M. Kuckein, E. Sauvan, C. Scheidenberger, and L. Schweikhard. From direct to absolute mass measurements: A study of the accuracy of ISOLTRAP. *European Physical Journal D*, 22:53–64, January 2003.

[30] J. Dilling, R. Baartman, P. Bricault, M. Brodeur, L. Blomeley, F. Buchinger, J. Crawford, J. R. Crespo López-Urrutia, P. Delheij, M. Froese, G. P. Gwinner, Z. Ke, J. K. P. Lee, R. B. Moore, V. Ryjkov, G. Sikler, M. Smith, J. Ullrich, and J. Vaz. Mass measurements on highly charged radioactive ions, a new approach to high precision with TITAN. *International Journal of Mass Spectrometry*, 251:198–203, April 2006.

[31] J. Hakala, J. Dobaczewski, D. Gorelov, T. Eronen, A. Jokinen, A. Kankainen, V. S. Kolhinen, M. Kortelainen, I. D. Moore, H. Penttilä, S. Rinta-Antila, J. Rissanen, A. Saastamoinen, V. Sonnenschein, and J. Äystö. Precision Mass Measurements beyond Sn132: Anomalous Behavior of Odd-Even Staggering of Binding Energies. *Physical Review Letters*, 109(3):032501, July 2012.

[32] R. S. van Dyck, Jr., D. B. Pinegar, S. van Liew, and S. L. Zafonte. The UW-PTMS: Systematic studies, measurement progress, and future improvements. *International Journal of Mass Spectrometry*, 251:231–242, April 2006.

[33] M. Mukherjee, D. Beck, K. Blaum, G. Bollen, J. Dilling, S. George, F. Herfurth, A. Herlert, A. Kellerbauer, H.-J. Kluge, S. Schwarz, L. Schweikhard, and C. Yazidjian. ISOLTRAP: An on-line Penning trap for mass spectrometry on short-lived nuclides. *European Physical Journal A*, 35:1–29, January 2008.

[34] S. Kreim, D. Atanasov, D. Beck, K. Blaum, C. Böhm, C. Borgmann, M. Breitenfeldt, T. E. Cocolios, D. Fink, S. George, A. Herlert, A. Kellerbauer, U. Köster, M. Kowalska, D. Lunney, V. Manea, E. Minaya Ramirez, S. Naimi, D. Neidherr, T. Nicol, R. E. Rossel, M. Rosenbusch, L. Schweikhard, J. Stanja, F. Wienholtz, R. N. Wolf, and K. Zuber. Recent exploits of the ISOLTRAP mass spectrometer. *Nuclear Instruments and Methods in Physics Research B*, 317:492–500, December 2013.

[35] E. Kugler. The ISOLDE facility. *Hyperfine Interactions*, 129:23–42, December 2000.

[36] G. Gräff, H. Kalinowsky, and J. Traut. A direct determination of the proton electron mass ratio. *Zeitschrift fur Physik A Hadrons and Nuclei*, 297:35–39, March 1980.

[37] K. Heyde and J. L. Wood. Shape coexistence in atomic nuclei. *Reviews of Modern Physics*, 83:1467–1521, October 2011.

[38] J. Repp, C. Böhm, J. R. Crespo López-Urrutia, A. Dörr, S. Eliseev, S. George, M. Goncharov, Y. N. Novikov, C. Roux, S. Sturm, S. Ulmer, and K. Blaum. PENTATRAP: a novel cryogenic multi-Penning-trap experiment for high-precision mass measurements on highly charged ions. *Applied Physics B: Lasers and Optics*, 107:983–996, June 2012.

[39] A. H. Wapstra, G. Audi, and C. Thibault. The AME2003 atomic mass evaluation (I). Evaluation of input data, adjustment procedures. *Nuclear Physics A*, 729:129–336, December 2003.

[40] T. Fritioff, I. Bergström, S. Nagy, A. Solders, M. Suhonen, and R. Schuch. Precise measurements of ionic masses for QED tests. *International Journal of Mass Spectrometry*, 251:281–285, April 2006.

[41] M. Jentschel, P. Becker, J. Krempel, B. Lauss, G. Mana, and P. Mutti. Measurement of neutron binding energy of ^{36}Cl for a determination of $N_A h$. In *Precision Electromagnetic Measurements Digest, 2008. CPEM 2008. Conference on*, pages 632–633, 2008.

[42] F. M. Penning. Verzögerungen bei der Zündung von gasgefüllten Photozellen im Dunkeln. *Physica*, 3:563–568, June 1936.

[43] T. W. Hänsch. Nobel Lecture: Passion for precision. *Reviews of Modern Physics*, 78:1297–1309, October 2006.

[44] L. S. Brown and G. Gabrielse. Geonium theory: Physics of a single electron or ion in a Penning trap. *Reviews of Modern Physics*, 58:233–311, January 1986.

[45] M. Kretzschmar. Single particle motion in a Penning trap: description in the classical canonical formalism. *Physica Scripta*, 46:544–554, December 1992.

[46] F. G. Major, V. N. Gheorghe, and G. Werth. *Charged Particle Traps: Physics and Techniques of Charged Particle Field Confinement*, volume 37. Springer, 2005.

[47] G. Bollen, R. B. Moore, G. Savard, and H. Stolzenberg. The accuracy of heavy-ion mass measurements using time of flight-ion cyclotron resonance in a Penning trap. *Journal of Applied Physics*, 68:4355–4374, November 1990.

[48] G. Gabrielse. The true cyclotron frequency for particles and ions in a Penning trap. *International Journal of Mass Spectrometry*, 279:107–112, January 2009.

[49] P. W. Anderson. Theory of Flux Creep in Hard Superconductors. *Physical Review Letters*, 9:309–311, October 1962.

[50] P. W. Anderson and Y. B. Kim. Hard Superconductivity: Theory of the Motion of Abrikosov Flux Lines. *Reviews of Modern Physics*, 36:39–42, January 1964.

[51] G. Bollen, H.-J. Kluge, M. König, T. Otto, G. Savard, H. Stolzenberg, R. B. Moore, G. Rouleau, G. Audi, and ISOLDE Collaboration. Resolution of nuclear ground and isomeric states by a Penning trap mass spectrometer. *Physical Review C*, 46:2140, December 1992.

[52] M. König, G. Bollen, H.-J. Kluge, T. Otto, and J. Szerypo. Quadrupole excitation of stored ion motion at the true cyclotron frequency. *International Journal of Mass Spectrometry and Ion Processes*, 142:95–116, March 1995.

[53] W. M. Itano, J. C. Bergquist, J. J. Bollinger, and D. J. Wineland. Cooling methods in ion traps. *Physica Scripta Volume T*, 59:106–120, January 1995.

[54] F. Herfurth, J. Dilling, A. Kellerbauer, G. Bollen, S. Henry, H.-J. Kluge, E. Lamour, D. Lunney, R. B. Moore, C. Scheidenberger, S. Schwarz, G. Sikler, and J. Szerypo. A linear radiofrequency ion trap for accumulation, bunching, and emittance improvement of radioactive ion beams. *Nuclear Instruments and Methods in Physics Research A*, 469:254–275, August 2001.

[55] D. J. Wineland and H. G. Dehmelt. Principles of the stored ion calorimeter. *Journal of Applied Physics*, 46:919–930, February 1975.

[56] D. Lunney, J. M. Pearson, and C. Thibault. Recent trends in the determination of nuclear masses. *Reviews of Modern Physics*, 75:1021–1082, August 2003.

[57] J. Erler, N. Birge, M. Kortelainen, W. Nazarewicz, E. Olsen, A. M. Perhac, and M. Stoitsov. The limits of the nuclear landscape. *Nature*, 486:509–512, June 2012.

[58] G. Audi, M. Wang, A. H. Wapstra, F. G. Kondev, M. MacCormick, X. Xu, and B. Pfeiffer. The AME2012 atomic mass evaluation. *Chinese Physics C*, 36(12):1287–1602, Dec 2012.

[59] K. Blaum and M. Wiescher. Von der Massenformel zum Multizyklus. *Physik Journal*, 11(7):31, 2012.

[60] R. D. Woods and D. S. Saxon. Diffuse Surface Optical Model for Nucleon-Nuclei Scattering. *Physical Review*, 95:577–578, July 1954.

[61] M. Goeppert-Mayer. The shell model. *Nobel Lectures: Physics*, 3, 1963.

[62] E. Caurier, G. Martínez-Pinedo, F. Nowacki, A. Poves, and A. P. Zuker. The shell model as a unified view of nuclear structure. *Reviews of Modern Physics*, 77:427–488, April 2005.

[63] M. Bender, P.-H. Heenen, and P.-G. Reinhard. Self-consistent mean-field models for nuclear structure. *Reviews of Modern Physics*, 75:121–180, January 2003.

[64] W. D. Myers and W. J. Swiatecki. Nuclear masses and deformations. *Nuclear Physics*, 81:1, June 1966.

[65] J. Duflo and A. P. Zuker. Microscopic mass formulas. *Physical Review C*, 52:23, July 1995.

[66] G. T. Garvey and I. Kelson. New Nuclidic Mass Relationship. *Physical Review Letters*, 16:197–200, January 1966.

[67] W. Benenson and E. Kashy. Isobaric quartets in nuclei. *Reviews of Modern Physics*, 51:527–540, July 1979.

[68] W. Heisenberg. Über den Bau der Atomkerne. I. *Zeitschrift fur Physik*, 77:1–11, January 1932.

[69] W. Heisenberg. Über den Bau der Atomkerne. II. *Zeitschrift fur Physik*, 78:156–164, March 1932.

[70] M. Bender, K. Rutz, P.-G. Reinhard, and J. A. Maruhn. Pairing gaps from nuclear mean-field models. *European Physical Journal A*, 8:59–75, July 2000.

[71] J. Dobaczewski, P. Magierski, W. Nazarewicz, W. Satuła, and Z. Szymański. Odd-even staggering of binding energies as a consequence of pairing and mean-field effects. *Physical Review C*, 63(2):024308, February 2001.

[72] K. Kreim, M. L. Bissell, J. Papuga, K. Blaum, M. De Rydt, R. F. Garcia Ruiz, S. Goriely, H. Heylen, M. Kowalska, R. Neugart, G. Neyens, W. Nörtershäuser, M. M. Rajabali, R. Sánchez Alarcón, H. H. Stroke, and D. T. Yordanov. Nuclear charge radii of potassium isotopes beyond N=28. *Physics Letters B*, 731:97–102, April 2014.

[73] E. W. Otten. Nuclear radii and moments of unstable isotopes. In *Treatise on heavy ion science*, volume 8, pages 517–638. Springer, 1989.

[74] V. Manea, D. Atanasov, D. Beck, K. Blaum, C. Borgmann, R. B. Cakirli, T. Eronen, S. George, F. Herfurth, A. Herlert, M. Kowalska, S. Kreim, Y. A. Litvinov, D. Lunney, D. Neidherr, M. Rosenbusch, L. Schweikhard, F. Wienholtz,

R. N. Wolf, and K. Zuber. Collective degrees of freedom of neutron-rich A $\approx$ 100 nuclei and the first mass measurement of the short-lived nuclide ^{100}Rb. *Physical Review C*, 88(5):054322, November 2013.

[75] U. Köster, V. N. Fedoseyev, A. N. Andreyev, U. C. Bergmann, R. Catherall, J. Cederkäll, M. Dietrich, H. de Witte, D. V. Fedorov, L. Fraile, S. Franchoo, H. Fynbo, U. Georg, T. Giles, M. Gorska, M. Hannawald, M. Huyse, A. Joinet, O. C. Jonsson, K. L. Kratz, K. Kruglov, C. Lau, J. Lettry, V. I. Mishin, M. Oinonen, K. Partes, K. Peräjärvi, B. Pfeiffer, H. L. Ravn, M. D. Seliverstov, P. Thirolf, K. van de Vel, P. van Duppen, J. van Roosbroeck, L. Weissman, I. Is365, Is393, and Isolde Collaborations. On-line yields obtained with the ISOLDE RILIS. *Nuclear Instruments and Methods in Physics Research B*, 204:347–352, 2003.

[76] R. N. Wolf, F. Wienholtz, D. Atanasov, D. Beck, K. Blaum, C. Borgmann, F. Herfurth, M. Kowalska, S. Kreim, Y. A. Litvinov, D. Lunney, V. Manea, D. Neidherr, M. Rosenbusch, L. Schweikhard, J. Stanja, and Z. Zuber. ISOLTRAP's multi-reflection time-of-flight mass separator/spectrometer. *International Journal of Mass Spectrometry*, 349:123–133, September 2013.

[77] G. Savard, S. Becker, G. Bollen, H.-J. Kluge, R. B. Moore, T. Otto, L. Schweikhard, H. Stolzenberg, and U. Wiess. A new cooling technique for heavy ions in a Penning trap. *Physics Letters A*, 158:247–252, September 1991.

[78] D. Beck. *Aufbau einer zylindrischen Penningfalle zum Einfang und Kühlen von Ionen*. Diploma thesis, Johannes Gutenberg-Universität, Mainz, 1993.

[79] H. Raimbault-Hartmann, D. Beck, G. Bollen, M. König, H.-J. Kluge, E. Schark, J. Stein, S. Schwarz, and J. Szerypo. A cylindrical Penning trap for capture, mass selective cooling, and bunching of radioactive ion beams. *Nuclear Instruments and Methods in Physics Research B*, 126:378–382, 1997.

[80] M. Kowalska, S. Naimi, J. Agramunt, A. Algora, D. Beck, B. Blank, K. Blaum, C. Böhm, C. Borgmann, M. Breitenfeldt, L. M. Fraile, S. George, F. Herfurth, A. Herlert, S. Kreim, D. Lunney, E. Minaya-Ramirez, D. Neidherr, M. Rosenbusch, B. Rubio, L. Schweikhard, J. Stanja, and K. Zuber. Trap-assisted decay spectroscopy with ISOLTRAP. *Nuclear Instruments and Methods in Physics Research A*, 689:102–107, October 2012.

[81] St. Schwarz. priv. comm., 2014.

[82] G. Audi, A. H. Wapstra, and C. Thibault. The AME2003 atomic mass evaluation: (II). Tables, graphs and references. *Nuclear Physics A*, 729:337–676, December 2003.

[83] Ch. Borgmann. *Mass Measurements of Exotic Ions in the Heavy Mass Region for Nuclear Structure Studies at ISOLTRAP*. Ph.D. thesis, Ruprecht Karls-Universität, Heidelberg, 2012.

[84] S. Eliseev, C. Böhm, D. Beck, K. Blaum, M. Breitenfeldt, V. N. Fedosseev, S. George, F. Herfurth, A. Herlert, H.-J. Kluge, M. Kowalska, D. Lunney, S. Naimi, D. Neidherr, Y. N. Novikov, M. Rosenbusch, L. Schweikhard, S. Schwarz, M. Seliverstov, and K. Zuber. Direct mass measurements of ^{194}Hg and ^{194}Au: A new route to the neutrino mass determination? *Physics Letters B*, 693:426–429, October 2010.

[85] J. Ketelaer, J. Krämer, D. Beck, K. Blaum, M. Block, K. Eberhardt, G. Eitel, R. Ferrer, C. Geppert, S. George, F. Herfurth, J. Ketter, S. Nagy, D. Neidherr, R. Neugart, W. Nörtershäuser, J. Repp, C. Smorra, N. Trautmann, and C. Weber. TRIGA-SPEC: A setup for mass spectrometry and laser spectroscopy at the research reactor TRIGA Mainz. *Nuclear Instruments and Methods in Physics Research A*, 594:162–177, September 2008.

[86] J. Stanja, C. Borgmann, J. Agramunt, A. Algora, D. Beck, K. Blaum, C. Böhm, M. Breitenfeldt, T. E. Cocolios, L. M. Fraile, F. Herfurth, A. Herlert, M. Kowalska, S. Kreim, D. Lunney, V. Manea, E. Minaya Ramirez, S. Naimi, D. Neidherr, M. Rosenbusch, L. Schweikhard, G. Simpson, F. Wienholtz, R. N. Wolf, and K. Zuber. Mass spectrometry and decay spectroscopy of isomers across the $Z = 82$ shell closure. *Physical Review C*, 88(5):054304, November 2013.

[87] C. Weber, G. Audi, D. Beck, K. Blaum, G. Bollen, F. Herfurth, A. Kellerbauer, H.-J. Kluge, D. Lunney, and S. Schwarz. Atomic mass measurements of short-lived nuclides around the doubly-magic ^{208}Pb. *Nuclear Physics A*, 803:1–29, April 2008.

[88] J. Dobaczewski, H. Flocard, and J. Treiner. Hartree-Fock-Bogolyubov description of nuclei near the neutron-drip line. *Nuclear Physics A*, 422:103–139, June 1984.

[89] S. Hilaire and M. Girod. Large-scale mean-field calculations from proton to neutron drip lines using the D1S Gogny force. *European Physical Journal A*, 33:237–241, August 2007.

[90] A. N. Andreyev and T. E. Cocolios. Beta-delayed fission and in-source laser spectroscopy in the lead region. Technical report, CERN-INTC-2014-013 / INTC-SR-029, 2014.

[91] A. E. Barzakh, L. K. Batist, D. V. Fedorov, V. S. Ivanov, K. A. Mezilev, P. L. Molkanov, F. V. Moroz, S. Y. Orlov, V. N. Panteleev, and Y. M. Volkov. Changes in the mean-square charge radii and magnetic moments of neutron-deficient Tl isotopes. *Physical Review C*, 88(2):024315, August 2013.

[92] D. Berdichevsky and F. Tondeur. Nuclear core densities, isotope shifts, and the parametrization of the droplet model. *Zeitschrift fur Physik A Hadrons and Nuclei*, 322:141–147, March 1985.

[93] M. Bender, G. F. Bertsch, and P.-H. Heenen. Global study of quadrupole correlation effects. *Physical Review C*, 73(3):034322, March 2006.

[94] I. Angeli and K. P. Marinova. Table of experimental nuclear ground state charge radii: An update. *Atomic Data and Nuclear Data Tables*, 99:69–95, January 2013.

[95] E. Chabanat, P. Bonche, P. Haensel, J. Meyer, and R. Schaeffer. A Skyrme parametrization from subnuclear to neutron star densitiesPart II. Nuclei far from stabilities. *Nuclear Physics A*, 635:231–256, May 1998.

[96] B. S. Reehal and R. A. Sorensen. Odd-even staggering of nuclear radii. *Nuclear Physics A*, 161:385–400, February 1971.

[97] J. Stanja. *Synergy of decay spectroscopy and mass spectrometry for the study of exotic nuclides*. Ph.D. thesis, Technische Universität, Dresden, 2012.

[98] Evaluated Nuclear Structure Data File (ENSDF), 2013. Accessed on 10.10.2014.

[99] U. Kentsch, G. Zschornack, A. Schwan, and F. Ullmann. Short time ion pulse extraction from the Dresden electron beam ion trapa). *Review of Scientific Instruments*, 81(2):020000, February 2010.

[100] J. Repp. *The setup of the high-precision Penning trap mass spectrometer PENTATRAP and first production studies of highly charged ions*. Ph.D. thesis, Ruprecht Karls-Universität, Heidelberg, 2012.

[101] J. R. Crespo López-Urrutia, J. Braun, G. Brenner, H. Bruhns, A. Lapierre, A. J. González Martínez, V. Mironov, R. Soria Orts, H. Tawara, M. Trinczek, and J. Ullrich. Optimization of the charge state distribution of the ion beam extracted from an EBIT by dielectronic recombination. *Review of Scientific Instruments*, 75:1560–1562, May 2004.

[102] H.-J. Kluge, T. Beier, K. Blaum, L. Dahl, S. Eliseev, F. Herfurth, B. Hofmann, O. Kester, S. Koszudowski, C. Kozhuharov, G. Maero, W. Nörtershäuser, J. Pfister, W. Quint, U. Ratzinger, A. Schempp, R. Schuch, T. Stöhlker, R. C. Thompson, M. Vogel, G. Vorobjev, D. F. A. Winters, and G. Werth. HITRAP: A Facility at GSI for Highly Charged Ions. *Advances in Quantum Chemistry*, 53:83–98, 2008.

[103] A. O. Rischka. *Aufbau eines Heliumdruck- und Heliumlevel-Stabilisierungssystems und Konstruktion eines kryogenen Faraday-Bechers für PENTATRAP*. Master thesis, Ruprecht Karls-Universität, Heidelberg, 2014.

[104] C. Roux, C. Böhm, A. Dörr, S. Eliseev, S. George, M. Goncharov, Y. N. Novikov, J. Repp, S. Sturm, S. Ulmer, and K. Blaum. The trap design of PENTATRAP. *Applied Physics B: Lasers and Optics*, 107:997–1005, June 2012.

[105] D. Beck, H. Brand, K. Poppensieker, and K. Wunderle. LabVIEW control applications for Cave A and SHIPTRAP. *GSI Scientific Report*, 2002.

[106] M. L. Goncharov. *High-precision Penning-trap mass spectrometry at SHIPTRAP and PENTATRAP for neutrino physics research*. Ph.D. thesis, Ruprecht Karls-Universität, Heidelberg, 2014.

[107] E. A. Cornell, R. M. Weisskoff, K. R. Boyce, and D. E. Pritchard. Mode coupling in a Penning trap: π pulses and a classical avoided crossing. *Physical Review A*, 41:312–315, January 1990.

[108] C.-E. Roux. *High-resolution mass spectrometry: The trap design and detection system of PENTATRAP and new Q-values for neutrino studies*. Ph.D. thesis, Ruprecht Karls-Universität, Heidelberg, 2012.

[109] A. Dörr. *in preparation*. Ph.D. thesis, Ruprecht Karls-Universität, Heidelberg, 2015.

[110] A. O. Rischka. *Aufbau und Charakterisierung eines Systems zur Stabilisierung des Magnetfeldes an PENTATRAP*. Bachelor thesis, Ruprecht Karls-Universität, Heidelberg, 2011.

[111] S. Streubel, T. Eronen, M. Höcker, J. Ketter, M. Schuh, R. S. Van Dyck, and K. Blaum. Toward a more accurate Q value measurement of tritium: status of THe-Trap. *Applied Physics B: Lasers and Optics*, 114:137–145, January 2014.

[112] S. Streubel. *Kontrolle der Umwelteinflüsse auf THe-Trap am Beispiel der Bestimmung des Massenverhältnisses von Kohlenstoff-12 zu Sauerstoff-16*. Ph.D. thesis, Ruprecht Karls-Universität, Heidelberg, 2014.

[113] R. S. Van Dyck, D. L. Farnham, S. L. Zafonte, and P. B. Schwinberg. Ultrastable superconducting magnet system for a penning trap mass spectrometer. *Review of Scientific Instruments*, 70:1665–1671, March 1999.

[114] J. M. Lockhart, R. L. Fagaly, L. W. Lombardo, and B. Muhlfelder. Magnetic susceptibility of instrument materials below 10k. *Physica B Condensed Matter*, 165:147–148, August 1990.

[115] G. L. Salinger and J. C. Wheatley. Magnetic Susceptibility of Materials Commonly Used in the Construction of Cryogenic Apparatus. *Review of Scientific Instruments*, 32:872–874, July 1961.

[116] S. Ulmer. *First Observation of Spin Flips with a Single Proton Stored in a Cryogenic Penning Trap*. Ph.D. thesis, Ruprecht Karls-Universität, Heidelberg, 2011.

[117] Stahl-Electronics. *UM 1-14 Data Sheet*. `http://www.stahl-electronics.com/bilder/UM_1-14_LN_high_precision_voltage_source.pdf`. Accessed on 16.10.2014.

[118] S. Sturm *et al. Article in preparation*. 2014.

[119] R. Zirpel. priv. comm., 2013.

[120] Fluke Calibration. *8508A Users Manual*. http://us.flukecal.com/literature/product-manuals/8508a-reference-multimeter-users-manual. Accessed on 16.10.2014.

[121] See http://www.alamath.com for a program to calculate the Allan deviation. Accessed on 10.10.2014.

[122] D. W. Allan. Statistics of atomic frequency standards. *Proceedings of the IEEE*, 54(2):221–230, 1966.

[123] S. Sturm, F. Köhler, J. Zatorski, A. Wagner, Z. Harman, G. Werth, W. Quint, C. H. Keitel, and K. Blaum. High-precision measurement of the atomic mass of the electron. *Nature*, 506:467–470, February 2014.

[124] B. A. Marsh, B. Andel, A. N. Andreyev, S. Antalic, D. Atanasov, A. E. Barzakh, B. Bastin, C. Borgmann, L. Capponi, T. E. Cocolios, T. Day Goodacre, M. Dehairs, X. Derkx, H. De Witte, D. V. Fedorov, V. N. Fedosseev, G. J. Focker, D. A. Fink, K. T. Flanagan, S. Franchoo, L. Ghys, M. Huyse, N. Imai, Z. Kalaninova, U. Köster, S. Kreim, N. Kesteloot, Y. Kudryavtsev, J. Lane, N. Lecesne, V. Liberati, D. Lunney, K. M. Lynch, V. Manea, P. L. Molkanov, T. Nicol, D. Pauwels, L. Popescu, D. Radulov, E. Rapisarda, M. Rosenbusch, R. E. Rossel, S. Rothe, L. Schweikhard, M. D. Seliverstov, S. Sels, A. M. Sjödin, V. Truesdale, C. Van Beveren, P. Van Duppen, K. Wendt, F. Wienholtz, R. N. Wolf, and S. G. Zemlyanoy. New developments of the in-source spectroscopy method at RILIS/ISOLDE. *Nuclear Instruments and Methods in Physics Research B*, 317:550–556, December 2013.

[125] R. N. Wolf, D. Beck, K. Blaum, C. Böhm, C. Borgmann, M. Breitenfeldt, N. Chamel, S. Goriely, F. Herfurth, M. Kowalska, S. Kreim, D. Lunney, V. Manea, E. Minaya Ramirez, S. Naimi, D. Neidherr, M. Rosenbusch, L. Schweikhard, J. Stanja, F. Wienholtz, and K. Zuber. Plumbing Neutron Stars to New Depths with the Binding Energy of the Exotic Nuclide Zn82. *Physical Review Letters*, 110(4):041101, January 2013.

[126] F. Wienholtz, D. Beck, K. Blaum, C. Borgmann, M. Breitenfeldt, R. B. Cakirli, S. George, F. Herfurth, J. D. Holt, M. Kowalska, S. Kreim, D. Lunney, V. Manea, J. Menéndez, D. Neidherr, M. Rosenbusch, L. Schweikhard, A. Schwenk, J. Simonis, J. Stanja, R. N. Wolf, and K. Zuber. Masses of exotic calcium isotopes pin down nuclear forces. *Nature*, 498:346–349, June 2013.

[127] P. Ascher, D. Atanasov, K. Blaum, Ch. Böhm, Ch. Borgmann, M. Breitenfeldt, R. B. Cakirli, T. E. Cocolios, T. Eronen, S. George, F. Herfurth, A. Herlert, D. Kisler, M. Kowalska, K. Kreim, Yu. A. Litvinov, D. Lunney, V. Manea, E. Minaya Ramirez, S. Naimi, D. Neidherr, M. Rosenbusch, L. Schweikhard, F. Wienholtz, A. Welker, R. N. Wolf, and K. Zuber. Precision Mass Measurements with ISOLTRAP to Study the Evolution of the N= 82 Shell Gap far from Stability. Technical report, CERN-INTC-2013-022, INTC-P-382, 2013.

[128] A. Nucciotti. The MARE Project. *Journal of Low Temperature Physics*, 151:597–602, May 2008.

Acknowledgments

First of all, I would like to thank my supervisor Prof. Dr. Klaus Blaum for his continous motivation and support. Thank you for beeing always available when your opinion and advice was needed. I am glad that I got the chance to do my PhD in your group. There was much more support than what one could expect from a supervisor – thank you!

I thank PD Dr. Klaus Reygers for accepting to be the second referee of this thesis.

Thanks a lot to the Penning trap team in Heidelberg for the great time. Especially, I would like to thank all PENTATRAP members: Dr. Sergey Eliseev, Dr. Christian Roux, Dr. Julia Repp, Dr. Mikhail Goncharov, Andreas Dörr, Alexander Rischka and Rima Schüssler. Sergey, thanks for your advice in different projects, for discussions and also for corrections of this thesis. Mikhail, thanks for your patience, the discussions on the voltage source and also the support, whenever some programming was needed and thank you for your comments on this thesis. Andreas and Christian, thank you for many discussions and advice. Julia, I am very glad, that I met you at the very beginning of the physics studies. We had a great time in Mainz and in Heidelberg. Thanks for being there all the years and your support in many situations! Alexander, thanks a lot for your work on the stabilization system and for your creative ideas. Rima, thanks a lot for your help during the last months. Thank you PENTATRAP for a lot of fun!

Thanks to the THe-Trap team, especially Dr. Tommi Eronen, Dr. Sebastian Streubel, Martin Höcker and Jochen Ketter. Thank you very much for being always available for discussions and for testing parts of the voltage source and parts of the stabilization system at your experiment. I really appreciate all your efforts.

Thanks to Dr. Pauline Ascher for comments on the thesis.

I thank the Penning trap group members in Mainz for the fruitful discussions, especially Dr. Sven Sturm, Dr. Anke Kracke and Florian Köhler from the g-factor team. Sven, thank you very much for your developments, discussions and advice concerning the voltage source and for your comments on this thesis. Florian and Sven, thank you for testing the stability of the voltage source at the g-factor experiment. Anke, thanks a lot for corrections of this thesis.

I thank the members of the ISOLTRAP collaboration for a great time at CERN but also for many valuable discussions. Thanks especially to Dr. Susanne Kreim and Dr. R Burcu Cakirli. I learned a lot from you during many hours of discussions. Thanks to both of you for your patience, for being always available and your advice in nuclear physics but also in questions far away from physics! Susanne, thank you also for your comments on this thesis. Furthermore, I would like to thank Dr. Christopher Borgmann for his help concerning the data analysis and evaluation and also many helpful discussions beyond. Furthermore, I thank Dr. Vladimir Manea for his ideas and valuable comments on the

nuclear structure of the thallium isotopes.

At this point I would also like to thank Mrs Dücker for her organisational support and for the always friendly atmosphere. Furthermore, I would like to thank Ralph Zilly for his technical support and creative ideas.

I would like to thank the team of the electronics workshop: Thomas Wagner, Volker Wieder, Dennis Obieglo, Jan Martin, Domenik Marschall, Matthias Steigleder and Jonas Westermann. Thanks for all the work and effort on the voltage source and also for all discussions and measurements!
Furthermore, I thank Roland Zirpel from the PTB Braunschweig for his advice concerning the voltage source.

I thank Prof. Dr. Jacek Dobaczewski for discussions and for providing data on the pairing gaps as well as Dr. Anatoly Barzakh for his advice and discussion concerning nuclear charge radii.

I would like to thank Dr. Georges Audi and Dr. Meng Wang for the discussions of the thallium masses. Furthermore, I thank Dr. David Lunney for his ideas and advice for the thallium data evaluation.

I thank Prof. Dr. Jens Dilling for final proof reading of this thesis.

I would like to thank my parents, Irmgard and Karl, as well as my sister Carina for their continuous support and encouraging words during all phases of this thesis. Thank you for being there for me!
Last, but not least I would like to thank Jürgen and Marlene. Jürgen, thank you for your incredible support within the last years. Thank you for discussions on scientific working but also for your patience and your encouragement. Thank you for your motivating words at the right time!
Marlene, thank you for the great time! Gofieche, Pagei and Ewawa – you make me laugh every day. Thank you!